Alkaline membrane water electrolysis with non-noble catalysts

Kraglund, Mikkel Rykær

Publication date:
2017

Document Version
Publisher's PDF, also known as Version of record

Mikkel Rykær Kraglund

Alkaline membrane water electrolysis with non-noble catalysts

PhD Thesis

July 2017

DTU Energy
Department of Energy Conversion and Storage

Title:

Alkaline membrane water electrolysis with non-noble catalysts

Author:

Mikkel Rykær Kraglund
E-mail: mirkr@dtu.dk

Principal supervisor:

Erik Christensen, Senior Researcher, DTU Energy
E-mail: erchr@dtu.dk

Co-supervisors:

Jens Oluf Jensen, Professor, Head of Section, DTU Energy
E-mail: jojen@dtu.dk

David Aili, Researcher, DTU Energy
E-mail: larda@dtu.dk

Aleksey Nikiforov, Development Engineer, DTU Energy
E-mail: nava@dtu.dk

Date of submission:

Submitted 31st of July, 2017

Defended 13th of October, 2017

Revised on 19th of October, 2017

Department of Energy Conversion and Storage

Section for Proton Conductors
Technical University of Denmark
Kemitorvet, Building 207
2800 Kgs. Lyngby
Denmark

www.energy.dtu.dk
Tel: (+45) 46 77 58 00

ISBN: 978-87-92986-65-8

"Yes, my friends, I believe that water will one day be employed as fuel, that hydrogen and oxygen which constitute it, used singly or together, will furnish an inexhaustible source of heat and light, of an intensity of which coal is not capable."

- Jules Verne 1874, The Mysterious Island

Preface

This thesis is submitted in candidacy for a Ph.D. degree from the Technical University of Denmark (DTU). The work herein was conducted over 3 years running from August 2014 to July 2017. The work has primarily taken place at Section for Proton Conductors, at the Department of Energy Conversion and Storage, supervised by Erik Christensen, Jens Oluf Jensen, David Aili and Aleksey Nikiforov. A part of the work, from September 2016 to December 2016, was conducted at Forschungszentrum Jülich (FZJ), Germany, at the Institute of Energy and Climate Research, IEK-3: Electrochemical Process Engineering, in collaboration with Marcelo Carmo.

The project was internally funded at DTU Energy, partially by internal projects *PorouZ* and *TT JOEL*.

Mikkel Rykær Kraglund
July 2017

Abstract

As renewable energy sources reach higher grid penetration, large scale energy storage solutions are becoming increasingly important. Hydrogen produced with renewable energy by water electrolysis is currently the only option to solve this challenge on a global scale, and green hydrogen is essential for the decarbonization of the transportation and industrial sector required to limit climate change.

Electrolysis done with an alkaline electrolyte is a cheap, proven, and commercially available technology, but the systems suffer from inefficiency and limited operating flexibility. The work herein seek to address these issues by introducing alkaline polymeric membranes and efficient electrodes based on novel materials.

Polymer electrolyte membranes with sufficient OH^--conductivity enable a drastic reduction of the electrode spacing, which lead to improved ohmic properties enabling operation at higher current density. This, combined with better gas separation properties and a higher operating flexibility, have the prospects of significantly reducing the capex and opex of electrolysis systems, and the cost of green hydrogen. Towards this goal, membranes based on poly(2,2'-(*m*-phenylene)-5,5'-bibenzimidazole) (*m*-PBI) as well as poly(2,2'-(*m*-mesitylene)-5,5'-bibenzimidazole) (mes-PBI) were investigated as electrolyte for alkaline electrolysis cells.

PBI membranes were equilibrated with aqueous KOH and applied as separator, and polarization data from cells at 20-25 wt% KOH using these membranes showed improved ohmic behaviour over cells with conventional porous separators. This was strikingly clear when combined with active electrodes with Raney-nickel-based coatings. With thin 40 µm *m*-PBI membranes, Raney-nickel-molybdenum cathodes and nickel anodes, cells operated at 80°C with 24 wt%

KOH (aq) achieved 1000 mA cm^{-2} at 1.7 V and 2800 mA cm^{-2} at 2.0 V. Electrochemical impedance spectroscopy data showed a 6-fold reduction in ohmic cell resistance compared to conventional materials. Albeit good performance, *ex-situ* characterization and durability tests showed that polymer backbone and membrane stability remained a problem under conventional operating conditions.

To accompany novel membranes in alkaline electrolysis, electrodes can be employed in a zero-gap configuration. This enable different electrode concepts than used in commercial systems. Inspired by recent literature, nickel-iron based anodes, and nickel-tin as well as nickel-molybdenum cathodes were investigated in half cell tests. The materials were applied as coatings on nickel foam and showed improvements in the order of 150-300 mV over reference nickel materials at room temperature, depending on the specific electrode and electrolyte concentration used.

In a secondary approach, electrodes were prepared using powder and polymeric binders. Using nickel powder with *m*-PBI binder in a nickel foam as cathode, a reduction in cell overpotential of more than 200 mV was achieved compared against a pristine nickel foam cathode.

Resumé

I forbindelse med at vedvarende energikilder opnår en større udbredelse bliver energilagring i stor skala gradvist mere vigtigt. Brint produceret vha. vedvarende energi fra elektrolyse af vand er i øjeblikket den eneste mulighed til at løse denne udfordring på en global skala, og grøn brint er essentielt for at afkarbonisere transport- og industrisektorene, hvilket er nødvendigt hvis klimaændringerne skal begrænses.

Elektrolyse med alkalisk elektrolyt er en billig, gennemtestet, og kommercielt tilgængelig teknologi, men den nuværende teknologi lider under ringe effektivitet og begrænset driftsfleksibilitet. Arbejdet beskrevet i dette værk forsøger at imødekomme disse problemer ved at anvende alkaliske polymer-membraner frem for porøse separatorer, samt ved at anvende elektroder baseret på nye materialer uden ædelmetaller.

Ved brug af polymer-elektrolyt-membraner med tilstrækkelig OH^- ledningsevne er det muligt at reducere afstanden mellem elektroderne i en elektrolysecelle drastisk. Dette medfører bedre ohmiske egenskaber og åbner op for drift ved højere strømtætheder. Kombineret med bedre gas adskillelses egenskaber og større driftsfleksibilitet giver det udsigt til at nedsætte anlægs- og driftsomkostninger, og dermed reducere omkostningerne ved at producere grøn brint. For at opnå dette er membraner baseret på poly(2,2′-(*m*-phenylen)-5,5′-bibenzimidazol) (*m*-PBI), samt poly(2,2′-(*m*-mesitylen)-5,5′-bibenzimidazol) (mes-PBI) blevet undersøgt som elektrolyt til alkaliske elektrolyseceller.

PBI membranerne blev aktiveret i stærk KOH (aq) opløsning og anvendt som separator. Polariseringsdata fra celler med disse membraner ved 20-25 wt% KOH udviser forbedrede ohmiske egenskaber i forhold til celler med traditionelle porøse separatorer. Dette var især tydeligt når membranerne blev kombineret med aktive elektroder baseret på Raney-nikkel belægninger. Med tynde 40 µm *m*-PBI

membraner, Raney-nikkel-molybdæn katoder, og nikkel anoder, opnåede celler kørt ved 80°C og 24 wt% KOH (aq) op til 1000 mA cm^{-2} ved 1.7 V, og 2800 mA cm^{-2} ved 2.0 V. Elektrokemisk impedansspektroskopi viste for disse celler en 6-foldig reduktion af den ohmiske celle modstand, sammenlignet med traditionelle celler. På trods af gode elektrokemiske egenskaber har det dog vist sig ved senere karakterisering og stabilitetstest at polymerrygraden bliver nedbrugt, og membranstabiliteten er dermed stadigvæk utilstrækkelig under konventionelle driftsbetingelser.

Til at ledsage de nye membraner i alkalisk elektrolyse kan elektroder blive anvendt uden nogen afstand til membranen. Det muliggør forskellige elektrode koncepter end dem anvendt i kommercielle systemer. Inspireret af den nyeste litteratur er nikkel-jern anoder, samt nikkel-tin og nikkel-molybdæn katoder blevet undersøgt, primært i halvcelle tests. Materialerne er blevet belagt på nikkelskum og elektroderne har vist en forbedring i størrelsen 150-300 mV ved stue temperature i forhold til ubelagte referenceelektroder af nikkelskum. Den præcise forbedring afhænger af den specifikke elektrode og de resterende eksperimentelle betingelser så som elektrolyttens koncentration.

En anden strategi til at fremstille aktive elektroder er at anvende pulver og polymeriske bindere. Med en katode baseret på nikkelpulver, *m*-PBI binder og et nikkelskum som substrat, er det lykkedes at opnå en reduktion celle overspænding på mere end 200 mV i forhold til referencemålinger.

Acknowledgements

I would like to extend my gratitude towards everyone who contributed to making the previous three years productive and enjoyable.

First and foremost my supervisors: Erik Christensen for his guidance, and for always being a second set of ears, when I needed someone to discuss with. Jens Oluf Jensen for helping me understand and discuss some of the fundamental problems. David Aili for answering my countless questions in organic chemistry. And Aleksey Nikiforov for helping me getting started in the laboratory with the practical work.

A special thanks goes to Lars Nilausen Cleemann, who helped with many different practical issues, from programming through practical equipment help to questions regarding electrochemistry. And to Claus Burke Mortensen, Steen Blichfelt, Larisa Seerup, and Chao Pan for technical and experimental help throughout the project.

I also want to thank Lene Christensen and Kirsten Munkgaard Thomsen for their invaluable help as section secretaries.

My sincere thanks also goes to Marcelo Carmo for his hospitality in hosting me at my exchange stay at Forschungszentrum Jülich. To the technical staff at FZJ supporting me during the three months, Daniel Holtz, Stefanie Fischer, and Florian Berg, as well as Fabian Tigges who worked with the alkaline setup at FZJ prior to my arrival.

And very importantly all the office mates, the lunch group, former and current PhD students and postdocs; Andreas Kirkebæk, Annemette Hindhede Jensen, Anton Vassiliev, Arvind Kannan, Benedict Axel Brandes, Carstren Brorson Prag, Hans Becker, Illia Shypunov, Lijie Zhong, Stine and Tonny Søndergaard, and Yang Hu, all with whom I have agreed with, disagreed with, and shared a lot of coffee with.

The students who did their projects with me, Anders Richter Kjeldsen with his bachelor project and Mikkel P. F. Laursen with his master project, also deserve a big thank you for their contributions to my work and time here.

I also want to thank my friends from Physics who have been here with me since the beginning in 2008, Jonas, Rune, Morten and Mikkel, for our many talks on PhD life ups and downs during lunch and outside working hours.

And my family for supporting me and encouraging me in this endeavour.

And the rest of the PRO section for being my colleagues, and those that I might have forgotten.

Table of Contents

List of Figures

List of Tables

1

Introduction

1.1 Energy Resources

The industrial revolution in the early 19th-century marked a paradigm shift for primary energy sources. Previously, mankind was mostly burning firewood or similar biofuels, but along with the industrialization arose the need for and use of non-replenishable fossil fuels. Ever since then, coal, oil, and natural gas have played a dominant role in driving the development of todays societies. Energy is a requirement for all modern necessities and conveniences, from electricity, heating, and transportation, to the production of food, goods, and all industrial processes. As more and more people have their standard of living increase, the worlds total final energy consumption has continued to increase. From 4661 Mtoe (mega-tonne oil equivalent) anually in 1973 (equivalent to an average power of 6.2 TW) to 9425 Mtoe (12.5 TW) in 2014.[1] This is expected to increase and projected to grow by 48 % in 2040, primarily driven up as the populations of non-OECD countries increase their standard of living and energy requirements.[2]

1.1.1 Fossil fuels

With the advent of fossil fuels mankind stepped into a new era. However, the increase in productivity from these energy-dense resources have come at a cost. At its core, three drawbacks are associated with burning of fossil fuels: Availability of known reserves and resources; pollution of air and environment, with related health hazards; and emission of green house gasses primarily carbon dioxide, leading to global warming and climate change.

Fossil fuels is a finite resource and is destined to run out eventually. With 2015 production rate, known reserves of oil, coal and gas will last 51, 114 and 53 years.[3] Known reserves are those resources that are currently known that can be extracted under 2015 technological and economical conditions. As prices increase and technology develops, some harder-to-get deposits may become feasible to extract, however, the numbers do not consider the predicted increased production rates. Oil and natural gas reserves have increased over the last 20 years, but so has production and consumption. In general, supply forecasts are very uncertain and can differ quite significantly.[4]

The burning of hydrocarbon fuels is associated with higher levels of local pollution. This is from everything between centralized power generation and industry, through burning of wood and coal for residential cooking and heating, to the exhaust from vehicles in urban and city areas. The world health organization (WHO) estimate that 7 million people died world wide in 2012 as a result of pollution exposure, corresponding to one-in-eight deaths globally. Of these, 3 million were due to ambient air pollution.[5,6]

The extraction and combustion of fossil fuels stored in geological deposits for millennia introduce carbon into the atmosphere in the form of anthropogenic carbon dioxide. The CO_2 concentration in the atmosphere has increased rapidly over the last 100 years. From levels around 280-300 ppm in 1850 at the beginning of the industrial revolution and thousands years prior, to 406 ppm as of January 2017.[7,8] CO_2 act as a green house gas, and the rapid release has significantly contributed to the increase in average global surface temperature. From 1880 to 2012 the temperature increased with 0.85 °C and the last three decades have been successively warmer than any decade since 1850. As a consequence of this seemingly modest temperature increase, extreme weather phenomena have become more common and some areas have already experienced changes in cli-

mate.[9] The consequences disrupt the geopolitical situation in vulnerable areas, as heat waves, draughts, floods, heavy precipitation, or extreme winds can turn inhabitable and fertile areas into inhabitable ones.

1.1.2 Renewables

Recent years have shown a tremendous growth in the deployment of renewable energy sources. The rollout of renewable energy technologies significantly change the energy sector, which is steering towards a new paradigm shift as the energy costs associated with renewables becomes directly competitive with traditional fossil resources. Wind and solar power is being employed at unprecedented rates, and solar energy from photovoltaics is already regionally cheaper than coal, and is projected to undercut coal and natural gas prices for electricity generation worldwide by 2020.[10] This is great news, but the intermittent nature of these primary variable renewable energy sources gives rise to its own set of problems. Electrical energy storage is notoriously difficult in the gigawatt scale, and unlike the residential and industrial sector, the entire transport sector is almost exclusively dominated by liquid fuels. Renewable electricity sources currently have a hard time penetrating into these markets due to lack of competitive technologies. As of 2012, the transport sector was responsible for 25% of the worlds energy consumption with 96% of the energy goods being liquid fuels.[2] 92.4% being from oil with 2014 numbers.[1]

In Denmark in 2015, renewables (here sun, wind, hydro, biomass, and biogas) amounted to 56% of the electricity production, with wind being the dominant source with a share of 41.8%.[11] Wind power as a prime example however, fluctuates significantly over the course of a year, and will at times provide nothing, and can at other times cover more than 100% of the electricity consumption.[12] Hence the electricity has to be either stored, exported, or curtailed. Curtailment is essentially lost energy during overcapacity, as some wind mills are stopped to prevent overproduction and ensure grid stability. Solar energy behaves analogously, but with different patterns in fluctuation. The issue remain the same as for wind energy, as production and consumption does not match very well. This is both over the course of a year, but also on shorter time-scales of minutes, hours, or days.

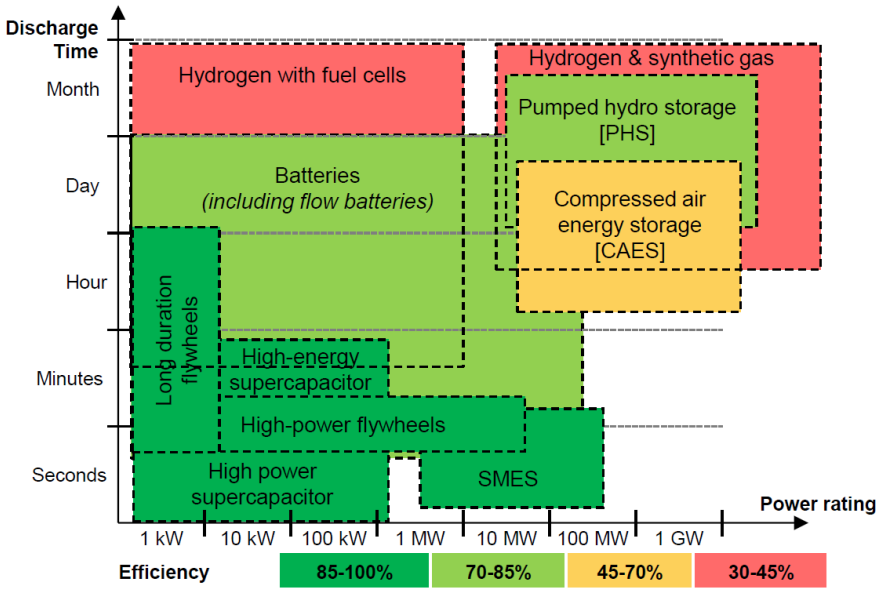

Fig. 1.1: Scheme of energy storage technologies in a power and time scale context. SMES: Superconducting magnetic energy storage. From [14].

1.1.3 Energy storage and distribution

As countries continue to increase the penetration of variable renewable energy in their energy production the issues of large scale energy storage become increasingly important. A large range of technologies already exist, each with their own set of benefits and limitations. In an electricity context, the two key parameters to consider when evaluating technology for system integration are the total power and the timescale. Figure 1.1 illustrates how different options fit into this scheme. For load levelling, short term storage and for end-users batteries excel, but at large time and power scales hydrogen may have some merit. In 2010 numbers the worldwide installed grid-connected electricity storage were in the magnitude of 140 GW, of which 99% were pumped hydro storage,[13] however the numbers don't show the total energy available.

Besides the primary electricity production and related storage, liquid and gaseous fuels for transportation and industrial processes, as well as heat-energy also constitute a significant part of the full energy matrix. In general there are little linkage between *heat*, *electricity*, and *liquid and gaseous fuels*, beyond perhaps co-generation of electricity and district heating. Ultimately, the carbon footprint needs to be reduced in all systems and across all sectors, including *transporta-*

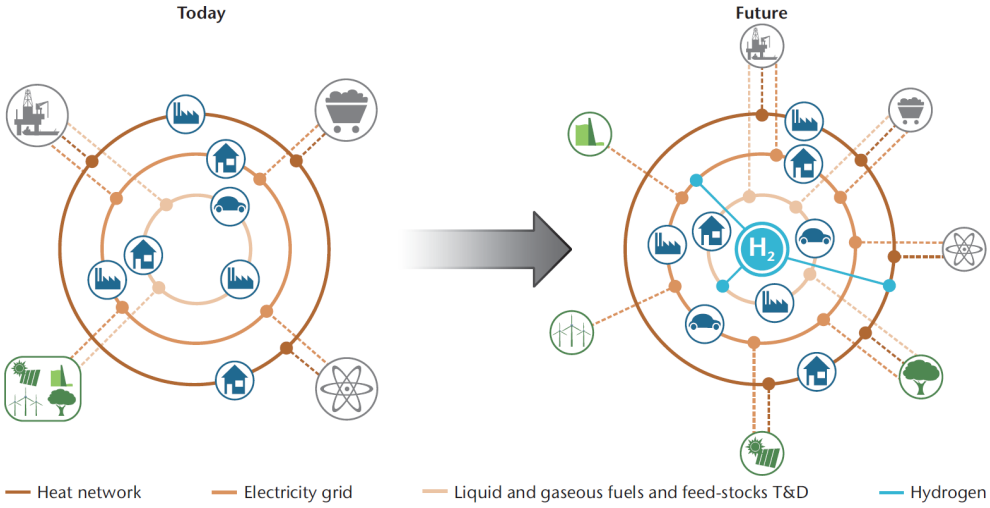

Fig. 1.2: The energy matrix of today and in the future. Primary sectors are transportation/mobility, industrial use, and residential/buildings/heating. Most energy transmission and distribution is in the form of either heat, electricity, or fuels, liquid and gaseous. In the future hydrogen may work as a link between the different energy form, and enable variable renewable primary energy sources to penetrate into all branches. T&D: Transmission and distribution. From [15].

tion, *residential*, and *industrial*. In this context hydrogen makes for an interesting player, as it can link the different branches, and in the grand scheme act as a very flexible resource. Figure 1.2 illustrate the current and potentially future energy matrix.

1.2 Hydrogen as an energy vector

Hydrogen is versatile as an energy carrier, but does not represent a primary energy source. This must be emphasized, particularly when discussions fall on electrical round-trip efficiency where all hydrogen based *power-to-power* pathways show low final efficiency,[15] see Figure 1.3. In broader numbers and not limited to electricity, chemical hydrogen storage has a 22-50% efficiency whereas e.g pumped hydro storage (PHS) is 50-85% and batteries 75-95%.[13] Consequently, purely in terms of efficiency, hydrogen is not the ideal medium.

Where hydrogen really shines is when surplus energy from variable renewables such as wind and solar is used to generate hydrogen from water electrolysis. The value lies in the ability to convert renewable power into green chemical

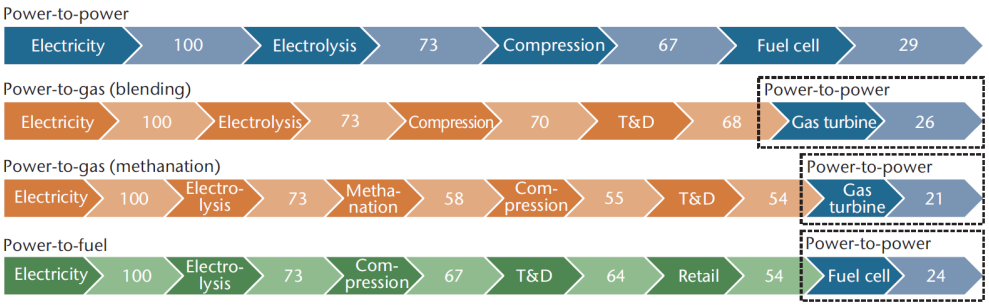

Fig. 1.3: Independent on pathway, hydrogen energy storage round-trip efficiency is low, even if every step is improved. Power-to-power is grid-to-grid electricity, whereas power-to-fuel represent hydrogen as a fuel for fuel cell electric vehicles (FCEV). Conversion efficiency is based on the higher heating value except for gas turbines. From [15].

carriers, either as pure hydrogen or higher hydrocarbons. Green hydrogen together with bioenergy represents the only renewable source for chemical energy carriers, and it helps bridge the different branches in the energy-supply system. In e.g. the transportation sector, battery driven electric vehicles (BEV) are slowly reaching market maturity, but are mostly suited for short to medium distance and light duty vehicles. Batteries are not suited for heavy duty and long haul transportation as in lorries, shipping, or flight. In cases of *power-to-gas*[16] and *power-to-fuel*, green hydrogen is essential for the products to be meaningful in a carbon emission context, and for *power-to-feedstock* in the refining and steel industry it is needed to significantly reduce emissions.[15,17]

1.2.1 Hydrogen production

Only a fraction of todays hydrogen production is through water electrolysis. In 2008, 4% was made by electrolysis, whereas the rest was produced from fossil fuels, by share; natural gas 48%, oil 30%, and coal 18%.[14,18]

Water electrolysis

Water electrolysis technologies are conventionally grouped into three categories; alkaline, PEM, and solid oxide (SO), each distinguished by their key characteristic: Alkaline electrolysis using concentrated alkaline aqueous electrolyte, either NaOH or KOH. PEM, short for polymer electrolyte membrane or proton ex-

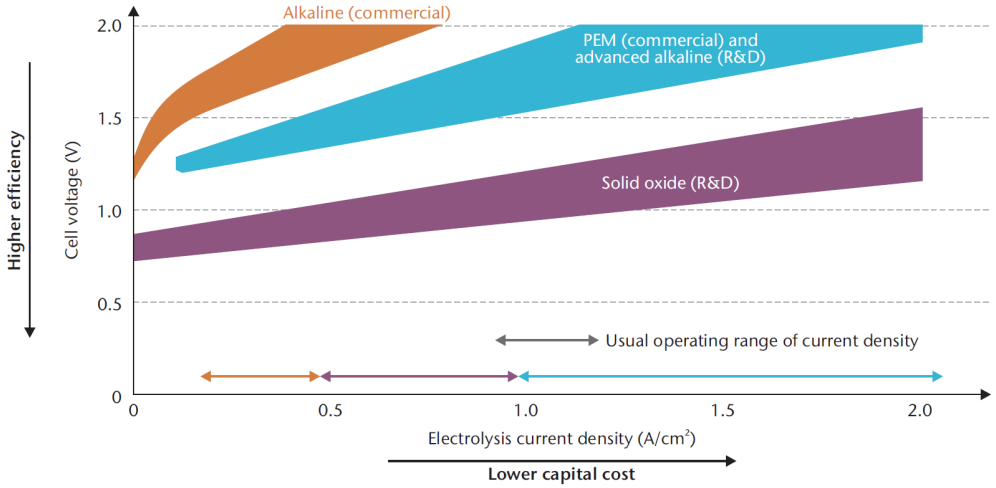

Fig. 1.4: Water electrolysis performance range. In terms of raw current-potential characteristics alkaline is inferior to PEM and solid oxide. From [15], adopted from [19].

change membrane, using proton conducting polymeric membranes. And solid oxide, using ceramic electrolytes and operating at high temperatures. Each is described in detail in Section 2.1. They each offer significantly different performance in regards to efficiency and come with their own set of advantages and disadvantages. In brief, alkaline performs the worst, but is cheap and mature. PEM is at early market stages, with higher performance and higher costs, while solid oxide is still at research level, but offer high performance at stable conditions. Figure 1.4 illustrate the conventional performance and operating range for the three classes of water electrolyzers, as presented by the International Energy Agency's 2015 Technology Roadmap for Hydrogen and Fuel Cells.[I]

1.3 Project objectives

The ultimate goal of this project is to move the performance of alkaline electrolysis from the classic alkaline range to that of PEM, which quite fittingly is also labelled as advanced alkaline cf. Figure 1.4 (■→■). A fitting target is 2000 mA cm^{-2} at 2.0 V. The present approach is to apply proven, as well as novel electrodes based on recent developments, in a zero-gap configuration with novel

[I]The low current density range performances presented here are at lower potentials than actual systems, but the differences are well illustrated.

polymeric alkaline-compatible membranes. The key novelty arise from the use of alkaline membranes, which are poised replace conventional porous separators previously used in alkaline electrolysis. The use of thin membranes over thick porous separators can reduce ohmic losses in the system, improve gas separation and dynamic operation properties, and enable the use of porous-type electrodes in a zero gap configuration. All together this should allow for higher operating current densities and higher efficiencies, both with the long term potential of reducing the capital costs of green and clean hydrogen generating systems. Consequently, the work concluded fall into three categories:

- Testing of alkaline electrolysis cells in general and the affiliated engineering involved. Design and construction of test station, cell housing, gasket configurations, and setup of equipment and programming for autonomous electrochemical measurements and electrolyte management.

- Evaluation of novel membranes under real cell conditions, under varying alkaline concentrations, temperatures, and with different electrodes. Both short term tests for initial performance, and longer term evaluation of stability and degradation effects.

- Development of electrodes using novel concepts, materials, or compositions. This involves using the knowledge documented in recent literature, with modifications necessary to fit into real cells. Ideally, a powder-based-type porous-electrode preparation route with catalyst flexibility is established.

1.3.1 Thesis outline

This thesis is intended to cover the scientific work carried out over the 3 years of the PhD programme. This includes work published in scientific journals, as well as work not comprehensive enough for journal publication. The contents are structured into 6 chapters:

1. **Introduction:** The topic of this project is tiny in the grand scheme of things. This chapter attempts to motivate why this work is important, and how it fits into the greater context.

2. **Water electrolysis:** The theoretical framework and the current technology status is outlined in this chapter. This includes an overview over water electrolysis systems, theoretical fundamentals, and an up-to-date literature review of the specific components in the alkaline system.

3. **Experimental alkaline electrolysis:** As the work is heavily experimental, a chapter is dedicated to this. The default equipment is specified, and cell testing framework described. Some considerations regarding cell and test station configuration is touched upon.

4. **Results with PBI membranes:** Membrane work in the context of this project is mostly connected to cell tests and performance. The development, synthesis, and other characterization is part of a collaboration. Presented here are primarily cell test results with membrane performance in focus.

5. **Results on active electrodes:** The various work related to anode and cathode development is presented in this chapter. This includes experimental work, half and full cells, as wells as physical and chemical characterization. Two approaches are followed, the first is to apply various coatings to macro-porous nickel foam substrates, and the second is to prepare porous electrodes from powders.

6. **Conclusion & outlook:** The overall findings of the project is summarized, and some proposed paths for future research work are outlined.

2

Water Electrolysis

Before diving into specifics it seems essential to present the core of electrochemical water splitting. An electrochemical cell consists at its very basic of an anode, a cathode, and an electrolyte. A set of redox reactions are separated and by definition oxidation takes place at the anode, and reduction at the cathode. The electrolyte provides an ionic pathway between the electrodes, while inhibiting electronic conduction. Since electrons take part in the redox reactions there must be an electronic pathway for reactions to proceed. If the total reaction is thermodynamically favourable it is spontaneous and can drive a current. This enables work to be done as in e.g. a fuel cell or during discharge in a battery. Vice versa, energy can be supplied by an external current supply to drive reactions the opposite way as done in electrolysis or while recharging a battery.

For water electrolysis the reactant, water, is electrochemically split into its molecular constituents, hydrogen and oxygen, by driving the reaction energetically uphill by means of an external power supply. The reactions depend on the ionic charge carrier and different reaction schemes exist for different systems. In most cases of aqueous electrolytes this means that the reactions are pH dependant and vary between acidic and alkaline condition.

$$\text{Anode:} \quad H_2O \longrightarrow 2\,H^+ + 2\,e^- + \frac{1}{2}\,O_2 \qquad E^\circ = 1.23\,V \qquad \text{(acidic)} \quad (2.1)$$

$$2\,OH^- \longrightarrow H_2O + 2\,e^- + \frac{1}{2}\,O_2 \qquad E^\circ = 0.401\,V \qquad \text{(alkaline)} \quad (2.2)$$

$$\text{Cathode:} \quad 2\,H^+ + 2\,e^- \longrightarrow H_2 \qquad E^\circ = 0.0\,V \qquad \text{(acidic)} \quad (2.3)$$

$$2\,H_2O + 2\,e^- \longrightarrow H_2 + 2\,OH^- \qquad E^\circ = -0.8277\,V \qquad \text{(alkaline)} \quad (2.4)$$

$$\text{Total:} \quad H_2O \longrightarrow H_2 + \frac{1}{2}\,O_2 \qquad E^\circ = 1.23\,V \quad (2.5)$$

Standard potentials are specified vs. the standard hydrogen electrode (SHE).

Since the reactions are different, it is not surprising that there are major differences between the reaction kinetics in the two environments. However, as the complete reaction is the identical, the general thermodynamics governing the process is the same.

As a practical note, the cathode will generally appear left of, or prior to the anode, both in figures and in text, and bear in mind, that the work of this thesis is concerned only with the alkaline environment.

2.1 Technologies

To grasp the context of alkaline water electrolysis as a topic, it is worth providing a brief review over the different competing types of water electrolysis. Different types of water electrolyzers are, similar to fuel cells, classified by their electrolyte and charge carrier. Conventionally three systems are discussed: *Alkaline electrolysis* (AE/AWE), with liquid alkaline electrolyte transporting OH^--ions, often supported by a porous diaphragm to help separate evolved gasses. *Proton exchange membrane* or *polymer electrolyte membrane* electrolysis (PEM) using polymeric proton conducting (H^+-ions) membranes. PEM is occasionally referred to as *solid polymer electrolyte* electrolysis (SPE). Both alkaline and PEM operate at temperatures below 100°C. The third type, solid oxide electrolysis (SO/SOE) uses ceramic materials and work at high temperatures in the range 500-1000°C where ${O_2}^-$-conduction is possible. However, this conventional classification is

somewhat inadequate when discussing new electrolyzer concepts such as membrane based alkaline electrolysis or proton conduction solid oxide electrolysis.

2.1.1 Alkaline electrolysis

Classic alkaline electrolysis is a mature technology and has seen MW-scale commercial use since the early the 1900-ies.[20,21] It was developed to be robust rather than efficient. Although commercially available for a long time, it has not reached large scale deployment. It cannot directly compete on economic terms with steam reforming, and the demand for green hydrogen has only recently increased. Nevertheless, it remains the dominant water electrolysis technology on the market as the alternatives are only slowly reaching market maturity.

The cells apply plates, perforated plates, or expanded meshes as anode and cathode, which are separated by a diaphragm. In conventional systems there is a gap between electrodes and the porous diaphragm, which can be as much as 42 mm.[22] In addition to this gap, the diaphragm itself contributes with a significant inter-electrode distance > 500 µm. In between, strong alkaline electrolyte (> 4 M) such as NaOH (aq) or KOH (aq) is circulated through both electrode chambers and is immobilized in the diaphragm where it provides the necessary ionic conductivity. The concept is schematically illustrated in Fig 2.1. The working temperature of most systems lie in the range 60-90°C, depending on source.

Keywords often associated with alkaline electrolysis are *proven*, *cheap*, and *inefficient*. Proven since it has been on the market for a century. Cheap since it does not require noble metal catalysts, but can use nickel and cobalt based transition metal and transition metal-oxides as catalytic coatings. And inefficient since it has large internal resistance, hence a limited current density range. The *cheap*-part is why it is interesting as topic, and the *inefficient*-part is where research is needed. Most, if not all, disadvantages with the alkaline systems somehow relate to the use of a porous diaphragm and liquid electrolyte. As gas evolution takes place on the electrodes, the volume between electrode and diaphragm is filled with gas bubbles. While NaOH (aq) and KOH (aq) both have very high ionic conductivity, the large inter-electrode distances and the significant blocking effect of gas bubbles result in very high ohmic losses, which limits operation to the sub 500 mA cm^{-2} range. On top of this, the porous nature of the diaphragm is not ideal in terms of gas separation. It prevents differential pressure

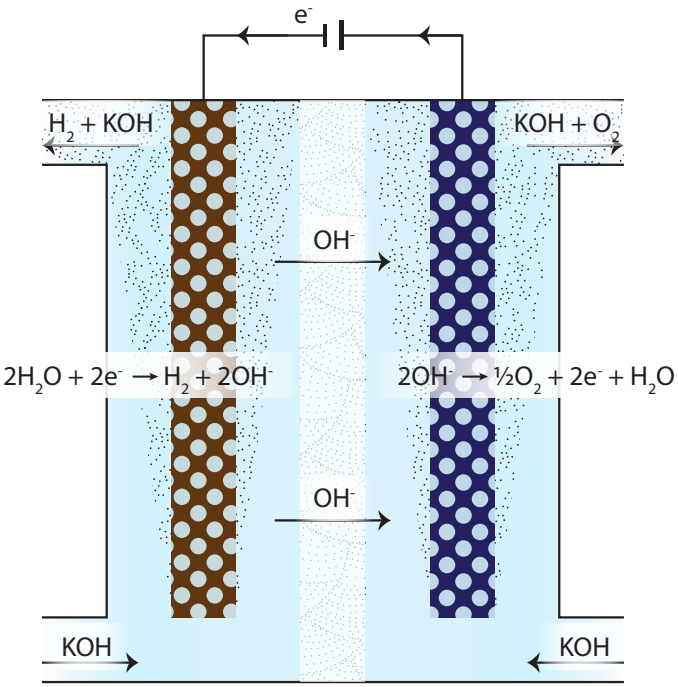

Fig. 2.1: Working principle of a traditional alkaline electrolysis cell. Working temperature 60-90°C. Aqueous KOH 15-30 wt% is circulated through the cell. Cathode left, anode right.

operation, and since it is a porous material it must be of a certain thickness to limit gas mixing. Furthermore, the highly corrosive alkaline electrolyte is tough for auxiliary equipment, and ideal systems would use dilute (< 1 M) alkaline electrolyte or pure water.

Consequently, some research have gone into finding improved materials and better cell design. For a long time asbestos cloths were used as diaphragm, but asbestos is toxic and suffers from stability issues at high temperatures.[20,23,24] Different alternatives have since been investigated: Sintered nickel oxide;[25,26] polyantimonic acid[26–28] and zirconium oxide[26,29] based composites, with polymeric binders such as polysulfone (PSU) or polytetrafluoroethylene (PTFE); and polymeric cloths based on polysulfones,[24] polyphenylenesulfide (PPS),[23,30] or sulfonated poly(etheretherketones) (SPEEK).[31] Current state-of-the-art is a commercially available polysulfone/zirconium oxide-composite symmetrically coated on a polymeric mesh with the trademark name *Zirfon*.[29] Zirfon is specified to be stable in 6 M KOH (aq) at up to 110 °C. Further separator improvements in alkaline electrolysis are expected to come from the development of anion-

exchange membranes (AEM) or ion-solvating alkaline membranes.[32]

Anion exchange and alkaline polymer electrolyte membrane electrolysis

Introducing a polymeric membrane - anion-exchange or ion-solvating - and employing a zero-gap configuration move the alkaline system towards the PEM system in terms of components and cell structure. To better distinguish between alkaline concepts they can be grouped in three subcategories. Classic alkaline, alkaline polymer electrolyte membrane (APEM), and anion-exchange membrane (AEM).

APEM is in many ways like classic alkaline, except the diaphragm is substituted with a polymeric membrane. Zero-gap configurations with porous electrodes can be applied, but KOH (aq) or similar electrolyte is still necessary to provide ionic conductivity. This type can efficiently utilize foam or mesh-based electrodes. Figure 2.2a illustrate the concept with foam-type electrodes. The work in this thesis primarily fall under this category, and it certainly belong to the alkaline electrolysis category.

AEM on the other hand has a close resemblance to PEM. While the environment within the membrane is alkaline (OH^--conducting), and non-noble metal catalysts are an option, it does not require alkaline electrolyte but rather can operate with pure water. This adds the requirement that electrodes offer anionic pathways, similar to what is necessary in conventional PEM electrolysis. This is arguably *polymer electrolyte membrane* electrolysis, but no consensus exist within literature with regards to the PEM abbreviation. This type is normally referred to as AEM, whereas PEM is restricted to proton-conducting polymeric electrolyte membrane systems. The concept is illustrated in Figure 2.2b, with electrodes consisting of a catalyst layer near of the membrane, and a porous transport layer (PTL) to support this and provide better electronic pathways.

An in-depth review on electrode materials and catalysts is presented in Section 2.3, and details on state-of-the-art alkaline membranes is covered in Section 2.4.

High temperature and pressure alkaline electrolysis

A novel and slightly different approach within alkaline electrolysis is the use of much higher temperatures. Kinetics and ionic conductivities generally increase

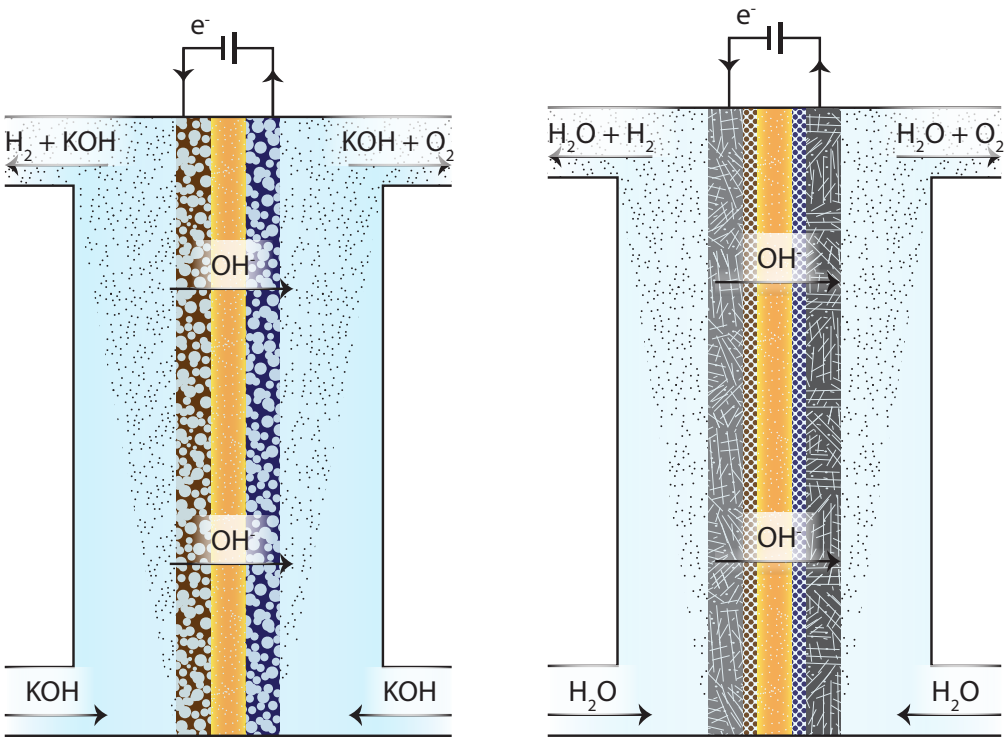

(a) APEM **(b)** AEM

Fig. 2.2: Membrane-based alkaline electrolysis concepts. **(a)** APEM, here using electrodes with macro-porosity without the need of an ionomer. **(b)** AEM, since an-ionic pathways are necessary, electrodes consist of an ionomer/catalyst layer, and a porous transport layer. Cathodes left, anodes right.

drastically with temperature, but normal alkaline electrolysis is restricted by the boiling point of the liquid electrolyte and material stability concerns. However, with high pressure (~ 40 bar) operation up to 250°C is possible. At these temperatures KOH solution can be immobilized by a porous ceramic material to form an electrolyte system, which at high temperatures show high ionic conductivity.[33] Using either silver catalyst on nickel or nickel alloy foam based electrodes, with an yttria-stabilized zirconia electrolyte matrix;[34,35] or cobalt and molybdenum activated nickel foam electrodes and a strontium titanate electrolyte matrix,[36] very high current densities can be reached at high efficiencies. More than 1 A/cm^2 can be achieved at 1.5 V.[36]

2.1.2 PEM electrolysis

PEM electrolysis was introduced in its modern form as a concept in the late 1980-ies, as the first and most common type of solid polymer electrolyte (SPE) electrolysis.[37,38] Unlike alkaline, which have been available for a century, MW-scale PEM has only recently reached market maturity, although small systems have been available for about 20 years.[39] PEM systems promise high efficiency, high partial load range, short response time, and high hydrogen purity. However, this come at the cost of very expensive systems with scarce platinum group metal (PGM) catalysts, and expensive and difficult to process materials.[40]

The most widely used solid polymer electrolyte in PEM systems is perfluorosulfonic acid-type (PFSA) membranes, such as the well known Nafion, capable of conduction protons (H^+). The immediate vicinity of the membrane is strongly acidic, and as a consequence only a limited selection of noble PGM metals can act as stable catalysts. Cathodes are made from carbon supported platinum catalysts (Pt/C), and anodes are iridium or ruthenium oxide based catalysts supported by a titanium felt or similar material.[40] PEM electrolyzers operate with pure water and commonly only on the anode side, hence the ionic pathways in the electrode must be provided by an ionomer mixed into the catalytic layer. The concept is illustrated in Figure 2.3. Normal working temperature for PEM systems are in the range 50-80°C.[40]

While PEM show extraodinary electrochemical performance, and can reach 2-6 A/cm^2 at 2 V depending on membrane thickness ($\sim 50 - 200$ µm)[41] it is not without some issues. The acidic nature of the membrane together with the large oxidizing potentials limit catalyst options to noble metals.[39] Expensive and scarce platinum and the even more scarce iridium are currently used for cathodes and anodes respectively. Iridium, a side product of platinum production, is only produced in small amounts annually and it can be imagined to become a limiting factor if gigawatts of PEM electrolyzers are to be deployed. While it is apparently not an issue of concern for commercial PEM eletrolyzer companies yet, a rough estimate of total deployment potential can be made.

Consider a 1 MW system (Inspired by a ITM Power PEM electrolyzer system), with 3 stacks of 100 cells, with cell size 60×30 cm^2. Nominal operating conditions of 1.8 V and 1 A/cm^2 fit approximately with this. Assuming a loading of 2.2 mg/cm^2 IrO_2 it requires approximately 1 kg iridium per 1 MW. Taking 9

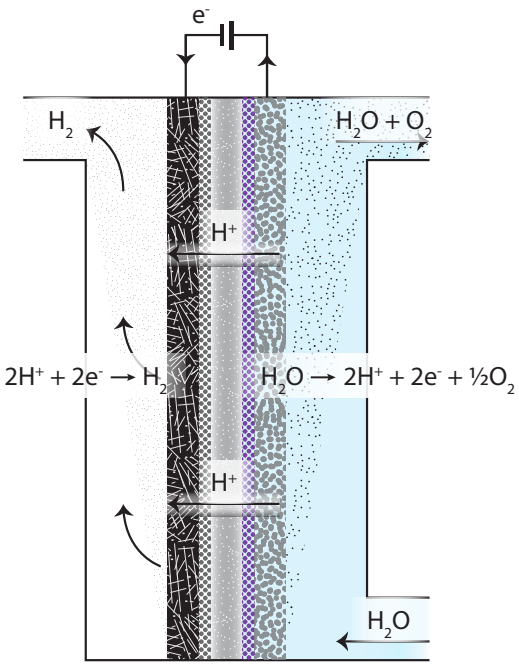

Fig. 2.3: Working principle of a PEM electrolysis cell. Common working temperature 40-80°C. Cathode left, anode right.

t/yr[42] as annual iridium production, this is at most 9 GW/yr. This is disregarding any other applications for iridium which is unlikely. Babic *et al.* estimate 2 GW/yr, with long term improvements enabling up to 100 GW/yr based on slightly different assumptions.[39]

Although the primary contributor to stack costs is the bipolar plates (51%[43]), significant work is directed towards the catalysts[I]. Some research has looked into alloying iridium or ruthenium in e.g. pyrochlores[45] or with tin,[46] or simply at reducing the catalyst loading without compromising the performance. The carbon (cathode) or titanium (anode) catalyst support which act as a porous transport layer and help by providing electronic pathways is another important cell component. The carbon felts of the cathode are cheap and reliable. However, the titanium materials at the anode is problematic. They are difficult and expensive to process, and they oxidize over long term cell operation. Consequently, the contact resistance increase and performance decrease. Lastly, the hydrogen permeability of Nafion is strongly dependent on partial pressure difference. Since pressurized operation is stated as an advantage for PEM over alkaline,

[I] According to a recent conference contributions [44], this is not the case any longer.

it necessary to point out the relatively poor membrane performance in this regard.[39,41,47] Thus, to adhere to safety requirements commercial systems may employ recombination catalysts (platinum in the anode), and thicker membranes than otherwise desired. As such, the afore mentioned 6 A/cm^2 at 2 V is not realistic under current commercial conditions. For a broader overview, Carmo *et al.*[40] (2013) provide a comprehensive PEM electrolysis review and Babic *et al.*[39] (2017) thoroughly discuss all the issues of current state-of-the-art systems.

2.1.3 Solid oxide electrolysis

Solid oxide electrolysis is the least mature among the three primary types of water electrolysis, and is at present stage purely at a R&D level. Characterised by very high operating temperatures, 750-900°C, these electrolyzers are fed with steam rather than liquid water. At these temperatures a whole different set of materials is necessary, and the thermodynamics of the water splitting process is significantly different. Much higher electrical efficiency can be achieved as kinetics are faster and as the reversible electrochemical cell potential is decreased.

The electrolyte and electrodes are made from ceramic or ceramic/metallic composites. At high temperatures the electrode conduct oxygen ions (O^{2-}) through oxygen vacancies in the ceramic crystal lattice. The electrodes are gas-diffusion type electrodes, as steam and product gasses must be able to diffuse in and out easily. As the membrane as well as both electrodes are very thin and made from brittle ceramic material, the entire cell is normally supported by an increased cathode layer thickness to help mechanical integrity. The concept is illustrated in Figure 2.4.

The most common electrolyte material is yttria (Y_2O_3) stabilized by zirconia (ZrO_2), YSZ. Commonly with an 8 mol% substitution ratio. Electrodes are composite electrodes of electronic and ionic-conducting materials, and reactions only take place at the triple phase boundary (TPB) between the two conducting materials and the gas phase. Hydrogen electrodes are made from metallic/ceramic composites (cermets), with Nickel/YSZ being most frequent. Platinum is useful in model studies but not feasible from a commercial point of view. For the oxygen electrode perovskite-type ($ABO_{3-\delta}$) ceramics are mixed with YSZ. Most commonly strontium-doped lanthanum manganite (LSM), but also strontium doped lanthanum cobaltite (LSC) and with additional iron sub-

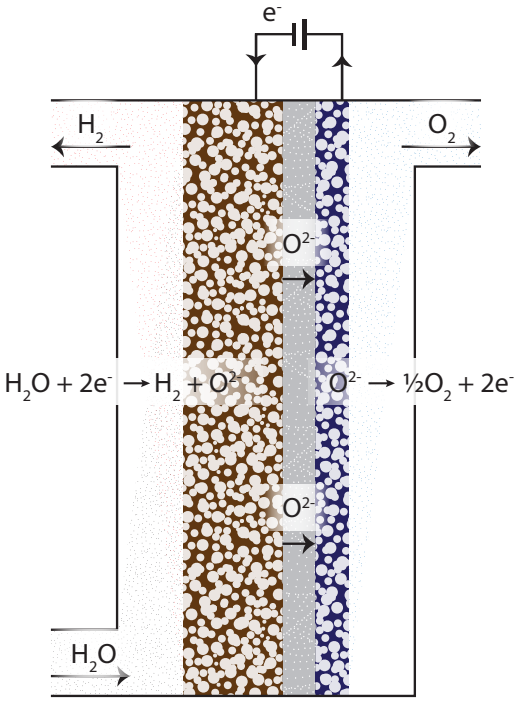

Fig. 2.4: Working principle of a solid oxide electrolysis cell. Working temperature > 750°C. The high temperature enables oxygen-ion conduction by means of vacancies in the ceramic material of the electrolyte. Water is supplied as steam. Cathode left, anode right.

stitution of cobalt (LSCF). A wide range of other materials are investigated in literature, but the Ni/YSZ | YSZ | LSM/YSZ remain the most common configuration.[48]

It should be noted that high temperature electrolysis has some opportunities beyond water electrolysis. Co-electrolysis in which CO_2 is introduced as reactant and reduced to generate syn-gas (H_2 + CO) is possible, but is a topic on its own and will not be addressed further.

High temperature proton conductors

Solid proton conducting electrolysis is conceptually similar to normal solid oxide electrolysis, except that the charge carrier is H^+ rather than O^{2-} and steam is fed to the anode. Materials are primarily ceramics, but rather than YSZ, the protonic conductors are based on perovskites such as $SrCeO_3$, $BaCeO_3$, and $BaZrO_3$ where the B atom is replaced by trivalent cations such as Y, Yb or Nb, e.g. yttria-

doped barium zirconate.[48]

As with conventional solid oxide electrolysis, co-electrolysis is also an option. Here, CO_2 is also introduced on the cathode, and can in principle be used for direct formation of methane.[49]

Intermediate temperature proton conductors

Another type of water electrolysis can be performed at intermediate temperatures (200-400°C) using solid acids such as CsH_2PO_4 or $Sn_{0.9}In_{0.1}P_2O_7$ as electrolyte.[50] This field is however, at very early stages of research hence not much is published and the concept is largely unexplored.

2.2 Theoretical framework

2.2.1 Thermodynamics

During water electrolysis energy is converted from electrical energy to chemical energy. In our case in the form of hydrogen, since oxygen is readily available from the atmosphere for most applications. The chemical energy obtained corresponds to the difference in enthalpy of formation $\Delta_f H$ between reactant (H_2O) and products (H_2 and O_2). However, since the entropy is changed during gas evolution reactions, the governing thermodynamic entity describing the equilibrium of reactions is the Gibbs free energy ΔG of the reaction, which at constant temperature and pressure is given by

$$\Delta G = \Delta H - T\Delta S\,. \tag{2.6}$$

Here T is the temperature and ΔS is the difference in molar entropy. When the change in Gibbs free energy is negative the reaction is thermodynamically spontaneous. Conversely, if ΔH is positive energy must be supplied to drive the reaction, and energy corresponding to ΔG must be supplied as high quality energy such as work. Relevant thermodynamic quantities at standard conditions are summarized in Table 2.1, with $^\circ$ denoting standard values. The enthalpy of formation of H_2 and O_2 are zero, whereas for water it has a negative value. Hence, the Gibbs free energy (ΔG) and the enthalpy (ΔH) associated with the water splitting reaction are identical to the negative energies of formation for

water.

$$\Delta G = -\Delta_f G^\circ_{H_2O(l)} = 237.1\,\text{kJ/mol} \tag{2.7}$$

$$\Delta H = -\Delta_f H^\circ_{H_2O(l)} = 285.8\,\text{kJ/mol} \tag{2.8}$$

Reacting H_2 with O_2 is thermodynamically spontaneous and can liberate chemical energy (fuel cell or combustion), whereas the opposite reaction require external energy input (electrolysis).

Table 2.1: Thermodynamic quantities at standard temperature and pressure (STP), $T = 298.15$ K, $p = 1$ bar.[51]

	$\Delta_f H^\circ$ kJ/mol	$\Delta_f G^\circ$ kJ/mol	S° J/(mol K)	C_p° J/(mol K)
H_2	0	0	130.7	28.8
O_2	0	0	205.2	29.4
H_2O (l)	-285.8	-237.1	70	75.3
H_2O (g)	-241.8	-228.6	188.8	33.6

As water splitting increase entropy through the formation of gas, the $T\Delta S$ term is positive and contributes towards making the reaction progress more easily as it decrease the Gibbs free energy. As a consequence, the cost in energy supplied as work required to drive the reaction is less than the energy available by combustion of hydrogen. This enable water electrolysis to operate at electrical efficiencies above 100%. Although rarely feasible in practice for alkaline systems due to kinetics, it is practically possible at high temperatures with free heat energy available. That a fuel cell or combustion process cannot convert back all the energy available in hydrogen into work or electrical energy is a different aspect. Fuel cells suffer the same entropy-driven energy penalty and is also kinetically limited, whereas combustion processes are limited by the carnot efficiency.

Temperature dependence

Increasing temperature has a profound effect on the equilibrium and kinetics of chemical reactions. Water splitting is no exception. While this work is solely looking into water electrolysis, solid oxide technology and other high temperature techniques operate with steam electrolysis, hence higher temperatures deserves a brief mention.

The equilibrium behaviour is, as discussed, governed by the Gibbs free energy given by eq. (2.6). The enthalpy of formation and the molar entropy are functions of temperature and the molar heat capacity, which in turn is also temperature dependent, albeit only slightly. For temperatures below 100°C one can assume C_p constant, but for much higher temperatures one should refer to tables or empirical formulas, e.g. [51–53]. The temperature dependency is expressed as:

$$H(T) = H^\circ + \int_{T^\circ}^{T} C_p(T)dT \approx H^\circ + C_p \cdot \Delta T \tag{2.9}$$

$$S(T) = S^\circ + \int_{T^\circ}^{T} \frac{C_p(T)}{T}dT \approx S^\circ + C_p \cdot \ln\frac{T}{T^\circ}\,. \tag{2.10}$$

Electrochemical water splitting

Water electrolysis is an electrochemical technique, which in essence means that the electron transfer reactions are separated at the anode and cathode. The energy associated with driving the reaction, *i.e.* the Gibbs free energy, can thus be expressed in terms of work performed by moving charges. Hence, a potential is associated with the reaction, which is induced between the electrodes. This is called the *reversible potential* E_{rev} or standard cell potential and is expressed in terms of the Gibbs free energy and the number of charges participating in the reaction n.

$$E_{rev} = -\frac{\Delta G}{nF}\,. \tag{2.11}$$

For water electrolysis $n = 2$ and $F = 96485\,\mathrm{C\,mol^{-1}}$ is Faradays constant. Hence, to drive the reaction a potential larger than E_{rev} must be applied for electrons to overcome the thermodynamic work needed by the reaction.

While the Gibbs free energy governs the equilibrium behaviour, the enthalpy of formation determines the generated potential chemical energy. The *thermoneutral potential* E_{tn} describe the potential at which the reactions occur isothermally, and is given in terms of the enthalpy of formation through

$$E_{tn} = -\frac{\Delta H}{nF}\,. \tag{2.12}$$

If reactions take place below the thermoneutral potential they are endothermic, while reactions above are exothermic. The reversible and thermoneutral potentials at relevant temperature conditions is provided in Table 2.2. The common working temperature in this work is 80°C.

Table 2.2: Reversible E_{rev}, and thermoneutral E_{tn}, cell potentials for various temperatures at standard pressure.

Temp.	[°C]	20	25	40	60	80
E_{rev}	[V]	1.233	1.229	1.216	1.120	1.183
E_{tn}	[V]	1.482	1.481	1.479	1.475	1.472

At a glance, it seems ideal to operate at the thermoneutral potential, but in practice heat is lost to the surroundings through e.g. thermal radiation and vapour leaving the system. To be self-sustaining on a system level, a slightly higher potential is necessary, to generate the excess heat which is otherwise lost. This can be denoted as the *thermobalanced potential* and depend on the type and size of system, pressurization, and operation specifics. Commonly this lie in the range 1.54-1.74 V for alkaline and PEM systems.[41] A deeper discussion of this is beyond the scope of the this project, and the reader is referred to the reference.

The thermodynamic temperature behaviour of the reaction at standard pressure is summarized in Figure 2.5.

Nernst equation

As temperature can influence the cell potential, so can pressurization and concentration of involved species. The equilibrium is described by the Nernst equation (2.13) where a_x represent the activity of the involved species.

$$E = E^\circ - \frac{RT}{nF} \cdot \ln \left[\frac{a_{H_2} \cdot {a_{O_2}}^{1/2}}{a_{H_2O}} \right] . \tag{2.13}$$

For gas phase reactions such as steam electrolysis, the activity is conveniently substituted by partial pressures. In dilute aqueous solutions the concentrations can be used and water taken as unity. However, a strong alkaline electrolyte is not dilute and gas is evolved during alkaline water electrolysis making it non-trivial to use.

Efficiency

The topic of efficiency is of course important when it comes to energy technology. The intuitive way to consider efficiency is to compare the energy you get

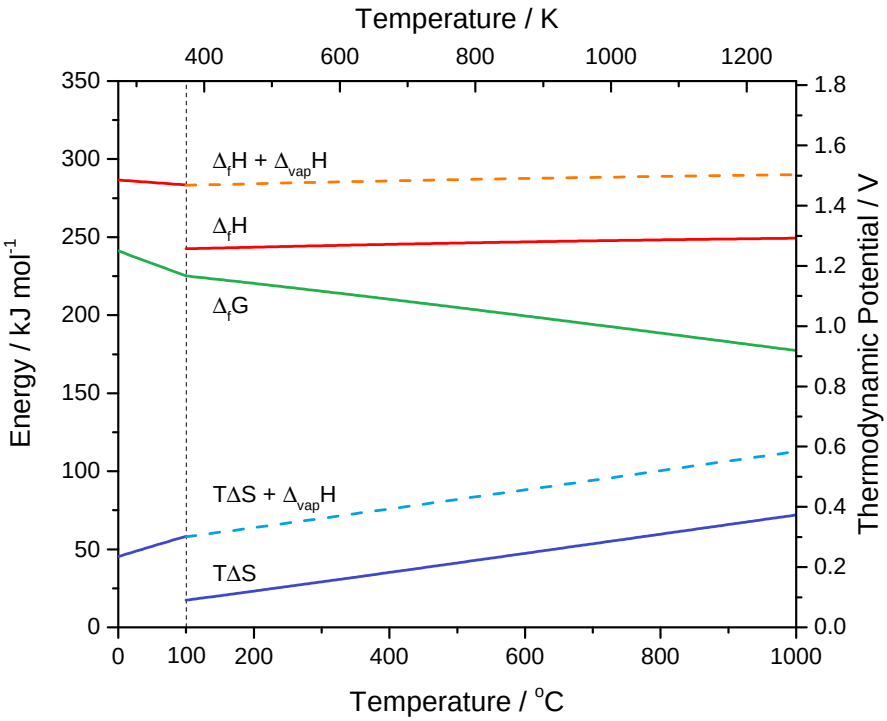

Fig. 2.5: Thermodynamic entities; Gibbs free energy $\Delta_f G$, enthalpy of formation $\Delta_f H$ and thermal energy $T\Delta S$, and their temperature dependence assuming liquid water at $T < 100°C$.

out versus the energy you put in. The energy you get is ΔH which can be expressed against a higher heating value (HHV), which correspond to a reaction forming liquid water ($\Delta H_{HHV} = -\Delta H_{H_2O(l)}$), or the lower heating value (LHV), corresponding to a reaction forming gaseous water ($\Delta H_{LHV} = -\Delta H_{H_2O(g)}$). The electrical energy provided is expressed in terms of the applied potential E_{cell}. For the HHV and LHV respectively, at standard conditions, efficiencies are expressed as

$$\eta_{HHV} = \frac{\Delta H_{HHV}}{nF}\frac{1}{E_{cell}} = \frac{1.481\,\mathrm{V}}{E_{cell}} \tag{2.14}$$

$$\eta_{LHV} = \frac{\Delta H_{LHV}}{nF}\frac{1}{E_{cell}} = \frac{1.253\,\mathrm{V}}{E_{cell}}, \tag{2.15}$$

However, this figure of merit is more accurately referred to as the voltaic efficiency or polarization efficiency and is a simplification of the cell. A full cell efficiency would take into account produced and lost hydrogen, and capture effects of crossover and recombination, which can be quite significant,[39,41] but this require more complex test systems to capture accurately. Hence, commonly

in electrochemical contexts and in academic literature the current-potential-behaviour (iV-curve or polarization-curve) is presented, as it effectively capture electrode performance, the ohmic behaviour of the electrolyte, and mass transportation effects. However, differentiating clearly between contributions from the different sources of overvoltage is non-trivial.

The faradaic efficiency, *i.e.* the fraction of electrons participating in water electrolysis contra parasitic reactions, is almost always assumed to be 100% under steady-state conditions in water electrolysis context. Current contributions from corrosion, nickel oxidation/reduction, anodic formation of hydrogen peroxide H_2O_2, or anodic carbon corrosion could contribute and are important in aspects of stability, but insignificant in a steady-state efficiency context.

In commercial context, the efficiency on a system or stack level is more interesting. Here the balance of plant (BoP), *i.e.* pumps, dryers, compressors and other auxiliary equipment plays a role, and the efficiency is expressed in energy per H_2 with units of kWh/kg or kWh/Nm^3.

To put things a bit into perspective. Assuming an operating potential of 1.8 V, (voltaic efficiency of $\sim$ 82%), faradaic efficiency of 100% and BoP efficiency of 85 % the energy costs amount to 4.58 kWh/Nm^3 and 56.31 kWh/kg respectively, in total $\eta \approx 70\%$[II].

Operational costs (opex) must always be balanced against capital cost (capex) and production capacity. Large systems operating a lower current densities will have a higher voltaic efficiency than small systems at high current densities. Normally alkaline electrolyzers have a lower capex, but higher opex compared to PEM electrolyzers.

2.2.2 Kinetics

Although thermodynamics lay the foundation for understanding water electrolysis, there is not much engineering to be done without significantly changing the system design. For instance, the reversible potential decrease only about 50 mV going from 20°C to 80°C. But while thermodynamics define the equilibrium behaviour it does not describe the behaviour away from equilibrium. To describe

[II] The Toyota Mirai with a range of approximately 500 km store about 5 kg of hydrogen in two tanks.[54] At danish *consumer* electricity prices[55] of $\sim$ 2.10 DKK/kWh that is about 590.00 DKK for a full tank. Not very impressive due to the high fees on consumer electricity.

this we need to look at reaction kinetics, and the losses that real systems suffer from during operation.

When the current and reaction rate increase, the potential increases correspondingly. The higher the current is, the larger the potential becomes and the lower the efficiency gets. The real cell potential E_{cell}, necessary to drive a given nominal current can in a simple model be separated into three fundamental terms representing different concepts. The thermodynamic reversible potential E_{rev}, the activation or kinetic potential E_{kin}, and the ohmic potential E_{Ω}.

$$E_{cell} = E_{rev} + E_{kin} + E_{\Omega} \tag{2.16}$$

Potential contributions beyond E_{rev} can be considered losses and should be minimized as much as possible. Kinetic losses are often called overpotentials η, and can be ascribed to each electrode, η_{an} and η_{cat}. These are unavoidable, but can be minimized by using active catalysts and large electrode surface area. Ohmic losses are proportional to the current and are caused by ohmic resistances in the electrolyte (ionic) and in the electrodes (electronic). Since the electronic conductivity is often orders of magnitude larger than the ionic conductivity, the ohmic contributions are often primarily ionic. Ohmic losses can be reduced by increasing ionic conductivity using novel materials, or by decreasing electrode distance by using e.g. thinner membranes. In a slightly expanded model, the cell potential is then described by

$$E_{cell} = E_{rev} + \eta_{an} + \eta_{cat} + I \cdot R_{\Omega} \tag{2.17}$$

Furthermore, gas evolution in liquid electrolyte give rise to bubble resistance, which conceptually is similar to mass transport losses in fuel cells. The formation of gas replace the liquid electrolyte locally, and can cover catalyst surfaces. This lead to higher ohmic resistances as the electrolyte volume is reduced and the ionic mean path distance is increased, as well as to higher kinetic losses as the effective surface area is decreased. However, in water electrolysis due to the high reactant-density of water (a liquid), sudden mass transport limitations as seen in fuel cells (gaseous reactants) are rarely observed even for very high current densities (> 4 A/cm^2). Hence, distinguishing bubble effects from the intrinsic kinetic and ohmic effects is not trivial. As a consequence, electrode properties such as hydrophilicity may appear to affect ohmic losses more than kinetic losses normally associated with electrodes.

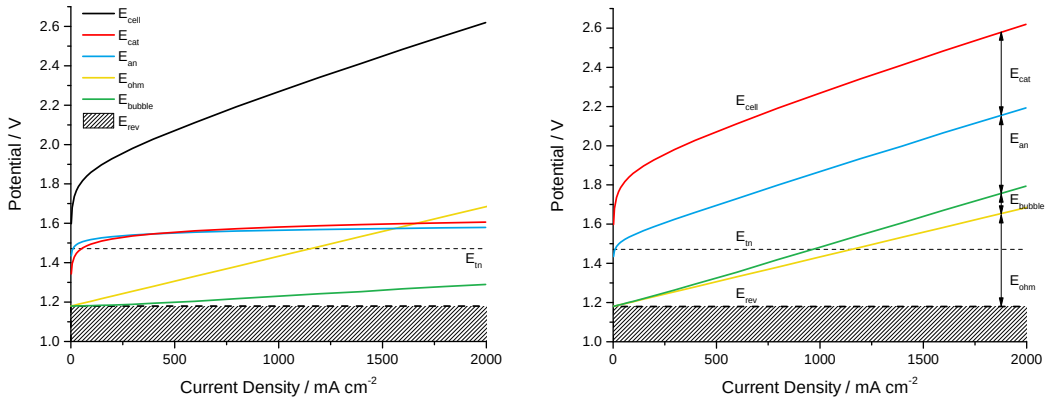

Fig. 2.6: Illustration of various contributions to the cell potential, **(a)** individual overpotentials, **(b)** cumulative overpotential.

A typical current-voltage curve (polarization curve) with arbitrary values is presented in Figure 2.6 to illustrate the contribution of different effects. E_{an} and E_{cat} can be reduced by using better catalysts, E_{ohm} with better or thinner membrane or separators, and E_{bubble} by using zero-gap configuration, or hydrophilic electrodes with better transport properties. The individual potential contributions are by themselves added onto the reversible potential in Figure 2.6a, whereas they are cumulatively added in Figure 2.6b. The relative contributions between anode, cathode and ohmic losses are highly electrode and membrane dependent and the graphs should be taken as an example. In e.g. PEM electrolysis, the cathode contribution is significantly lower than the anode contribution.

Butler-Volmer equation

Ohmic losses are straight forward, and are equivalent to the potential drop across a resistor when a current flows. They follow ohms law, are directly proportional to the current, and are increasingly important as current density is increased. At low current densities the main contributions to the overpotential come from the the electrode kinetics, *i.e.* the cost of pushing the system away from equilibrium conditions. The electrochemical reaction rate on a single electrode represented by a current density i, relates with the reaction overpotential η, through the Butler-Volmer equation:

$$i = i_0 \left[\exp\left(\frac{\alpha n F}{RT}\eta\right) - \exp\left(-\frac{(1-\alpha) n F}{RT}\eta\right)\right] . \tag{2.18}$$

i_0 is the exchange current density - equivalent to the equilibrium forward and backward current density at $\eta = 0$. The exchange current density is effectively increased by enlarging the active electrochemical surface area (ECSA), e.g. by increasing catalyst loading, employing porous structures, or increasing surface roughness. α is known as the charge transfer coefficient for which $0 < \alpha < 1$, but is often assumed to be 0.5. If this is a sound assumption is not necessarily true for alkaline water electrolysis.

As expressed by the equation, the reaction rate (and thus current density) is the difference between the forward and backward reactions. At equilibrium these are equal, but when the system is perturbed away from equilibrium, the overpotential η change and one of the exponential functions start to dominate resulting in a non-zero current. If far enough away from equilibrium, one of the terms become negligible, and the equation can be simplified:

$$i = i_0 \exp\left(\frac{\alpha n F}{RT}\eta\right) . \tag{2.19}$$

This can be rewritten to describe the overpotential in terms of current density

$$\eta = -\frac{RT}{\alpha n F}\ln(i_0) + \frac{RT}{\alpha n F}\ln(i) \tag{2.20}$$

$$= -\frac{2.3RT}{\alpha n F}\log(i_0) + \frac{2.3RT}{\alpha n F}\log(i) \tag{2.21}$$

$$= a + b\log(i) . \tag{2.22}$$

Equation (2.22) is known as the Tafel equation and is commonly used to fit electrode polarization data in literature. The coefficient

$$b = \frac{2.3RT}{\alpha n F}, \tag{2.23}$$

is known as the tafel slope and represent the change in current density per decade of overpotential increase. The constant

$$a = -\frac{2.3RT}{\alpha n F}\log(i_0), \tag{2.24}$$

is used to calculate the exchange current density i_0 which is a term for the equilibrium current.

Caution must be exercised when fitting electrode data to the tafel equation. Depending on current density regime, a change in rate limiting step can induce a

change in the tafel slope, and similarly will increased bubble coverage and blocking of the active surface diverge the measured data from the intrinsic behaviour. This is almost always observed at current densities above 100 mA/cm^2 relative to the apparent geometric electrode area, but often already at much lower current densities. Lastly, the limiting step of a reaction may be chemical and not electrochemical, or parasitic reactions may run concurrently in which case the model is misleading at best.

2.3 Electrocatalysis and electrodes

In the context of this work, two electrochemical reactions are of prime interest. The hydrogen evolution reaction (HER) taking place at the cathode in which water is reduced, and the oxygen evolution reaction (OER) at the anode where hydroxide ions are oxidized. For these processes to proceed rapidly with minimal losses, efficient electrocatalysts are necessary. This section seeks to provide an up-to-date literature review on electrodes and electrocatalysts for alkaline hydrogen and oxygen evolution. While electrodes and electrocatalysts are not the same thing, they are intrinsically connected and can hardly be addressed without one another.

The most important advantage of alkaline electrolysis over the strongly acidic environment present in PEM electrolysis is the option to use non-noble metals. In PEM electrolysis essentially all catalysts are Pt or Ir based, all of which are expensive and scarce.[39,40] In the alkaline environment a wide range of e.g. transition metal-based materials can be used. Primarily these are nickel, cobalt and iron-based, but not exclusively. In contrast to PEM, there are currently no well established go-to catalyst, and vast amounts of literature is being published on novel and less-novel materials. Hence, while this review is hopefully comprehensive it is by no means exhaustive. The included literature is selected in part on basis of the "*at a glance*"-relevance to cell applications. This means that there may be an overweight of good performing catalysts, and a lack of poorly working concepts.

A good electrode employ an active catalyst and have a large electrochemical surface area. Furthermore, it needs to get rid of evolved gasses efficiently (hydrophilicity), and have a good and uniform electronic conductivity. In a simplified framework, this is achieved in two ways. Either a catalyst powder is

prepared into an electrode through blending with organic binders and/or conductivity enhancing support materials. This can be processed in various ways, such as spraying, tape-casting, or pellet pressing. This type of approach is common in PEM fuel cells and PEM electrolysis, where a need for ionic pathways exists, which are established through the polymeric ionomer which co-function as binder. Alternatively, when a liquid electrolyte is present, a structured material such as nickel foam can be physically, chemically, or electrochemically coated directly. Naturally, preparation methods also exist that fall outside or inbetween these categories.

Good electrodes and electrocatalysts are evaluated against a set of criteria that to varying degrees must be fulfilled. Trasatti summarized these nicely.[56]

- High electrocatalytic activity towards the desired reaction, in the form of a large exchange current density.
- A large active surface area to enable an increased reaction rate relative to mass or geometric electrode area.
- High electrical conductivity of the electrode. Poorly conductive catalysts must be used in thin layers only or mixed with percolating conductive networks. This is an issue for many oxide catalysts.
- Good wettability, to efficiently get rid of gas bubbles.
- High selectivity of the electrocatalyst towards the relevant reaction. This is generally assumed not an issue in water electrolysis during steady state operation.
- Stability of electrodes, and the materials in all aspects. Mechanical electrode stability towards two-phase flows during gas evolution at high current densities, chemical stability at high temperatures in corrosive alkaline electrolyte, and electrochemical stability under highly reductive and oxidative potentials, and towards depolarization on shutdown or in case of system failures.
- Electrodes should be prepared from abundant and cheap elements, and preferably easy to process.
- Materials and processing should easily comply with health and safety concerns (toxicity, pyrophobicity)

Naturally, trade-off has to be made, e.g. sacrificing mechanical stability to increase porosity, or by increasing catalyst loading to increase activity at the expense of using more material.

The catalytic activity is a very important but weakly specified quantity. In some cases like the oxygen reduction reaction (ORR), a specific figure of merit is widely accepted, namely the kinetic current at 0.9 V vs RHE, but for the oxygen evolution or hydrogen evolution reactions no common figure of merit is widely employed.[57] Several representations exist, but which ones are used depend on the authors and the scope of the publication.

- Graphical reporting (iV-curve) of polarization characteristics. Commonly shown with one or more reference materials or electrodes for comparison. The current axis can vary with orders of magnitude between electrode and catalyst publications depending on the normalization used. The current axis is generally presented with a linear scale for electrodes, and logarithmic scale for catalysts.

- The tafel slope b [mV dec^{-1}], which can be extracted from a polarization data, is used in both electrode and catalysis contexts and represent the needed overpotential to increase current density a decade. It is not a complete characteristic as a stand-alone value.

- The exchange current density i_0 [mA cm^{-2}] is fundamentally interesting, but estimates based on tafel slopes are highly uncertain. Furthermore, the ECSA of electrodes are often difficult to accurately determine and thus the values loose some of their meaning.

- The turn over frequency (TOF) $[s^{-1}]$ of a material describes the number of reactions per catalytically active site. As this involves an estimate of the type and the number of active sites it is associated with a significant uncertainty. The TOF is commonly used in contexts of intrinsic catalystic activity. In electrochemical contexts, the TOF must be accompanied with a specific overpotential.

- Current density i at a given overpotential η, i_η. Normalization is often in terms of apparent geometric electrode area, but can also be with regards to mass loading or electrochemically active surface area.

- The overpotential η at a specified current density i, η_i. In the literature, this is often provided at $i = 10$ mA cm^{-2}, since this is the approximate current density for a 10% efficient photolytic watersplitting device under standard illumination and is thus particularly interesting for photoelectrocatalysis.[58]

This work investigates electrodes and cells, hence the full range polarization characteristics and the overpotentials needed to reach a specific geometric current density are the most interesting figures of merit.

While there are other aspects to a good electrode than high intrinsic catalytic activity, it is still very important. In many cases, the reaction rate is limited by a single reaction step and follows the Sabatier principle: When bonding is too strong, desorption is hindered, and conversely, when bonding is too weak, adsorption is hindered. Hence, a volcano behaviour can be predicted based on specific bonding descriptors. For instance, it has been shown that the HER rate on metallic surfaces depends on the hydrogen adsorbate bonding strength.[59,60] Similarly, the OER on metal-oxides has been shown to correlate with the energy difference between the *O and *OH adsorbates,[61] whereas Suntivich relate the activity of perovskite-oxides with the e_g-orbital electron filling.[62]

Recent reviews by Seh *et al.*[63] and Sapountzi *et al.*[49] provide an up-to-date status on hydrogen and oxygen electrocatalysis.

2.3.1 Hydrogen evolution reaction

The hydrogen evolution reaction in alkaline media is generally accepted to proceed through two steps involving three reactions.[64–67] The first step corresponds to water dissociation, forming adsorbed hydrogen on a surface site, eq. (2.25),

$$\mathrm{M} + \mathrm{H_2O} + \mathrm{e^-} \longrightarrow \mathrm{MH} + \mathrm{OH^-} \qquad \text{(Volmer)} \qquad (2.25)$$

This is followed by either an electrochemical hydrogen desorption step, eq. (2.26), or a chemical desorption step, eq. (2.27), which may proceed concurrently.

$$\mathrm{MH} + \mathrm{H_2O} + \mathrm{e^-} \longrightarrow \mathrm{M} + \mathrm{OH^-} + \mathrm{H_2}\uparrow \qquad \text{(Heyrovsky)} \qquad (2.26)$$

$$\mathrm{MH} + \mathrm{MH} \longrightarrow 2\,\mathrm{M} + \mathrm{H_2}\uparrow \qquad \text{(Tafel)} \qquad (2.27)$$

The polarization kinetics can in some instances provide information on the rate limiting reaction step. If the rate limiting step is either the Volmer, Heyrovsky,

or Tafel step, then the corresponding tafel slopes at standard conditions are $\sim$ 120 mV dec^{-1}, 40 mV dec^{-1} and 30 mV dec^{-1} respectively.[68–70]

It has been shown that the HER rate on metallic surfaces depends on the hydrogen adsorbate bonding strength,[59,60] and it is generally understood that platinum is a near-perfect hydrogen evolution catalyst. However, the activity in alkaline media on platinum is orders of magnitude lower. Whereas the Volmer step in acidic media only involves the reduction of a proton into adsorbed hydrogen, the Volmer step (water reduction) in alkaline media (2.25) is more complex and include water adsorption and hydroxide desorption. Platinum is still very active, although less so than in acidic media. We are however, mostly interested in non-noble metal catalysts since this is one of the advantages of alkaline electrolysis. Hence, platinum serve as an excellent reference material against which to compare catalysts or electrodes, but it is not desirable for large scale use.

Table 2.3 and 2.4 summarize the HER performance of selected publications grouped by respectively near-room temperatures and application-relevant temperatures. Furthermore, in the following sections several categories of alkaline HER catalysts are discussed. Nickel-molybdenum and nickel-tin bimetallics, nickel-sulfides, and Raney nickels are some of the most interesting classes of alkaline HER catalysts. For a presentation on an even wider range of catalysts, the reader is directed to other HER reviews. In specifically alkaline media, Gong *et al.* discuss nickel-based materials,[71] and Safizadeh provide a broad overview.[64] For general hydrogen evolution catalysis Zeng *et al.* discuss recent progress,[69] and McCrory evaluate several materials in a benchmark study.[58]

Briefly, a few comments to the tables are necessary. Loading is omitted since most coatings do not state loadings, and tafel slopes are presented only when stated directly. The overpotential at a given current density n_i is chosen as the primary figure of merit and is shown for various current densities depending on publication. The summarized data is sorted by KOH/NaOH concentration, and then by relative performance. The material stoichiometries stated under *material* are not stoichiometricly exact in many cases, but rather an indication of the elements involved. In cases where the temperature was not stated, room-temperature was assumed. Lastly, materials in the form of NiAlX or NiZn are in essence Raney-type materials.

Expanded table legend for 2.3 and 2.4: [a]: Estimated from graph, [b]: estimated from Hg/HgO reference based on article RHE estimates, (a): Amorphous, TD: Thermal decomposition, ED: Electrodeposition, EDCC: Electrodeposited composite coating, HT: Hydrothermal, MS: Magnetron sputtering, SP: Sintered powder, PP: Pressed powder, VPS: Vacuum plasma spraying, APS: Atmospheric plasma spraying, LPPS: Low pressure plasma spraying, PVD: Physical vapour deposition, DS: Direct sulforization, +S: Sulforization, +P: Phosphorization, +A: Annealing. *For more detailed descriptions see Appendix A.*

Table 2.3: Selected hydrogen evolution activity data published in the 20-35°C temperature range.

Material	Method	Substrate	Electrolyte	Conc.	Temp. °C	i_1 mA/cm^2	η_1 mV	i_2 mA/cm^2	η_2 mV	i_3 mA/cm^2	η_3 mV	b mV/dec	Year (ref.)
NiMo [a]	ED	Cu foam	NaOH	1 M	20	10	10	20	34	100	110		2014[72]
Ni_4Mo	HT+A	Ni foam	KOH	1 M	RT	10	15	200	44			30	2017[73]
Ni_4Mo	HT+A	Ni foam	KOH	1 M	25	10	28	20	37			36	2017[74]
Pt	-	Foil	NaOH	1 M	RT	10	36	50	81	100	92		2017[75]
Pt/C	Ink	Ni foam	KOH	1 M	RT	10	40					43	2015[76]
Pt/C	?	Ti mesh	KOH	1 M	RT	20	46					60	2016[77]
Pt/C	?	Ni foam	KOH	1 M	RT	10	50					37.8	2016[78]
NiS/Ni [a]	DS	Ni foam	KOH	1 M	RT	10	60						2016[79]
NiAlSn [a]	PP	-	NaOH	1 M	30	10	62	100	140	1000	240	107	2001[80]
CoMoB	Ink	GC	NaOH	1 M	RT	10	66	50	145	100	184	67	2017[75]
NiMo	Ink	Ti foil	KOH	2 M	25	20	70						2013[81]
Ni	-	Ni foam	KOH	1 M	RT	10	96					129	2015[76]
Pt [a]	S	Ni foam	NaOH	1 M	RT	10	128						2014[82]
NiS	HT-S	Ni foam	KOH	1 M	RT	10	130					123.3	2016[78]
NiS	DS	Ni foam	KOH	1 M	RT	20	158						2016[83]
CoB	Ink	GC	NaOH	1 M	RT	10	166			100	290		2017[75]
$NiSe_2$	HT	PTFE/C	KOH	1 M	25	10	184	20	201	50	219	77	2015[84]
Mo_2C [a]	PP	-	KOH	1 M	RT	10	192	20	210			54	2012[85]
$NiFe(OH)_2$ [a]	HT	Ni foam	NaOH	1 M	RT	10	214						2014[82]
NiP	HT-P	Ni foam	KOH	1 M	RT	10	230					58.5	2016[78]
$FeNiS_2$	HT-S	Ti mesh	KOH	1 M	RT	20	243					108	2016[77]
$Ni(OH)_2$ [a]	HT	Ni foam	NaOH	1 M	RT	10	249						2014[82]
$NiSe_2$	HT	Ni foam	KOH	1 M	RT	10	255					120	2015[76]
NiS_2	HT-S	Ti mesh	KOH	1 M	RT	20	276					113	2016[77]
Ni [a]	-	Ni foam	KOH	1 M	RT	10	311						2016[78]
Ni [a]	-	Ni foam	NaOH	1 M	RT	10	357						2014[82]
Ti	-	Ti mesh	KOH	1 M	RT	20	>500						2016[77]
NiAlMo	SP	-	KOH	1 M	25			250	57			134	2004[66]
NiAlMo	LPPS	?	KOH	1 M	25			250	67			136	2004[66]
NiAl	PP	-	NaOH	1 M	25			250	156				1993[86]
NiAl PVD 1 [a]	PVD	Ni plate	KOH	1 M	25			100	136	300	202	121	2013[87]
NiAl PVD 2 [a]	PVD	Ni plate	KOH	1 M	25			100	212	300	302		2013[87]
NiAlSn [a]	PP	-	NaOH	10 M	30	10	56	100	120				2001[80]
NiSn	ED	Ni 40-mesh	KOH	30 wt%	RT			200	137	300	161	86	2015[88]
NiCoS (a)	ED	Steel plate	NaOH	28 wt%	35			150	180			94.3	2003[89]
NiMo	ED	Steel	KOH	6 M	30					300	200	110	1990[90,91]
NiS (a)	ED	Steel plate	NaOH	28 wt%	35			150	213			106.8	2003[92]
NiS (a)	ED	Steel plate	KOH	28 wt%	23			135	289			85	1994[93]
NiCo	ED	Steel	KOH	6 M	30					300	380	30	1990[90,91]
NiFe	ED	Steel	KOH	6 M	30					300	410	50	1990[90,91]
NiZn	ED	Steel	KOH	6 M	30					300	425	30	1990[90,91]
NiW	ED	Steel	KOH	6 M	30					300	470	25	1990[90,91]
NiCr	ED	Steel	KOH	6 M	30					300	550	160	1990[90,91]
Mild Steel	-	Steel	KOH	6 M	30					300	620	125	1990[90,91]
NiCu [a]	ED	Steel	KOH	8 M	25	10	213						2015[68]

Table 2.4: Selected hydrogen evolution activity data published in the > 60°C temperature range.

Material	Method	Substrate	Electrolyte	Conc.	Temp. °C	i_1 mA/cm^2	η_1 mV	i_2 mA/cm^2	η_2 mV	i_3 mA/cm^2	η_3 mV	b mV/dec	Year (ref.)
NiAlMo	SP	-	KOH	1 M	70					250	33	80	2004[66]
NiAl	PP	-	NaOH	1 M	70					250	56	62	1993[86]
NiAl	EDCC	Steel plate	NaOH	1 M	70					250	68	67	1990[94]
NiAl	LPPS	Ni p-plate	NaOH	1 M	70					250	105	59	1995[95]
NiAlMo	LPPS	Ni p-plate	NaOH	1 M	70					250	148	71	1995[95]
NiAlMo [a]	VPS	Ni p-plate	KOH	25 wt%	70			100	22	200	34		1992[96]
Pt [b]	MS	SS e-mesh	NaOH	4 M	60			100	40	500	140		2012[97]
NiMo	TD	Ni 80-mesh	KOH	5 N	70			100	41	200	54	45	1982[98]
NiAl [a]	VPS	Ni p-plate	KOH	25 wt%	70			100	45	200	69		1992[96]
NiMo [a]	TD	Ni 80-mesh	KOH	30 wt%	70			100	48	200	60		1982[99]
NiMo [b]	MS	Ni e-mesh	NaOH	4 M	60			100	50	500	190		2012[97,100]
NiAlSn [a]	PP	-	NaOH	10 M	70	10	31	100	65				2001[80]
NiAl [b]	MS	Ni e-mesh	NaOH	4 M	60			100	100	500	270		2012[97]
NiS [b]	ED	Ni e-mesh	NaOH	4 M	60			100	110	500	270		2012[97]
NiSn [a,b]	ED	?	KOH	28 wt%	70	10	170	100	220			52	1992[101]
Ni	-	Ni p-plate	KOH	25 wt%	70			100	300	200	338		1992[96]
Ni	-	Ni 80-mesh	KOH	5 N	70			100	355	200	388		1982[98]
NiS (a)	ED	Steel plate	KOH	28 wt%	80			135	189			47	1994[93]
NiS (a)	ED	Steel plate	NaOH	28 wt%	80			150	90			80.9	2003[92]
NiCoS (a)	ED	Steel plate	NaOH	28 wt%	80			150	70			61.7	2003[89]
NiAl 100 [b]	APS	Ni plate	KOH	30 wt%	80					300	44	56.6	2013[102]
NiAl 300 [b]	APS	Ni plate	KOH	30 wt%	80					300	59	58.6	2013[102]
NiAlMo	LPPS	Ni p-plate	KOH	25 wt%	70					250	74	51	1995[95]
NiAl	EDCC	Steel plate	NaOH	35 wt%	90					200	80		1987[103]
NiSn	ED	?	NaOH	11 M	90					300	100	50	1993[104]
NiAl 30 [b]	APS	Ni plate	KOH	30 wt%	80					300	116	70	2013[102]
NiAl	LPPS	Ni p-plate	KOH	25 wt%	70					250	119	84	1995[95]
NiSn [a]	ED	Ni 40-mesh	NaOH	32 wt%	90					300	140		2014[105]
NiAl	PP	-	NaOH	30 wt%	70					250	165	146	1993[86]
NiMo	ED	Steel	KOH	6 M	80					300	185	112	1990[90,91]
NiZn	ED	Steel	KOH	6 M	80					300	225	50	1990[90,91]
NiCo	ED	Steel	KOH	6 M	80					300	240	35	1990[90,91]
NiFe	ED	Steel	KOH	6 M	80					300	270	25	1990[90,91]
NiW	ED	Steel	KOH	6 M	80					300	280	25	1990[90,91]
NiCr	ED	Steel	KOH	6 M	80					300	445	150	1990[90,91]
Mild Steel	-	Steel	KOH	6 M	80					300	540	135	1990[90,91]
NiMo	Ink	Ni foam	KOH	5 M	70					700	150		2014[106]

Nickel molybdenum

A number of studies have investigated bimetallic nickel materials for their HER activity. Nickel-molybdenum alloys often show the highest activity, whether prepared by thermal decomposition[99,107] or electrodeposition.[90,91] This has lead to a lot of later work on NiMo-type electrodes,[108] and later of the inclusion of molybdenum in raney-nickel electrodes for HER.[66,95,109] As is evident, NiMo is a promising material even when compared against other types of active HER catalysts,[97] and comes out on top in a recent benchmarking study.[58] Hence, various ways to employ the material have been investigated, *e.g.* by synthesizing powders,[81,106] simple electrodeposition,[72,110] hydrothermal deposition and annealing,[73,74] or through magnetron sputtering.[100]

It appears that optimum molybdenum content lie in the range 10-40 mol%, and that molybdenum to some extent will leach out during prolonged electrolysis, although without a loss of polarization performance. Other publications specifically prepare Ni_4Mo. Notable performance demonstrated include 1000 mA cm^{-2} at 84 mV overpotential in 5 N KOH at 70°C for thermal-decomposition-coated mesh electrodes by Brown;[98,99] 20 mA cm^{-2} at 34 mV overpotential in 1 M NaOH at room temperature for electrodeposited foam electrodes by Wang;[72] 10 mA cm^{-2} at 15 mV overpotential in 1 M KOH at room temperature for hydrothermal and annealed electrodes by Zhang;[73] and 20 mA cm^{-2} at 70 mV overpotential in 2 M KOH at 25°C with 1 mg cm^{-2} NiMo nanopowder by McKone.[81]

Nickel tin

Nickel-tin materials are only scarcely investigated in hydrogen evolution context, but additional studies with regards to preparation can be found in the fields of protective coatings, or battery materials. The coatings are commonly prepared by cathodic electrodeposition from pyrophosphate baths, containing nickel and tin chlorides, potassium pyrophosphate $K_4P_2O_7$, and aminoacetic acid NH_2CH_2COOH. The nickel-tin bimetallics show a complex phase diagram,[111] and the activity and resulting morphology depend strongly on bath composition and deposition conditions.

Early work by Santos[101] and Yamashita[104] both show good initial activity, but only Yamashita observe the material to be stable during prolonged hydrogen

evolution. Pure tin shows very poor hydrogen evolution activity, but with the addition of >25 mol% nickel the activity increases dramatically. On the other hand, even a few mol% of tin appear to drastically increase the HER activity of nickel. Later a series of papers by Jović *et al.* investigate the pyrophosphate bath behaviour, and the effects on the coatings and their HER activity.[105,112–114] They find a predominant phase of NiAs-like $Ni_{1+x}Sn$ with $0 < x < 0.5$, similar to Yamashita. This appears to be the same phase that Zhu *et al.* denote Ni_3Sn_2[88] which also show excellent activity and stability. This phase seems to be more active than the alternative Ni_3Sn or Ni_3Sn_4, hence the ideal stoichiometry seems to be in the range of 50-60 mol% nickel.

As with molybdenum, tin has been shown to improve the activity of mechanically alloyed raney nickel.[80]

Nickel sulfide

Some variations of nickel sulfide electrodes show high activity. This has been known at least since Norsk Hydro, now NEL Hydrogen, patented an electrode fabrication method in 1978.[115] Electrodes are often prepared by electrodeposition from nickel-sulfate type baths such as a Watts nickel bath, with e.g. thiourea $CS(NH_2)_2$[92,116,117] or sodium thiocyanate NaSCN[93] as sulfur source. It appears that the amorphous phases are more active than the crystalline phases and that heat treatment of as-prepared electrodes reduce the activity.[89,118] Small amounts of cobalt improve the HER activity further compared to similar samples without cobalt, and some activation takes place upon cathodic current onset, at which the electrode improves over a few hours.[89,118,119] Mostly active amorphous nickel sulfide electrodes contain approximately $\sim$ 15-20 mol% sulfur as-prepared, but the amount tend to decrease over long term polarization without any adverse effects. The improved activity of the amorphous phase over crystalline phase in alkaline media have also been shown for MoS_x and CoS_x.[120]

A novel way of preparing sulfide electrodes was recently demonstrated by Zhu[83] and You.[79] A sample of transition metal oxides or hydroxides is placed downstream of a sulfur deposit in a tube furnace with a argon flow at $\sim$ 400°C. Although crystalline, good activity is still obtained. The technieque may also, see some application for oxygen evolution,[77] and can similarly be used with phosphorous.

Raney nickel

Raney nickel is the common name for a skeletal or spongy nickel material with a very high porosity and large internal surface area. The material is formed by selective leaching of nickel-aluminium or nickel-zinc alloys where the majority of the aluminium or zinc is leached out leaving the nickel with a highly porous structure. The term is at times also used for highly porous materials of other elements, but it is primarily associated with nickel or nickel compounds. As the nickel host structure is left with a very large surface area after leaching, it commonly shows very good catalytic properties but suffer from weaker mechanical properties. It was first prepared by Murray Raney in 1927,[121] with a Ni:Al 50:50 weight ratio that is still commonly used today.

The nickel-aluminium alloy, primarily with the phases $NiAl_3$ and Ni_2Al_3, is prepared by thermal processes: Either aluminium is coated onto nickel followed by an inter-diffusion process, or a melt process can be used directly.[103,122] Electrodes can also be prepared through a powder-route where the alloy is crushed to fine powder and applied through plasma spraying[96,102,109] or together with PTFE binders as done in alkaline fuel cells[123,124] or even in alkaline electrolysis.[125,126] Alternatively, a nickel-zinc alloy is obtained by electrodeposition of zinc onto nickel followed by thermal inter-diffusion, or from direct co-deposition of nickel and zinc.[127,128]

In any case, the nickel-aluminium or nickel-zinc alloy needs to be activated by leaching of the alloying agent in concentrated alkaline solution such as NaOH or KOH. The degree and speed of the leaching process depend on the alloy phase,[87] and concentration (1-10 M) and temperature (20-100°C).[87,94,129–131] The Al-Ni intermetallic leaching reactions primarily proceed through eqs. (2.28) and (2.29)

$$NiAl_3 + 3\,OH^- + 9\,H_2O \longrightarrow 3\,Al(OH)_4{}^- + 4.5\,H_2 + Ni \tag{2.28}$$

$$Ni_2Al_3 + 3\,OH^- + 9\,H_2O \longrightarrow 3\,Al(OH)_4{}^- + 4.5\,H_2 + 2\,Ni\,. \tag{2.29}$$

$Al(OH)_4{}^-$ is poorly soluble in aqueous solutions and can precipitate aluminium hydroxide through (2.30),

$$Al(OH)_4{}^- \longrightarrow Al(OH)_3\downarrow + OH^- \tag{2.30}$$

Hence, a complexing agent such as K-Na-tartrate is often added to prevent precipitation.[87,109]

Activated Raney nickel is pyrophoric. This is due to the large surface area of metallic nickel prone to oxidation combined with adsorbed hydrogen from the leaching process. Severe oxidation will significantly affect the activity, but this can be mitigated by storing electrodes in water. For air storage, a slow drying at room temperature is recommend to limit the rate of the exothermic oxidation. Alternatively, a small positive polarization (< +100 mV) relative to the HER potential can oxidize adsorbed hydrogen without severely oxidizing the nickel surface which take place above +180 mV.[129]

Very high surface areas can be achieved in this way. Roughness factors of between 1000 and 60,000 have been reported.[86,95] It is however, not clear to what extent the surface can be utilized during water electrolysis. Particularly at high current densities, it appears that the pore utilization change.[132] It has also been observed than the activity improved by increasing coating thickness up to 100 µm but no further improvement was seen beyond 150 µm.[102,133]

Lastly, it should be mentioned that in HER contexts, the activity is commonly improved further by adding a molybdenum component.[66,95,109,134] Current commercial suppliers of raney nickel materials also offer a limited range of dopants e.g. Mo, Fe or Cr.[135]

2.3.2 Oxygen evolution reaction

Oxygen evolution is notoriously difficult and has been studied intensely for many years. Work has previously to a large extent focused on metal oxides. Significant interest has been shown in perovskites, including notable work by Suntivich *et al.*[62] and by Bockris and Otagawa.[136,137] Spinel oxides have also received great interest,[138] and also rutiles, rock salts, and other oxides have been examined.[56,57,139] Recently, transition metal hydroxides have seen increasing interest.[140] Not only because some metal hydroxides are more active than the most active metal oxides, but also because some conventional metal oxide surfaces may restructure into hydroxide-phases during the OER as nickel does.

The oxygen evolution reaction pathway is not fully understood and likely depends on which catalyst is used. Several reaction pathways have been proposed in the literature.[57,139] For the alkaline environment the following 5 pathways have been proposed, with S denoting a surface site.

Electrochemical oxide path[141]

$$(a) \quad S + OH^- \longrightarrow SOH + e^- \tag{2.31}$$
$$(b) \quad SOH + OH^- \longrightarrow SO + H_2O + e^- \tag{2.32}$$
$$(c) \quad 2\,SO \longrightarrow 2\,S + O_2 \tag{2.33}$$

Krasil'shchikov path[142]

$$(a) \quad S + OH^- \longrightarrow SOH + e^- \tag{2.34}$$
$$(b) \quad SOH + OH^- \longrightarrow SO^- + H_2O \tag{2.35}$$
$$(c) \quad SO^- \longrightarrow SO + e^- \tag{2.36}$$
$$(d) \quad 2\,SO \longrightarrow 2\,S + O_2 \tag{2.37}$$

Bockris path[137]

$$(a) \quad S + OH^- \longrightarrow SOH + e^- \tag{2.38}$$
$$(b) \quad SOH + OH^- \longrightarrow SH_2O_2 + e^- \tag{2.39}$$
$$(c) \quad SH_2O_2 + OH^- \longrightarrow SO_2H^- + H_2O \tag{2.40}$$
$$(d) \quad SH_2O_2 + SO_2H^- \longrightarrow H_2O + OH^- + O_2 \tag{2.41}$$

Oxide path[141]

$$(a) \quad S + OH^- \longrightarrow SOH + e^- \tag{2.42}$$
$$(b) \quad 2\,SOH \longrightarrow SO + S + H_2O \tag{2.43}$$
$$(c) \quad 2\,SO \longrightarrow 2\,S + O_2 \tag{2.44}$$

Yeager and O'Grady's path[143]

$$(a) \quad S + OH^- \longrightarrow SOH + e^- \tag{2.45}$$
$$(b) \quad S^zOH \longrightarrow S^{z+1}OH + e^- \tag{2.46}$$
$$(c) \quad 2\,S^{z+1}OH + 2\,OH^- \longrightarrow 2\,S + 2\,H_2O + O_2 \tag{2.47}$$

A prevailing mechanistic understanding of oxygen evolution for metal and metal-oxide surfaces (not metal-hydroxides) describes how the binding energy of two reaction intermediates on a single site (SOH and SOOH) follows a scaling relation.[61] The model shows excellent agreement with a wide range of literature values on metal oxides. Interestingly, an unavoidable overpotential is predicted, which may explain why no oxide-catalysts have been found with overpotentials lower than 200 mV at room temperature[III]. Most oxides, including con-

[III] Except perhaps.[144] Not since reproduced.

ventional state-of-the-art IrO_x generally show more than 300 mV overpotential, with variations due to effective surface area and preparation methods.[58,63,145,146] The model is widely used in theoretical approaches and used to plot volcano-type diagrams, and supposedly applies universally for both acidic and alkaline conditions although the reaction steps are based on acidic conditions.[63,147,148]

$$(a) \quad S + H_2O(l) \longrightarrow SOH + H^+ + e^- \tag{2.48}$$

$$(b) \quad SOH \longrightarrow SO + H^+ + e^- \tag{2.49}$$

$$(c) \quad SO + H_2O(l) \longrightarrow SOOH + H^+ + e^- \tag{2.50}$$

$$(d) \quad SOOH \longrightarrow S + O_2(g) + H^+ + e^- \tag{2.51}$$

Table 2.5 and 2.6 present selected OER electrode activity data, split on two tables due to page-size considerations with data grouped by material class. For the hydroxides in 2.6, the materials are not labelled stoichiometrically accurate and the oxide/(oxy)hydroxde form is not specified. Dionigi and Strasser[140] provide a focused overview over NiFe-(oxy)hydroxides and Hamdani *et al.*[138] give an overview over various spinel-type catalysts. Gerken *et al.*[149] published a large-scale screening study on ternary metal-oxides and Zhang *et al.*[150] have screened ternary amorphous compositions. Lastly, McCrory *et al.* published a series of benchmarking studies for the OER.[58,145,146]

Expanded table legend for 2.5 and 2.6: [a]: Estimated from graph, [b]: Estimated from Hg/HgO reference based on article RHE estimates, [c]: Known not to be stable, SD: Supercritical drying, SG: Sol-gel, CP: Chemical precipitation, CCT: Citrate complexion technique, SSR: Solid state reaction, +T: Thermal treatment. *For more detailed descriptions see Appendix A.*

Table 2.5: Selected oxygen evolution activity data published on spinels, perovskites, sulfides, and selenides.

Material	Method	Substrate	Electrolyte	Conc.	Temp. °C	i_1 mA/cm^2	η_1 mV	i_2 mA/cm^2	η_2 mV	i_3 mA/cm^2	η_3 mV	b mV/dec	Year (ref.)
$NiCo_2O_4$	SD	Graphite	KOH	1 M	25			100	184				2011[144]
$NiCo_2O_4$	SG	Graphite	KOH	1 M	25			100	379				2011[144]
La-$CoCo_2O_4$	SG	Ni plate	KOH	1 M	25			100	224				2007[151]
$CoCo_2O_4$	SG	Ni plate	KOH	1 M	25			100	235				2007[151]
$NiFe_2O_4$	CP+T	Ni plate	KOH	1 M	25			100	352	300	716	38	2006[152]
$NiFeCrO_4$	CP+T	Ni plate	KOH	1 M	25			100	283	300	621	40	2006[152]
$NiCo_2O_4$	HT+T	Ni foam	KOH	1 M	RT	10	360						2015[153]
$NiFe_2O_4$ [a,b]	CP+T	Ni plate	KOH	1 M	25	10	390	100				70	2010[154]
$NiFeVO_4$ [a,b]	CP+T	Ni plate	KOH	1 M	25	10	335	100				42	2010[154]
$La_{0.6}Sr_{0.4}CoO_3$	CCT+Ink	RDE	KOH	0.1	RT	10	468						2016[155]
$La_{0.6}Sr_{0.4}Co_{0.6}Fe_{0.4}O_3$	CCT+Ink	RDE	KOH	0.1	RT	10	424						2016[155]
$SrScNbCoO_3$	SSR+Ink	RDE	KOH	0.1	RT	10	350						2015[156]
$Ni_{0.9}Fe_{0.1}S_2$	HT+S	Ti mesh	KOH	1 M	25			100	231			43	2016[77]
$Ni_{0.9}Fe_{0.1}S_2$	HT+S	Ti mesh	KOH	30 wt%	25			100	212			43	2016[77]
$Ni_{0.9}Fe_{0.1}S_2$	HT+S	Ti mesh	KOH	30 wt%	60			100	108			43	2016[77]
$CoNi_2Se_4$	ED	CFP	KOH	1 M	RT	10	160	50	210			72	2017[157]
RuO_2 [c]	ED	?	KOH	1 M	RT	10	360					86	2017[157]
NiSe	HT	Ni foam	KOH	1 M	RT	20	270					64	2015[76]
$Ni_{0.85}Se$	ED	Graphite	NaOH	1 M	RT	10	302	100	364			62	2016[158]
Fe-NiSe	HT+HT	Ni foam	KOH	1 M	RT	50	245	100	264			65	2016[159]
Fe-NiSe	HT+HT	Ni foam	KOH	30 wt%	25			500	246	1000	263	56	2016[159]
Fe-NiSe [c]	HT+HT	Ni foam	KOH	30 wt%	70					1000	210		2016[159]

Table 2.6: Selected oxygen evolution activity data published on (oxy)hydroxide-type and reference catalysts.

Material	Method	Substrate	Electrolyte	Conc.	Temp. °C	i_1 mA/cm^2	η_1 mV	i_2 mA/cm^2	η_2 mV	i_3 mA/cm^2	η_3 mV	b mV/dec	Year (ref.)
NiCo	HT	Ni foam	KOH	0.1 M	RT	10	420					113	2015[160]
NiFe/CNT	HT	CFP	KOH	0.1 M	RT	10	308					35	2013[161]
NiFe/NF	ED	Ni foam	KOH	0.1 M	RT	10	240					33	2015[162]
NiFe/NF [a]	HT	Ni foam	KOH	0.1 M	RT	10	250	30	280			50	2014[163]
$Ni(OH)_2$ [a]	HT	Ni foam	KOH	0.1 M	RT			30	480			65	2014[163]
Ni foam [a]	HT	Ni foam	KOH	0.1 M	RT			30	520				2014[163]
Ir/C [a]	Ink	Ni foam	KOH	0.1 M	RT			30	390			60	2014[163]
FeCoW	SD+ink	Au Foam	KOH	1 M	RT	10	191						2016[164]
FeCo	SD+ink	Au Foam	KOH	1 M	RT	10	215						2016[164]
NiFeMn	CP	CFP	KOH	1 M	RT	20	289					47	2016[165]
NiMn	CP	CFP	KOH	1 M	RT	20	640					70	2016[165]
NiFe	CP	CFP	KOH	1 M	RT	20	401					65	2016[165]
Ir/C	Ink	CFP	KOH	1 M	RT	20	430					78	2016[165]
$NiFe/NiCo_2O_4$	HT+T+ED	Ni foam	KOH	1 M	RT	10	270			1200	340	38.8	2016[166]
NiFe/CNT	HT	CFP	KOH	1 M	RT	10	247					31	2013[161]
NiFe/NF	ED	Ni foam	KOH	1 M	RT	10	215					28	2015[162]
NiFe/NF [a]	HT	Ni foam	KOH	1 M	RT					200	270	43	2014[163]
NiFe	ED	Ni foam	KOH	1 M	RT	10	244					53	2015[167]
Ir/C	Ink	Ni foam	KOH	1 M	RT	10	309					145	2015[167]
NiCe	ED	Ni foil	KOH	1 M	RT	16	277						1989[168]
NiFe	ED	Ni foil	KOH	1 M	RT	16	287						1989[168]
NiLa	ED	Ni foil	KOH	1 M	RT	16	358						1989[168]
NiCo	ED	Ni foil	KOH	1 M	RT	16	397						1989[168]
NiCu	ED	Ni foil	KOH	1 M	RT	16	397						1989[168]
NiAg	ED	Ni foil	KOH	1 M	RT	16	402						1989[168]
NiY	ED	Ni foil	KOH	1 M	RT	16	402						1989[168]
NiMg	ED	Ni foil	KOH	1 M	RT	16	417						1989[168]
NiMn	ED	Ni foil	KOH	1 M	RT	16	417						1989[168]
Ni	ED	Ni foil	KOH	1 M	RT	16	420						1989[168]
NiCr	ED	Ni foil	KOH	1 M	RT	16	427						1989[168]
NiZn	ED	Ni foil	KOH	1 M	RT	16	437						1989[168]
NiCd	ED	Ni foil	KOH	1 M	RT	16	442						1989[168]
NiPb	ED	Ni foil	KOH	1 M	RT	16	443						1989[168]

Metal oxides

Metals will undergo oxidation when exposed to the large anodic potentials during the OER. Hence, metal catalyst for OER are often addressed by their metal-oxides. As a consequence, OER catalysts often suffer from poor electrical conductivity, which may reflect in the activity. Iridium oxide (IrO_x, nominally IrO_2) is generally considered state-of-the-art and this particularly holds true for acid environment such as the one present in PEM electrolysis. Although RuO_2 is more active, it is not stable and is by itself not considered a candidate, hence the acid-stable IrO_2 is employed in PEM electrolysis.[39] Although stable in PEM electrolysis in the conventional potential range, there are some indications that IrO_2 can suffer from dissolution in strong alkaline conditions.[169] In some cases IrO_x is observed not to be stable,[145] and iridium on carbon (Ir/C) catalyst are not stable, although that is expected in part due to carbon corrosion.[170]

Fortunately, the alkaline environment allows for a large range of non-noble metal-oxides to be stable. Perovskites as a class of materials have received much attention. The perovskite is an ABO_3 structure, commonly with rare or alkaline earth cations on the A-site and transition metal cations on the B-site. For instance, $LaNiO_3$ and $SrCoO_3$ appears at the top of the activity volcano based on the binding energy of *OH,[61] and *e.g.* $LaCoO_3$ and $La_{1-x}Sr_xCoO_3$ and a wide variety of other substitutions on A and B sites have been investigated repeatedly.[137,155,156] Notably, $Ba_{0.5}Sr_{0.5}Co_{0.8}Fe_{0.2}O_{3-\delta}$ was predicted to be very active,[62] and although active, the material has been shown not to be stable due to amorphization and disslution of Ba and Sr.[49,171,172] The problem that some A-site cations such as Sr may leach out from perovskites under harsh alkaline conditions has been known for a while.[173,174] Hence, as variations on perovskites, some newer research have started looking into double perovskites.[171] Furthermore, a previous study conducted in-house indicated that among the evaluated perovskite-catalysts the activity appeared to correlate directly with the electronic conductivity. In this context $LaNiO_3$ and $La_{0.6}Sr_{0.4}CoO_3$ showed good conductivity and were found active.

A different commonly investigated class of metal oxides is materials with the AB_2O_4 spinel structure with A^{II} and B^{III} cations. These are primarily prepared with combinations of transition metals, e.g. V, Cr, Mn, Fe, Co, Ni and Cu. Commonly investigated are Co_3O_4-based spinels,[26,109,151,175] and $NiCo_2O_4$,[26,153,176–178] where particularly $NiCo_2O_4$ show very good electronic conductivity. Notably,

Chien *et al.* prepared aerogel $NiCo_2O_4$ with extremely low overpotential of 184 mV at 100 mA/cm^2 at 25°C in 1 M KOH.[144] This together with La-doped Co_3O_4 at 224 mV under identical conditions,[151] are to this author's knowledge the most active electrodes based on spinels published to date. However, most spinels do not compare favourably against the best more recent hydroxide-oxyhydroxide type catalysts,[140] based in part of results presented in a review of Co-based spinels for OER by Hamdani *et al.*[138] That being said, one key advantage of many spinels is the simple preparation that can be used, as the material can be obtained from thermal treatment in air (300-350°C) from e.g. electrodeposited transition metals or chemically precipitated powders, or directly by thermal decomposition. For instance, in a notable paper Xiao *et al.* prepared NiCo-hydroxide and converted it to the spinel structure to act as a conductive supporting layer beneath the more active NiFe-hydroxide catalyst electrodeposited on top. They manage to demonstrate excellent OER performance up to above 1000 mA/cm^2.[166]

Hydroxides, oxyhydroxides and layered double hydroxides

While metal oxides appear as the most frequently investigated OER catalyst, other classes of materials exist that are worth investigating. Notably, metal hydroxides $M(OH)_2$, oxyhydroxides MOOH and layered double hydroxides (LDH) are important, in part because transition metals will tend to form these phases on their surfaces under alkaline oxygen evolution potentials rather than a pure oxide phase.[172,179,180] As the exact phase is often difficult to accurately determine, (oxy)hydroxide is commonly used to label mixed hydroxide and oxyhydroxide phases with indeterminate O_xH_y-stoichiometries. Some metal-hydroxides or oxyhydroxides are labelled as layered double hydroxides (LDH) when anions and water expand the structure by intercalating between layers to compensate charge imbalances. In these types of structures, transition metal atoms are octahedrally coordinated to oxygen forming layers, with oxygen-coordinated hydrogen pointing towards neighbouring sheets. The most general formula of the LDH structure can be expressed

$$[M^{II}{}_{1-x}M^{III}{}_x(OH)_2]^{z+}(A^{n-})_{z/n} \cdot y\,H_2O\,, \tag{2.52}$$

with M^{II} and M^{III} being divalent and trivalent cations, e.g. Ni^{2+}, Co^{2+}, Fe^{2+}, Mg^{2+}, Zn^{2+}, and Fe^{3+}, Cr^{3+}, Al^{3+}, Ga^{3+}.[181] A represents intercalated anions such

as CO_3^{2-}, SO_4^{2-}, Cl^-, ClO_4^-, NO_3^-, CH_3COO^-. Among the anions listed, carbonate shows the highest affinity in NiFe-based materials as well as the smallest layer spacing.[182] Due to their complexity, often hydroxide-type materials are simply denoted MO_xH_y, when the detailed structure is not in focus.

The LDH structure can be understood by looking at nickel and the phase transformations it undergoes at high potentials in alkaline conditions. Hall *et al.* have reviewed the pure nickel hydroxide structures and all the physico-chemical aspects.[183] The behaviour is conveniently illustrated by the Bode diagram in Figure 2.7, where the hydrated phase of nickel oxide exists in 4 phases. In brief, at intermediate potentials, nickel is in the Ni^{II}-oxidation state as either the ordered β-$Ni(OH)_2$ or disordered α-$Ni(OH)_2$. The α-phase have intercalated water and can be OH deficient.[184] Under higher potentials nickel changes oxidation state $Ni^{II} \rightarrow Ni^{III}$, and deprotonizes to form nickel oxyhydroxide β-NiOOH. This is utilized in some batteries. Upon higher oxidation (over-charging), a fraction of the nickel increases in oxidation state, and to compensate for that, anions such as OH^- and water intercalates into the layers. This causes a significant lattice expansion between layers from $\sim$ 4.8 Å to 7 Å. The difference in lattice spacing from α to γ is almost a doubling from $\sim$ 4.6 Å to 8 Å. The α-phase is disordered, and the α and γ-phases are LDH materials.

As these materials are layered they are highly anisotropic, and small particles often show plate or flake morphologies. Hence, coatings grown directly as hydroxide-type phases experience a significant surface roughening with vertical platelet morphologies.

When incorporating foreign cations into the nickel hydroxide prototype structures, the oxidation state of the foreign cations will affect how and what hydroxide structure forms. Hence, if M^{III} cations such as Fe^{3+} is incorporated through co-precipitation, the structure must either expand and allow for anion-charge compensation, form oxyhydroxide structures, or a structural compromise somewhere in-between. Since many preparation methods introduce nitrate or carbonate ions a LDH structure is often the result. Interestingly, some variations of LDH show significant OH^--conductivity.[185,186]

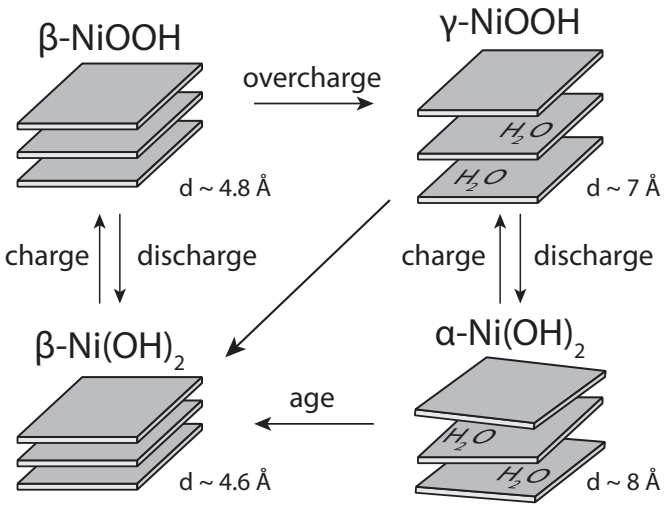

Fig. 2.7: Bode diagram illustrating different nickel-(oxy)hydroxide phases. The charge-discharge transformations are electrochemically induced, but ageing happens chemically.

Nickel-iron hydroxides

Of particular interest is the nickel-iron (oxy)hydroxide system. Over the previous 6 years it has taken the throne as the state-of-the-art catalyst for alkaline oxygen evolution and spawned two review articles only addressing this specific material.[140,187] Pointers towards the high activity has been published almost 30 years ago by Corrigan,[168,188,189] but back then the interest was largely in the context of nickel-hydroxide batteries where the improved OER was a parasitic reaction relative to the oxidation of nickel from Ni^{2+} to Ni^{3+}. Interest has been renewed in recent years after papers by Merrill and Dougherty in 2008,[190] Li, Walsh and Pletcher in 2011[191] and Gong *et al.* in 2013.[161]

Nickel-iron-(oxy)hydroxides show the highest activity with a 10-50% iron-in-nickel doping level.[140] It is speculated that iron is the active site, and that the binding energies are optimized by squeezing into the nickel host structure.[147,148] Indications are that maximizing iron content, balanced against preventing iron-hydroxide phase separation dictate the optimum activity. The mixed material further shows higher conductivity than either pure (oxy)hydroxides, and particularly pure FeOOH, which is poorly conducting and show negligible OER activity. Furthermore, it dissolves quickly and cannot be utilized directly.[192] It is worth noting that many of the hydroxides behave as semi-conductors, and only reach reasonable electronic conductivities at certain applied positive po-

tentials.[180,193,194] For $NiFeO_xH_y$ this seems to be close to +250 mV relative to the OER standard potential.

Several approaches to synthese metal-hydroxides have been described in the literature. In many instances, the method rely on the low solubility of the metal-hydroxide which form at high pH, hence by forming the metal-hydroxide near a surface, particles or coatings can grow. Some examples include cathodic electrodeposition by reduction of nitrate,[162,167,195] anodic electrodeposition,[196] chemical precipitation,[178] and homogeneous hydrothermal precipitation.[160,163,184,197] Additionally, the LDH materials can be exfoliated, as has also been demonstrated for a NiFe composition.[198] Hydroxide layers can also be grown on metallic or metal-oxide electrodes by electrochemical cycling, which notably have been demonstrated to significantly improve nickel electrodes. This was however shown to likely be caused by the uptake of impurity iron in the electrolyte, which in very small amounts drastically improve activity. It was shown that pure nickel is a very poor catalyst, and speculated that a significant amount of literature with active nickel is due to iron impurities frequently present in as-prepared electrolyte.[193,199,200]

Notable performance by $Ni_{1-x}Fe_x(OH)_2$ has been achieved with electrodeposition reaching 10, 500 and 1000 mA/cm^2 at 215, 240 and 270 mV;[162] by hydrothermal deposition reaching 30 mA/cm^2 at 280 mV;[163] and by ternary NiFeMn reaching 20 mA/cm^2 at 289 mV overpotential.[165] Doping with vanadium has also shown further improvements.[201] A very thorough overview over published NiFe oxygen evolution performance is available in the 2016 review by Dionigi and Strasser.[140]

Non-oxides

Non-oxide materials may also play a role, although stability is likely an issue for these materials. Phosphides, sulfides, and selenides can all be envisioned as oxygen evolution catalysts. Among these, sulfides[77–79,83] and phosphides[78,202] have demonstrated good activity, and selenides have demonstrated good to excellent activity.[76,157–159] It has however, been proposed that these materials, including the highly active NiFe-selenide, transform *in-situ* to oxide and (oxy)hydroxide phases.[203] Nonetheless, excellent activity has been demonstrated after transformation of 10 mA/cm^2 at 195 mV. Probably the best OER activity (at least initially) published to date is on a $CoNi_2Se_4$ selenide reaching 10 mA/cm^2 at 160

mV.[157]

2.4 Ionic conductors

The electrolyte is just as important as the electrodes, and is often the component after which the electrolysis cell is categorized by, since it determine the electrode reactions. Like good electrodes, which are crucial for obtaining high efficiency, so are a good ionic conductivity necessary particularly at large current densities. In addition to providing ionic conductivity, the electrolyte serve the important purpose of separating gasses. Not only is safety a serious concern, but overall efficiency also suffer from excessive gas crossover since gas, mostly hydrogen, appearing at the opposite electrode side is effectively lost. This section seeks to briefly describe relevant concepts closely linked to the use of alkaline electrolytes, including KOH (aq) and polymeric membranes relevant in the scope of alkaline electrolysis.

2.4.1 Potassium hydroxide

Aqueous potassium hydroxide is the go-to liquid electrolyte in alkaline systems. It is commonly used over sodium hydroxide due to its' higher peak ionic conductivity.[204,205] KOH or another liquid OH^--conducting electrolyte is necessary for both classic alkaline electrolysis as well as APEM systems, although true AEM may not need a liquid electrolyte beyond water.

In most recent electrode and catalyst studies, either 0.1 M or 1 M solutions are used at room temperature and specified by molarity. In older papers, electrodes were more often evaluated at industrial conditions around 4-6 M and temperatures close to 80°C. Since this project run a lot of single cell tests at 80°C we choose to specify the KOH concentration by weight% in most instances, since it is temperature independent. As the density of KOH (aq) vary with temperature, a 1 M solution at room temperature is not exactly 1 M at 80°C, hence a description by molarity can be inaccurate when working at elevated temperatures.

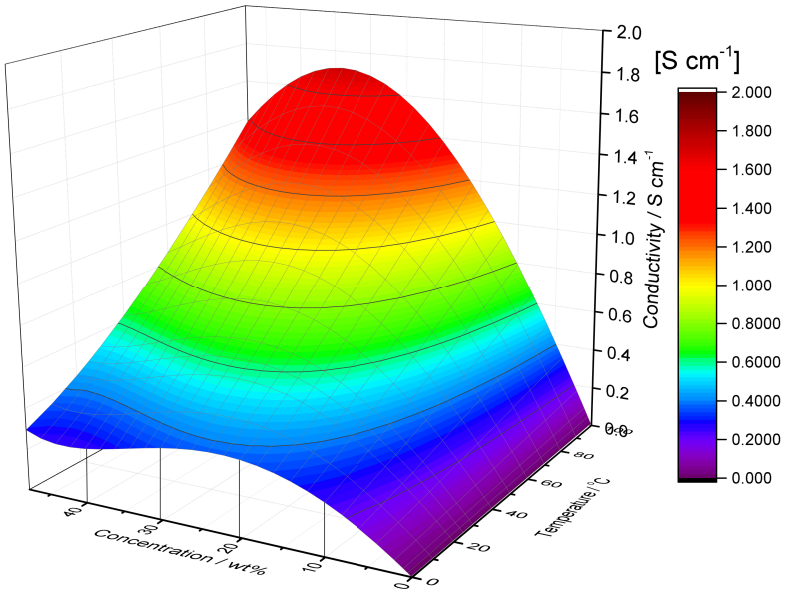

Fig. 2.8: Specific condutvitiy of aqueous potassium hydroxide over a wide temperature and concentration range. Data adopted from [204].

Ionic conductivity

Several studies have investigated the conductivity of KOH (aq),[33,206,207] but the conductivity is most easily accessible in the review study, and empirical model presented by Gilliam *et al.*[204] The data from the model is summarized in Figure 2.8. Notably, at 80°C the conductivity peaks at around ∼33 wt% at almost 1400 mS cm^{-1}, whereas the peak at lower temperatures shifts towards slightly lower concentrations. At 25°C conductivity tops out at ∼27 wt% with 620 mS cm^{-1}.

Ionic transport in liquid electrolytes and polymeric membranes are generally achieved by two mechanisms. The vehicle mechanism, where an ion will attach to another molecule, e.g. H^+ onto H_2O forming H_3O^+, which then migrate along movement of the water molecule in acid. Migration due to an electric field then result in parasitic transport of water known as electro-osmotic drag. Alternatively, the structural diffusion method also known as the Grotthuss mechanisms. With the Grotthuss mechanism, sometimes referred to as proton hopping, a proton will transfer from one water molecule to another, and migrate by jumping between molecules. OH^- conductivity behaves similarly, but not exactly analogously to H^+ diffusion in aqueous electrolytes. The solvation degree associated

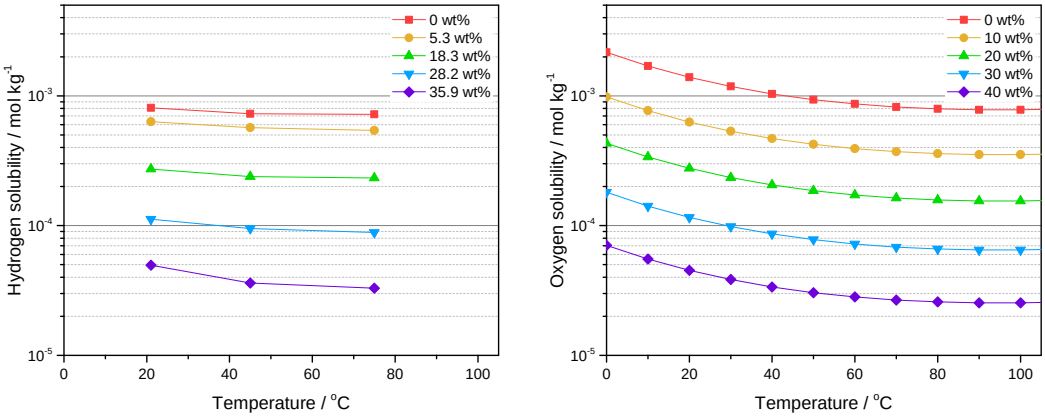

(a) **(b)**

Fig. 2.9: Gas solubility in KOH (aq) in mol kg^{-1} as a function of temperature and concentration. **(a)** Hydrogen solubility adopted from [210, 211] and, **(b)** oxygen solubility under 1 bar oxygen partial pressure, adopted from [212].

with the Grotthuss mechanism turns out to be larger for hydroxide.[208,209] Notably, a significant amount of water needs to be present around the OH^--ion itself to achieve ideal conditions for ionic transport, hence why the conductivity decreases above a certain threshold concentration, which at 30 wt% KOH correspond to roughly 7 H_2O molecules per KOH.

Gas solubility

The solubility of hydrogen and oxygen are important parameters in aspects of gas-crossover properties. Values obtained from literature are presented in Figure 2.9. What is interesting here is the approximately one order of magnitude lower solubility between pure water and 30 wt%. Hence in terms of dissolved gasses, KOH (aq) have superior properties over pure water. It is further seen that gas solubility decreases with increasing temperature, about two-fold going from 25°C to 80°C. The trend reverses however, when going significantly above 100°C.[210] Lastly, the magnitude of H_2 and O_2 solubility is about the same under equivalent conditions.

Diffusion and gas crossover effects

The second most important property of a membrane or porous diaphragm is to separate gasses. Hence, it is worth discussing different effects that play into

crossover. Any reasonable membrane and diaphragm will provide separation between gas bubbles, but crossover will in practice take place through diffusion of dissolved gas. This proceeds in principle through three mechanisms:

- Diffusion of dissolved species as described by Fick's Laws
- Movement of dissolved species through cross-permeation of the electrolyte described by Darcy's law
- Ion migration induced movement of electrolyte and attached solvated gas

In practice, at least for PEM electrolysis using Nafion, the third option is negligible.[41] This leaves the Fick's diffusion induced flux Φ^{fick} and Darcy's flow induced flux Φ^{darcy}. For simplicity and because the crossover of hydrogen is larger than oxygen, only hydrogen is addressed in the following.

Fick's diffusion is driven by concentration gradients, hence it is proportional to the difference in concentration of dissolved gas Δc, the diffusion constant of the given specie in the solute D, and the diffusion distance d.

$$\Phi^{fick} = -D\frac{\Delta c_{H_2}}{d}\,. \tag{2.53}$$

At equilibrium, the concentration follow Henry's law with respect to partial pressure and solubility S. Hence,

$$c = p_{H_2} \cdot S \tag{2.54}$$

and since the partial pressure of hydrogen is effectively the absolute pressure on the cathode side, the permeability ε^{fick} can be written

$$\varepsilon^{fick} = D \cdot S\,. \tag{2.55}$$

Hence, the Fick's induced crossover can be written

$$\Phi^{fick} = -\varepsilon^{fick}\frac{\Delta p_{H_2}}{d}\,. \tag{2.56}$$

Darcy's law describes the volumetric flux ϕ of a fluid through a porous medium over a distance d due to an absolute pressure difference Δp, and is given by

$$\phi = -\frac{K}{\mu}\frac{\Delta p}{d}\,, \tag{2.57}$$

Table 2.7: Hydrogen permeability values, obtained from [41].

Parameter		PEM Nafion/H_2O	Alkaline Zirfon/KOH
ε^{fick}	[mol cm^{-1} s^{-1} bar^{-1}]	$5.32 \cdot 10^{-11}$	$1.4 \cdot 10^{-12}$
ε^{darcy}	[mol cm^{-1} s^{-1} bar^{-1}]	0	$1.4 \cdot 10^{-10} \cdot p_{H_2}$

with K being the intrinsic permeability of the medium and μ the viscosity of the liquid. The gas permeation through this process is found by taking the concentration into account.

$$\Phi^{darcy} = \phi \cdot c = -\frac{K}{\mu} S p_{H_2} \frac{\Delta p}{d}, \tag{2.58}$$

By which we can take the Darcy's permeability ε^{darcy}

$$\varepsilon^{darcy} = \frac{K}{\mu} S p_{H_2} \tag{2.59}$$

This leaves us with crossover fluxes proportional to a permeation factor, and the difference in partial pressure (Ficks) and absolute pressure (Darcy). To discuss the consequences, we need estimated values for the permeabilities. Studies by Schalenbach *et al.*[41,47,213] based on theoretical and experimental work have found the values presented in Table 2.7. Notably, the by far largest contribution come from darcy's flux in the case of porous separators in alkaline electrolysis, effectively prohibiting differential pressure. However, at balanced pressures where $\Delta p \approx 0$ the Darcy's flux is essentially nil. This leaves us with the Fick's diffusion flux which shows a 38-fold difference in favour of the alkaline system. Consequently, while PEM systems can work with differential pressure, the general pressurization of the cathode side result in a very significant crossover flux. Not only does this require recombination catalysts (Pt on the anode) or a very limited operation range,[39] it also result in significant efficiency losses. In this aspect, ion-solvating membranes with KOH have the prospect of combining the best of each concept, i.e. the significantly lower gas solubility of KOH along with the non-porous nature of the membranes.

Safety and explosion limit

Gas crossover results in a loss of efficiency, but it is also associated with a safety hazard due the explosive nature of H_2-O_2 gas mixtures. Hence, keeping the

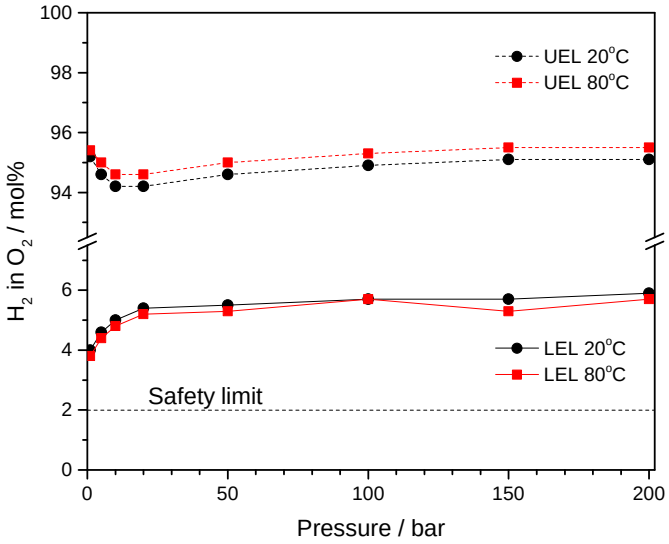

Fig. 2.10: Upper explosion limit (UEL) and lower explosion limit (LEL) for H_2 in O_2. Data adopted from [214].

gas mixing values below the safety limits is important. The lower explosion limit (LEL) and upper explosion limit (UEL) of hydrogen-in-oxygen mixtures are summarized in Figure 2.10 based on data from Schröder *et al.*[214] The explosive window increase slightly with temperature, but initially decrease with pressure. Under ambient conditions is the LEL around 4 mol% H_2 in O_2. The UEL in oxygen, most relevant for electrolysis cells, is about 95.5 mol%, and about 76 mol% in air. The LEL is largely the same in air. The safety limit is normally taken as 50% of the LEL, hence commonly put to 2 mol% of H_2 in O_2.

2.4.2 Alkaline membranes

We reckon that two approaches exist towards alkaline membranes. The defining and necessary OH^--conductivity can be achieved either through functionalization of stable polymers with cationic groups or through dissolving OH^--conductive alkaline electrolyte inside the membrane by engineering good membrane hydrophilicity. Both systems result in homogeneous membranes. The first is a true anion-exchange membrane approach and can ideally operate with pure water, whereas the latter is an ion-solvating type, which requires the presence or uptake of a liquid alkaline electrolyte. Engineering porosities into membranes may represent an attractive modification or a third approach, but hydroxide conductivity based on porosity or a separated two-phase system is likely not feasible

beyond what other mixed organic-inorganic separators may achieve. This categorization of membranes is also described in literature.[215,216]

Anion exchange membranes

The primary approach in the literature for preparing anion-exchange membranes in their hydroxide form is by functionalization of stable polymers. Generally, a cationic group is bound covalently to a polymer backbone, either through side chains or directly as a part of the backbone. The cationic groups are often quaternary ammonium (QA) based, but can also be based on imidazolium, phosphonium, or sulfonium, and others.[217] A common approach uses quaternary ammonium groups, which are grafted onto e.g. polysulfone[218] ($\sigma \sim 15$ mS cm^{-1} at RT) or poly-vinyl-benzyl-chloride[219,220] ($\sigma \sim 15$ mS cm^{-1} at RT). QA groups are often used as they generally show higher stability than their alternatives,[221] although severe stability concerns remain an issue. One challenge with the AEMs in their hydroxide form is their tendency to convert to the less conductive carbonate form on contact with CO_2 from air.[222] Secondly, the OH^- ions tend to attack the QA group, hence slowly eliminating the cationic groups.[221] This is particularly challenging for the ionomers in the catalyst layers. To date, the most stable anion exchange membrane is based on alkylpolybenzimidazolium hydroxides[223] ($\sigma \sim 10$ mS cm^{-1} at 30°C), but as is the case with several membranes, it display insufficient conductivity for practical applications.

For a more complete overview refer to review articles by Varcoe *et al.* (2014)[217] and Merle *et al.* (2011).[215]

Ion-solvating membranes

Ion-solvating membranes are membranes capable of dissolving liquid alkaline electrolyte to form a semi-solid. Hence a seemingly homogeneous mixed phase of polymer and alkaline salt solution can be formed, which to some extent retain the ionic conductivity properties of the salt solution and the mechanical properties of the polymeric membrane. A notable case with polybenzimidazole (PBI) and KOH for fuel cell application was first described by Xing and Savadogo in 2000[224] ($\sigma \sim 40$ mS cm^{-1} at RT). Alternative systems are largely based on polyvinyl-alchohol (PVA) and polyethylene-oxide (PEO).[215]

Polybenzimidazole

The case of PBI deserve some elaboration, since it is the foundation for a large part of this work. Specifically, membranes based on poly(2,2'-(*m*-phenylene)-5,5'-bibenzimidazole) (*m*-PBI), which is commercially available. *m*-PBI is mostly known for it's good thermochemical stability and it's application as electrolyte in high temperature PEM (HT-PEM) fuel cells. In HT-PEM systems, the ionic conductivity is supported by phosphoric acid (PA) within the membrane.[225] This electrolyte system can be seen as PA-doping of the membrane, or alternatively, as PA dissolved in the membrane. Nonetheless, independently on terminology, a homogeneous single-phase solid membrane can be realised. In practice this is done by equilibrating the membranes at room temperature. For HT-PEM fuel cell applications, this works very well at common operating temperatures around 160°C, but it has been shown in-house not to work in steam electrolysis mode due to rapid degradation of the membrane.[226]

An alternative to acid doping of PBI membranes, can be achieved with alkaline solution. Using KOH (aq) a similar system can be formed in alkaline conditions. This was first demonstrated in 2000 by Xing and Savadogo[224] for alkaline fuel cells, and later demonstrated for water electrolysis in 2013 by Aili *et al.*[227] As the initial investigations showed promising results, a large part of this project have focused on further testing of polybenzimidazole-based membranes.

The basis for Chapter 4 is KOH doped *m*-PBI or modifications thereof. The membranes are prior to cell test equilibrated in aqueous KOH of the desired concentrations. In practice this means leaving the membranes in the solution at room temperature overnight or longer. Equilibrating the *m*-PBI means that the equilibrium shown in Figure 2.11 shifts to the right to an extent depending on the concentration of the bulk solution.

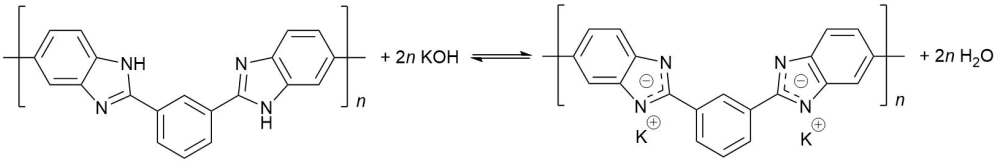

Fig. 2.11: Equilibrium scheme between the neutral pristine *m*-PBI polymer and the potassium polybenzimidazolide.

Previous work in our group has assessed the chemical stability[228] and several mechanical and chemical characteristics[229] of KOH doped *m*-PBI. However, the

practical performance in an electrolysis cell was previously not investigated beyond a single polarization test in a non-zero-gap cell.[227] Hence, some research is left to be done.

2.5 Alkaline water electrolysis with membranes

Having touched upon electrodes and electrolyte it seems worthwhile to spend a page on full single cell electrolysis performance. Here, what is interesting is the performance achieved in alkaline electrolysis using membranes. It makes sense to distinguish between AEM cells without KOH/NaOH, and APEM cells with KOH/NaOH of varying concentrations. Furthermore, it is relevant to distinguish between cells using platinum group metal catalysts and those without. Figure 2.12 present a comprehensive literature sampling on single cell polarization performance. The data points are extracted from presented polarization curves across 16 publications. The figure does distinguish between different parameters such as temperature, and does not provide details on e.g. stability, membrane thickness, or other relevant properties.

What is mainly interesting is the difference in performance achieved between AEM and APEM cells. A clear difference both in terms of activation and in regards to the ohmic behaviour is evident. Furthermore, PGM catalysts (primarily Pt and Ir) still reign supreme in terms of performance, but improved performance using non-noble metal catalysts should be achievable. It should be mentioned that the best APEM performance with and without PGM catalysts are published in the same publication.[238] Lastly, we note that it is a young research field, with the first publications arriving around 2011.

Data on which the graph is based on are, for AEM: [175, 219, 220, 230–234] and for APEM: [175, 191, 233, 235–239].

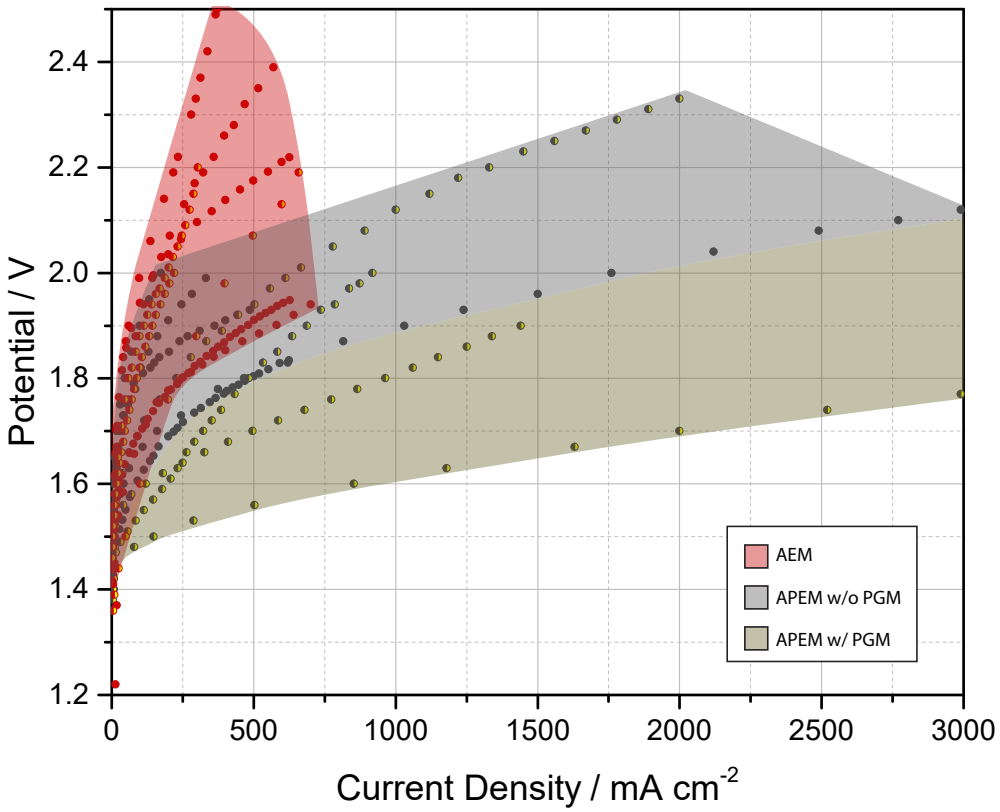

Fig. 2.12: Alkaline membrane electrolysis data presented in the literature. Data has been extracted from curves and are plotted in groups of AEM (red) or APEM (grey), and with PGM catalysts (yellow shading) or without (solid red/grey). Varying temperatures and stabilities have been disregarded, and only polarization performance is considered. AEM data: [175, 219, 220, 230–234], APEM data: [175, 191, 233, 235–239]

3

Experimental alkaline electrolysis

3.1 Alkaline electrolysis

A major part of the project involved the practical aspects of constructing, developing, and maintaining a setup for testing alkaline electrolysis single cells. As it turns out, actively circulating concentrated KOH (aq) at high temperatures is not necessarily without problems. The highly corrosive environment combined with the presence of H_2 or O_2 put some serious limitations on materials. For instance, stainless steel is not completely corrosion resistant towards concentrated KOH at 80°C.

Note that the cathode is mentioned prior to the anode when describing full single cells throughout the entirety of thesis.

Cell operation

Running an alkaline electrolyzer cell is associated with a set of necessary physical quantities that must be controlled or measured, as-well as a set of nice-to-have quantities that may or may not be important depending on what is investigated. Necessary quantities include the electrochemical behaviour of the cell as probed by e.g. a potentiostat or other electrical devices, good control of temperature, and control of the electrolyte with regards to concentration and flow.

Nice-to-have quantities include volume of produced gasses (gas flows), H_2 in O_2 values and vice versa for crossover behaviour, as well as long term water management to maintain electrolyte concentration.

An important conceptual design parameter is how the electrolyte is managed with regards to separation of cathode and anode side. Haug *et al.*[240] discuss three modes: Separated, partly separated, and mixed electrolyte flows. In separated mode, the anolyte and catholyte do not mix beyond what may occur across the diaphragm or membrane. In partly separated mode, the electrolyte storage tanks are connected through a small tube or similar, but not actively mixed and otherwise identical to fully separated. The connection allows for slow concentration equilibration and electrolyte level (volume) equilibration. This mitigates electrolyte build-up on one side due to migration across the membrane and subsequent drying which can occur in fully separated mode with membranes. Lastly, in the mixed mode the electrolyte is actively mixed after degassing, e.g. through a shared storage tank. Mixed mode results in significantly higher H_2 in O_2 values, and will mix dissolved ionic species that may leach out of the electrodes, however electrolyte equilibration is otherwise a non-issue. Ideally, a setup can switch between modes through the switching of a few valves.

Materials

To prevent ionic contamination of the electrolyte, e.g. iron from steels tubes, resistant polymeric materials are generally preferred. If metals are necessary, nickel or nickel-based alloys are preferred. For instance, Nickel 200, Monel 400 ($\sim$63% Ni, $\sim$28-34% Cu, < 2.5% Fe, < 2% Mn) and some variations of Inconel 600/625/690 ($\sim$60-70% Ni, $\sim$15-30% Cr, $\sim$10% Fe, plus other trace metals) generally show good corrosion resistance towards hot KOH, with some variations across sources in part due to varying conditions.[241–245] Normal 316 stainless steel is not recommended for operation at temperatures around 80°C as it will bleed iron into the electrolyte.

At up to 80°C several resistant polymeric materials also exist. Poly-(tetrafluoroethylene) (PTFE e.g. Teflon®) and perfluoroalkoxy-alkanes (PFA) show excellent resistance even at higher temperatures, and are both recommended materials. However, cheaper materials such as polypropylene (PP), polysulfone (PSU), poly-(phenylenesulfide) (PPS), and ethylene-propylene-diene-monomer rubber (EPDM) also show good resistance and can be used for e.g. valves, fittings, tubes

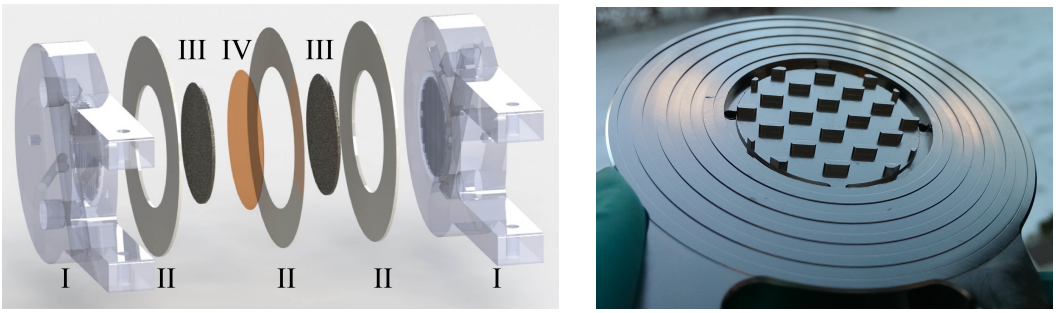

(a) **(b)**

Fig. 3.1: The DTU cell; circular geometry with a total cell diameter of 70 mm, and electrode active area diameter of 38.5 mm. **(a)** Exploded cell view. The assembly is kept together with a set of end-plates (not shown). (I) flowfield-plates, (II) gaskets, (III) electrodes, (IV) membrane. **(b)** photo of a pristinely coated cell flowplate with the most recent flow pattern.

or gaskets, although their temperature ratings generally are lower.[246–249]

3.1.1 DTU cell

Cell testing was carried out at two locations. Primarily at DTU as the primary institutions, but also at Forschungszentrum Jülich (FZJ) as part of a 3 month visiting research stay. Although similar, the cell and test-setups differ slightly, hence a section is dedicated to each setup.

The DTU cell is a 11.6 cm^2 cell and is illustrated in Figure 3.1. The exploded view in Figure 3.1a shows flow plates, gaskets, membrane, and electrodes, but does not show the end-plates. Fuel cell-type membrane-electrode-assemblies (MEAs) were not prepared in the sense that electrodes stick to the membrane, but the cathode-membrane-anode assembly may be referred to as an MEA. The end-plates keep the cell components together with eight M8 bolts, and heating elements and electrical wiring is connected directly to the flow field. The eletrolyte is introduced directly to the flowfield-plate through fittings in the back of the plate. The end-plate have holes in them to leave room for the fittings in the flowfield-plate. The photo (3.1b) shows a pristinely coated cell. Technical drawings of the cell house and end-plates are available in Appendix B.

The cell house and end-plates were milled in 316 steel. The cell house was coated with 20 µm electroless nickel containing ∼10 wt% of phosphorous (by

Elplatek A/S). End-plates were not coated since they are not in contact with the electrolyte. Electrodeposited nickel is not recommended due to the geometry of the cell house, and initial cells with electrocoatings showed partial coating delamination.

The active area of the cell is defined as 11.6 cm^{-2}, since circular electrodes with a diameter of 38.5 mm were used. Membrane and diaphragm pieces were prepared with a 44.5 mm diameter unless otherwise specified. Two flow field patterns were employed, as illustrated in Figure 3.2. The initial straight channel pattern (linear) was adopted from a previous electrolysis cell design, but a more open-back design was desired to help facilitate gas removal, hence the pin-type pattern (pin) was adopted after a while. Furthermore, a pattern was added to the gasket area to improve leak-tightness. The effects of modifying the flow field were not quantified.

A typical cell employ pressed nickel foam electrodes and PTFE and/or EPDM gaskets. Gasket thickness depends on the MEA of the cell and were initially chosen slightly thicker due to the softness of EPDM gaskets. At later stages with thinner MEAs, the gaskets were dimensioned to be slightly thinner than the MEA.

Cells were assembled horizontally by careful alignment of components and mounted in the setup illustrated in Figure 3.3, schematically on in 3.3a and with a photo in 3.3b. Most measurements with the DTU cell included in the thesis were done under separated electrolyte conditions as shown in the figure. The electrolyte was stored in PTFE bottles acting as degassing tanks, and gear pumps circulated the electrolyte through PFA tubes and PFA or PTFE fittings. An Elektro-Automatik EA-PS 3016-20 B power supply unit managed the current-voltage control. The electrical connections and the pumps were controlled by a LabVIEW interface. No analysis were performed on the produced gasses, which were simply vented.

3.1.2 FZJ cell

The FZJ cell was a 5×5 cm^2 cell and is shown in Figure 3.4. The flowfield-plates contain heating elements and were milled in nickel. A set of gold coated copper current collectors were used, which were insulated from the end-plates with a PTFE-material. The steel end-plates were fixed with 6 M8 bolts, and the

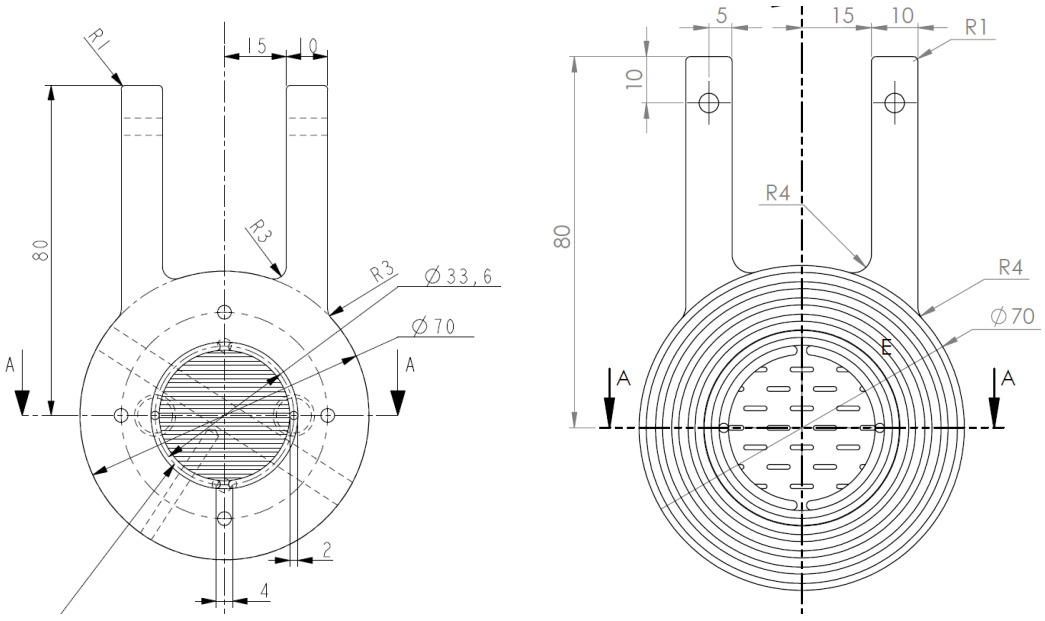

(a) **(b)**

Fig. 3.2: The two flow fields used, **(a)** a straight-channel flow field (linear), with land width of 1.1 mm and channel width of 1 mm and, **(b)** a pin-type flow field (pin) with land width 1.1 mm and spacing of 3.1 mm.

electrical current wiring were connected to the current collectors, whereas the voltage probes were connected directly to the flowfield-plate. The electrolyte was introduced from the edge into the flowfield-plates. The gold-coated plates were observed to corrode and exposed copper and corrosion products.

For tests with the FZJ cell, electrodes were in the form of nickel foam (f) or perforated plates (pp). The labels **(f)** and **(pp)** will be used to denote the support when different electrodes or coatings are applied, e.g. will R-NiMo(pp) represent a Raney-nickel-molybdenum coating on a perforated plate support.

Cells were similarly assembled horizontally, but the alignment of flowfield, current collector, and end-plates were assisted by two PTFE pins. The cells was connected to the test station schematically shown in Figure 3.5. The setup used a partially separated system with a tube connecting the bottom of the two electrolyte vessels. PTFE was used for tubes and valves, whereas some fittings were made from PP. For long term experiments, the exhaust gas from the anode (O_2 with trace H_2) was lead through a bubble flask prior to two drying steps with silica gel and molecular sieves, after which it was fed to the H_2 in O_2 sensor.

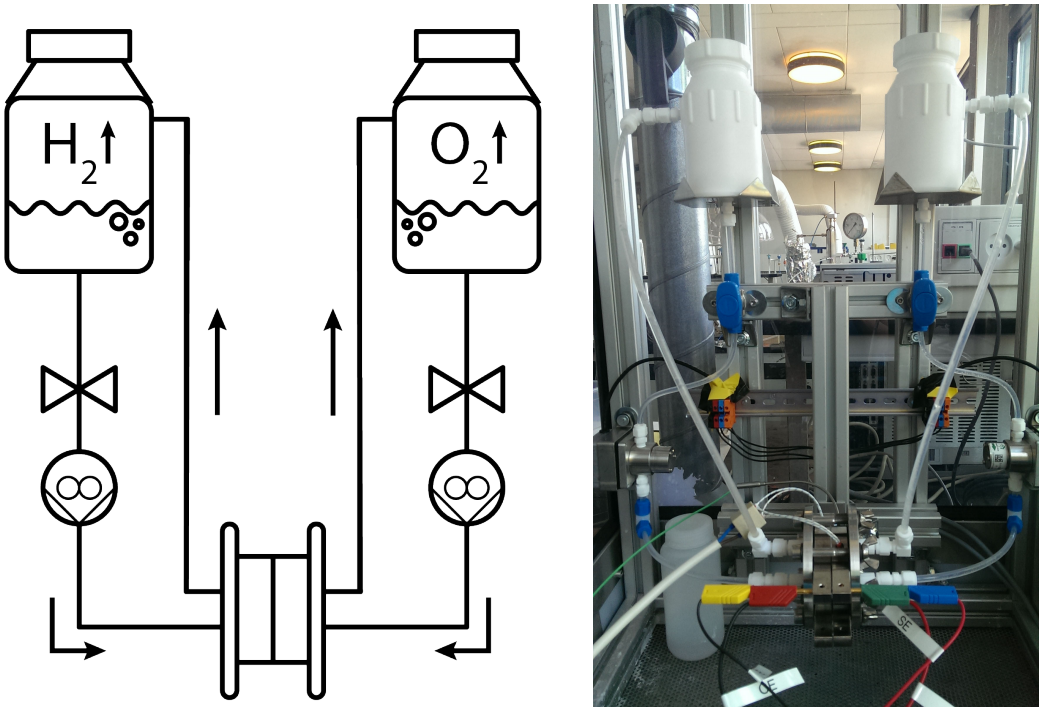

(a) (b)

Fig. 3.3: The test station for the DTU cell. **(a)** Schematic of the electrolyte flow. Heating and current was applied directly on the cell. **(b)** Image of the actual setup with a mounted cell. The lids of the PTFE containers were not tightened to let the gas escape.

Polarization measurements and break-in were in most cases controlled by a BioLogic HCP 1005 potentiostat with a 100 A booster. Long term experiments were current controlled with a different PSU, which was temporarily swapped when polarization measurements were recorded.

3.1.3 Membranes and separators

For tests in the DTU cell, membranes and separators were die cut. Doped membranes were placed between PTFE sheets before cutting. The separators were cut to a circular areas of 44.5 mm diameter. At FZJ the separators were manually cut to squares with about 7×7 cm^2.

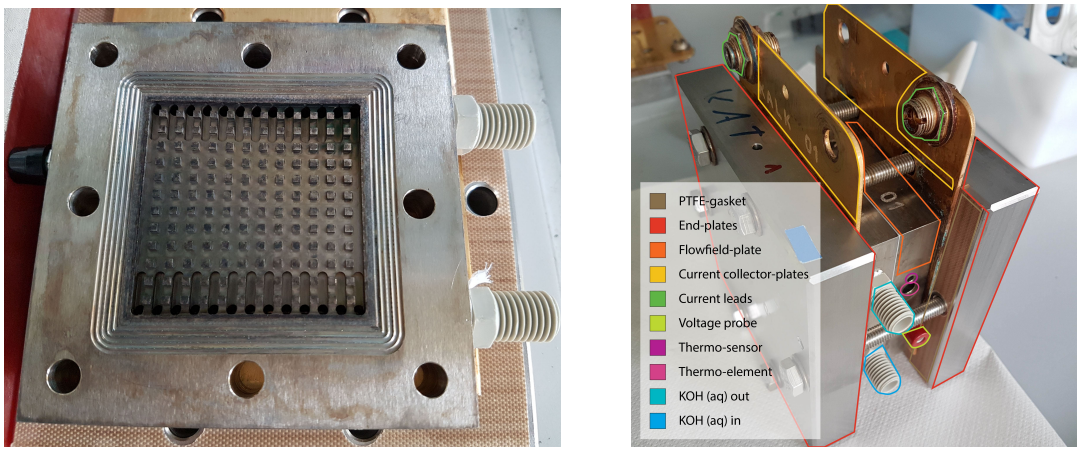

(a) **(b)**

Fig. 3.4: The FZJ cell; square geometry with active area of 5×5 cm^2. **(a)** the open back pin-type flow field and, **(b)** an assembled cell showing all the components and most of the connections.

m-PBI

The frequently used *m*-PBI membranes in this work were prepared by co-workers. The polymer was obtained from Danish Power Systems ApS or prepared in-house according to common procedures described elsewhere.[225] The polymer was cast from a DMAc solution in petri dishes and dried slowly under lid to prevent rapid evaporation. The dry as-cast membranes were washed in demineralized water for several hours to achieve pristine membranes. Prior to cell experiments membranes were equilibrated in KOH (aq) at least overnight but often for several days. The concentration of the equilibration solution were always identical to the cell electrolyte for any given membrane. Equilibration in KOH (aq) result in significant swelling and for cell purposes the membrane thickness referred to is the thickness after equilibration d_{wet}.

Using a pipette to add drops of electrolyte below and above the membrane during the horizontal cell assembly process is recommended. It prevents the membrane from locally drying and helps keeping the membrane flat during assembly.

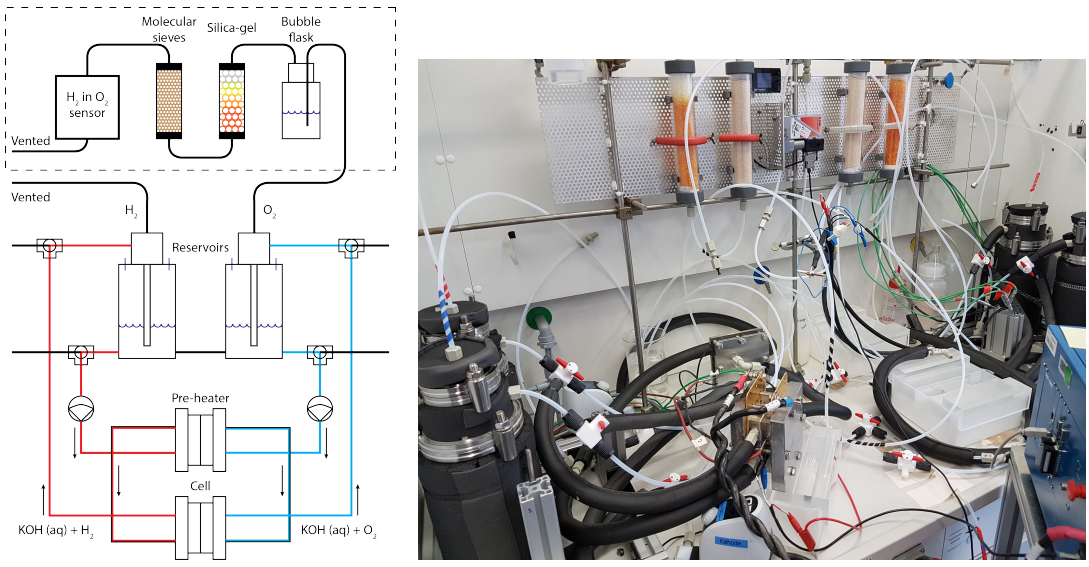

(a) **(b)**

Fig. 3.5: The test station for the FZJ cell. **(a)** A schematic illustration of the setup. The gas treatment steps marked by the dashed outline were only in operation for long term experiments. **(b)** A photograph of two test stations placed in a fume-hood. The left side has a pre-heating and active cell mounted, whereas the right station is offline. Gas drying by silica gel and molecular sieves were done in containers fixed in a rig above the setup, as seen in the top of the image.

mes-PBI

mes-PBI membranes were prepared by collaborators, and the synthesis and specific procedure is described elsewhere.[250] The mes-PBI membranes were equilibrated for at least 3 days prior to cell test.

Zirfon

Zirfon, a commercial diaphragm, was supplied by Agfa. The material consist of ZrO_2, polysulfone, and a mesh for reinforcement, and has a thickness of 500 $\pm$50 µm. Separator pieces were cut but otherwise used as-delivered.

3.1.4 Protocols and test conditions

Tests were in general conducted at $T = 80°C$, but some cells were additionally run partially at lower temperatures (20-60°C). The concentration of KOH (aq) is

for single cell tests specified by wt% rather than molarity, since the density is temperature dependent, which cause a room temperature molarity statement to be incorrect at 80°C. Flow rates of pumps were set somewhere in the range of V = 5-500 ml min^{-1} depending on pumps and electrodes, but most commonly at 100-120 ml min^{-1} (DTU) and 50 ml min^{-1} (FZJ). This correspond to reactant (water) stoichiometry in the order of 1000.

The current mode of the cells was initially to a large extent potential controlled (constant voltage), but later protocols at DTU used current control (constant current). Measurements at FZJ were done exclusively with current control.

The test protocols used during cell testing have evolved over the course of the project. The protocols generally consist of at least the following initial steps:

1. A system conditioning step (temperature and electrolyte flow)
2. A cell *activation/break-in* step at mild electrochemical conditions
3. A *polarization* curve

This is often followed by mixed operation at static and dynamic conditions depending on the specific experiments.

The specific protocols used, relevant to the presented results are presented in Table 3.1, 3.2, and 3.3. Note that some cells were run beyond the initial protocol, and that there may be minor deviations for some cells. For instance were the cells with *m*-PBI and 5 wt% KOH activated at lower setpoints than similar cells with higher KOH concentration.

There are currently no standard cell test protocols published for water electrolysis, neither by the U.S. DOE, nor the european FCH-JU, but it is being worked on.[251] In a lab context, cell failure is to be expected occasionally, hence the consequences depending on operating setpoint is worth considering.

At constant voltage, a short circuit results in very high currents, whereas decreasing performance simply lower the current density. For constant current mode, a cell with decreasing performance will increase in cell voltage, which ultimately can lead to undesired side reactions. On the otherhand, short circuiting simply make the electrochemical reactions stop and the potential drops.

Half cell electrode tests are normally done by scanning potential at a constant rate, whereas electrolysis single cells as well as stacks are nominally operated

Table 3.1: Protocol used for cell measurements while investigating *m*-PBI: Pump flow V, temperature T, current density i, and potential E.

DTU cell: *m*-PBI		
Parameter	Setpoint	Time/rate
$V_{cat} + V_{an}$	120 ml min^{-1}	
T	80°C	
i	*a*) 10 mA cm^{-2}	60 min ***Or***
	b) 50 mA cm^{-2}	15 min
E	1.2 V $\rightarrow$ 2.5 V	2.5 mV s^{-1}
i	200 mA cm^{-2}	120 min
E	1.2 V $\rightarrow$ 2.5 V	2.5 mV s^{-1}

by current density setpoint. Ultimately, there are no wrong way, but during the project the operating mode have shifted from potential scan towards a current step-scan, while static operation for the most part have been in terms of constant current. In the broader context, cell voltage is simply a parameter relating to efficiency, whereas the current relate to the product of the process. Hence, for H_2 production aspects, constant current mode is most interesting, whereas perhaps grid balancing or other electricity-price dependent applications may want to control by constant power rather than current or voltage.

3.2 Synthesis details

3.2.1 Ni-Fe

The synthesis of the Ni-Fe coatings primarily followed a procedure inspired by Lu *et al.*.[163] Synthesis of nickel-iron-(oxy)hydroxides is discussed in more detail in Section5.1.

Aqueous solution of $Ni(NO_3)_2 \cdot 6\,H_2O$, $Fe(NO_3)_3 \cdot 9\,H_2O$ (26.7 mM total metal ion concentration), and $CO(NH_2)_2$ (66.8 mM) were prepared. 80 ml solution was transferred to a 100 ml PTFE lined autoclave. The metal-nitrates act as metal-precursors whereas the urea hydrolyse at increased temperature to precipitate

Table 3.2: Protocol used for cell measurements while investigating mes-PBI: Pump flow V, temperature T, current density i, and potential E.

DTU cell: mes-PBI		
Parameter	Setpoint	Time/rate
$V_{cat} + V_{an}$	120 ml min^{-1}	
T	RT	
i	50 mA cm^{-2}	15 min
E	1.2 V $\rightarrow$ 2.5 V	2.5 mV s^{-1}
T	RT $\rightarrow$ 40°C	***While***
i	200 mA cm^{-2}	5-10 min
E	1.2 V $\rightarrow$ 2.5 V	2.5 mV s^{-1}
T	40°C $\rightarrow$ 60°C	***While***
i	200 mA cm^{-2}	5-10 min
E	1.2 V $\rightarrow$ 2.5 V	2.5 mV s^{-1}
T	60°C $\rightarrow$ 80°C	***While***
i	200 mA cm^{-2}	5-10 min
E	1.2 V $\rightarrow$ 2.5 V	2.5 mV s^{-1}

metal-(oxy)hydroxides. The amount of nickel and iron precursors were varied to change stoichiometry of the solution and samples without Fe (*10:0*) and molecular Ni:Fe ratios of *9:1*, *8:2*, *7:3*, *6:4*, *5:5* were prepared. Samples are denoted as such. Nickel foam sheets (39×80 mm^2) were briefly etched with 4 M HCl for 2 minutes, before being rinsed and transferred to the autoclave. The autoclave was heated at 2°C min^{-1} to 120°C and left for 12 hours before naturally cooling to room temperature. Prepared electrode sheets were briefly sonicated in water to remove material with poor adhesion. The electrode sheets were left to dry in air.

Electrodes were die cut with a hydraulic press into discs with diameter 38.5 mm for cell testing, and dog-bone shapes with 10×10 mm^2 shoulders and a 30 mm long, 2 mm wide neck for use in half-cell tests.

Table 3.3: Protocol used for cell measurements at FZJ: Pump flow V, temperature T, current density i, potential E, and galvanostatic electrochemical impedance spectroscopy (GEIS).

FZJ cell: Raney		
Parameter	Setpoint	Time/rate
$V_{cat} + V_{an}$	*a*) 50 ml min^{-1}	for (pp)
	b) 5 ml min^{-1}	for (f)
T	80°C	
i	40 mA cm^{-2}	12 h
i	5 mA $cm^{-2} \rightarrow$ 4000 mA cm^{-2}	5 min/pt
GEIS	5 mA $cm^{-2} \rightarrow$ 2000 mA cm^{-2}	1-2 min rest/pt

3.2.2 Ni-Sn

Aqueous solutions of $K_4P_2O_7$ (520 mM), NH_2CH_2COOH (266 mM), $NiCl_2 \cdot 6\,H_2O$ (84 mM), and $SnCl_2 \cdot 2\,H_2O$ (50 mM) were prepared by dissolving the precursors in that order. The complex forming effects of pyrophosphate and glycine inhibit Sn from oxidizing and affect deposition rates. The bath chemistry is discussed in more detail in the literature.[112] Electrode substrates were prepared by cutting nickel foam to 1 $\times$ 1.5 cm^2 pieces on which a nickel wire was spot-welding. The substrates were used as pristine for the first batch, but for second batch they were pre-treated with an alkaline degreasing step using Gardoclean® at 80-90°C for 10 minutes and an acid-etching step in 10% HCl for 5 minutes. The substrates were rinsed in-between cleaning steps. Electrodeposition was carried out in a glass beaker with the electrode substrate as working electrode (WE), a Pt counter electrode (CE), and a reversible hydrogen electrode (RHE) as reference electrode (RE). 100 ml solution were used to prepare up to 5 electrodes of 1.5 cm^2 depending on total charge passed through, as solution precursors were kept within 10% of original concentration. Deposition was done both potentiostatically (-0.78 and -1.28 V vs RHE) and galvanostatically (-50 to -250 mA cm^{-2}) depending on electrode. The electrodeposition solution pH was 8 and deposition was carried out at room temperature. Electrodes were left to dry overnight in open atmosphere, and a 1 $\times$ 0.5 cm^2 piece were cut off for physical characterization leaving electrodes with an active area of 1 $\times$ 1 cm^2.

3.2.3 Ni-Mo

The electrochemical deposition of Ni-Mo alloy followed a procedure adopted from Wang *et al*.[72]

Aqueous solutions of $NiSO_4 \cdot 6\,H_2O$ (17 mM), $(NH_4)_6Mo_7O_{24} \cdot 4\,H_2O$ (2.7 mM Mo), NaCl (281 mM), and $Na_3C_6H_5O_7$ (16 mM) were prepared. pH was adjusted to ∼9-10 and 60 ml solution was used per electrode in a 100 ml glass beaker. Electrode substrates were prepared by die cutting dog-bone shapes from nickel foam with shoulders of 10×10 mm^2 and a 2 mm wide and 30 mm long neck, and cutting the neck midway yielding two electrodes. The electrodes were degreased in 1 M KOH, rinsed, etched with 37 wt% HCl, and rinsed again. The electrode substrates were used as WE, a Pt or Ni mesh used as CE, and a RHE was used as RE. Note that the nickel CE corrode significantly and is not recommended. Deposition were carried out at -100 and -200 mA cm^{-2} for 600 or 1800 s, and the electrodes were rinsed and left to dry in air.

3.2.4 *a*-NiCoS

Cathodes labelled *a*-NiCoS were supplied by a collaborator and are proprietary technology. The electrodes are amorphous and the labelled stoichiometry does not represent the actual composition.

3.3 Half cell electrochemical tests

Electrochemical half cell tests were performed in glassware even though strong KOH solutions were used. Since half cell experiments were only conducted at room temperature, glass corrosion appear fairly limited. Nickel was used as counter electrode, and a RHE (Gaskatel HydroFlex®) was used as reference electrode. The RHE is very convenient since the 0 V value is equivalent to the reversible potential of the HER. Consequently, the reversible OER potential is always 1.23 V (at RT), hence the over potentials are easy to estimate and indepedent on pH.

The remaining experimental details varied and are covered in the following.

3.3.1 Ni-Fe

Half cell tests on NiFe-(oxy)hydroxide anodes were performed in 100 ml glass beakers. A nickel-mesh wrapped along the full circumference on the inside of the beaker made up the counter electrode, and the working electrodes (thickness, d = 1000 µm) were placed in the center. A reversible hydrogen electrode (RHE) was used as reference and was placed closed to the long edge of the working electrode. Measurements were done according to Table 3.4 by controlling the potential of working electrode against the reference. Potentiostatic electrochemical impedance spectroscopy (PEIS) were recorded with a 10 mV amplitude from 100 kHz to 10 Hz, at 15 points per decade, and the R_s were normally estimated near 25 kHz.

Table 3.4: Protocol used for half cell measurements on NiFe anodes.

Half cell: NiFe		
Parameter	Setpoint	Time/rate
E (static)	1.23 V	60 s
PEIS	1.23 V	
E (pol.)	1.23 V $\rightarrow$ 2.5 V	2 mV s^{-1}
Repeated *to a total of 3 measurements*		

Data presented in Section 5.1 is from run #2, unless it proved very noisy, in that case #3. The first run always show a different behaviour due to oxidation of the electrode. The nickel reference (Ni ref.) showed a large degree of hysteresis and the shown values are the average between the forward and backward scan for those measurement with a slightly modified protocol. The polarization scan were limited to 2000 mA cm^{-2}. Cyclic voltammetry measurements were recorded following the polarization measurements.

Measurements were recorded at room temperature in 20 wt% KOH (aq) electrolyte.

3.3.2 Ni-Sn

Nickel-tin cathode half cell test were performed in a glass beaker with 50 ml electrolyte. A 1 $\times$ 1 cm^2 nickel mesh was used a CE and placed 10-20 mm away

but parallel to the working electrode. A RHE was used as RE and place between WE and CE. Measurements followed the procedure outlined in Table 3.5

Table 3.5: Protocol used for half cell measurements on NiSn cathodes.

Half cell: NiSn		
Parameter	Setpoint	Time/rate
i (static)	-50 mA cm^{-2}	900 s
PEIS	0.0 V	
E (pol.)	0.1 V $\rightarrow$ -0.5 V	1 mV s^{-1}
i (static)	-300 mA cm^{-2}	900 s

Selected electrodes were operated galvanostatically at -300 mA cm^{-2} for several hours. PEIS measurements were recorded with a 10 mV amplitude from 100 kHz to 1 Hz, at 15 points per decade, and the R_s were normally estimated near 25 kHz.

Measurements were recorded at room temperature in 30 wt% KOH (aq) electrolyte.

3.3.3 Ni-Mo

The nickel-molybdenum half cell measurements were carried out in a setup identical to the one used for Ni-Fe electrodes with a nickel mesh as CE along the circumference of the beaker and a RHE as RE. The protocol is more elaborate and given in Table 3.6, although only a fraction of the recorded data are used.

PEIS were performed with an amplitude of 10 mV from 100 kHz to 0.1 Hz with 15 points per decade. Presented polarization data are taken from the second polarization curve and corrected with R_s values estimated based on the PEIS recorded just prior.

Measurements were recorded at room temperature in 1 M KOH (aq) electrolyte.

Table 3.6: Protocol used for half cell measurements on NiMo cathodes.

Half cell: NiMo		
Parameter	Setpoint	Time/rate
E (static)	-0.2 V	900 s
PEIS	-0.2 V	
E (static)	0.0 V	100 s
PEIS	0.0 V	
E (pol#1.)	0.05 V $\rightarrow$ -1.5 V	2 mV s^{-1}
E (static)	0.0 V	100 s
E (CV)	0.0 V $\rightarrow$ 0.1 V $\rightarrow$ 0.0 V $\times$ 9	10 to 1000 mV s^{-1}
E (static)	0.0 V	100 s
PEIS	0.0 V	
E (pol#2)	0.05 V $\rightarrow$ -1.5 V	2 mV s^{-1}

3.3.4 Porous nickel electrodes and *a*-NiCoS

Porous electrodes prepared with nickel powders were tested in a setup similar to the Ni-Mo electrodes, with a nickel counter encircling the WE and a RHE reference. The protocol followed is shown in Table 3.7. The tested amorphous-NiCoS cathode were evaluated in the same way.

Table 3.7: Protocol used for half cell measurements on porous nickel based cathodes.

Half cell: Porous Ni		
Parameter	Setpoint	Time/rate
E (static)	0.0 V	60 s
PEIS	0.0 V	
E (pol.)	0.01 V $\rightarrow$ -1.0 V	2 mV s^{-1}
Repeated *to a total of 2 measurements*		

PEIS were performed with an amplitude of 10 mV from 100 kHz to 10 Hz with 15 points per decade, and polarization data are taken from the second run.

Measurements were recorded at room temperature in 20 wt% KOH (aq) electrolyte.

3.4 Equipment and techniques

3.4.1 Equipment

Electrochemical tests

Electrochemical half cell measurements were recorded with a VersaSTAT potentiostat from Princeton Applied Research using the accompanying VersaStudio software. Single cell tests at DTU were done using an Elektro Automatik EA-PS 3016-20 B power supply unit controlled by a LabVIEW interface. Single cell tests at FZJ were recorded with a BioLogic HCP-1005 potentiostat with a 100 A booster module. Durability tests at FZJ were kept at constant current using a different external power supply, but swapped to the BioLogic potentiostat for polarization and impedance measurements.

Scanning electron microscopy and energy dispersive X-ray spectroscopy

Scanning electron microscopy (SEM) was done on a Zeiss EVO MA 10 scanning electron microscope with a secondary electron and backscatter electron detector. Energy dispersive X-ray spectroscopy (EDX) was done with a Oxford EDX X-max 80 mm^2 detector.

X-ray diffraction

X-ray diffraction were done with a Rigaku MiniFlex 600 diffractometer Cu K_α (λ = 1.54056 Å).

Fourier transform infrared spectroscopy

Fourier transform infrared spectroscopy (FTIR) was done using a PerkinElmer Spectrum Two spectrometer with a UATR single reflection diamond.

Size exclusion chromatography

Size exclusion chromatography (SEC) was carried out on a Shimadzu HPLC instrument, equipped with 2 PolarSil columns (100 and 300 Å) from Polymer Stan-

dards Service, and a Shimadzu refractive index detector. The system was controlled by the LabSolutions GPC software. The mobile phase was composed of DMAc with 0.25 or 2.5 wt% LiCl.

Cross-section sample preparation

Cross-section samples for SEM were prepared using a Hitachi E-3500 ion milling system.

Membrane conductivity measurements

Membrane conductivity was measured through-plane using a dedicated tubular conductivity cell. The cell consist of two parts, with nickel mesh electrodes fixed in each block. The cell blocks were assembled with the membrane sandwiched between them and submerged in a beaker with aqueous KOH. Cell resistances were measured using impedance with the membrane R and without R_{blank}, and the conductivity σ of the membranes were calculated knowing the cell tube area A (inner diameter 9 mm) and the membrane thickness d.

$$\sigma = \frac{d}{A \times (R - R_{blank})} \tag{3.1}$$

Electrolyte conductivities were obtained from R_{blank}, knowing the blank cell electrode spacing of 4.6 mm. Temperature was controlled by placing the entire assembly inside an oven.

3.4.2 Electrochemical impedance spectroscopy

Impedance is the effective resistance of a circuit or an electrical system to an alternating potential or alternating current perturbation. Not all systems show a linear ohmic response, hence a certain frequency dependent latency, a phase shift, can appear between the perturbation and the response. The impedance Z can be seen as the complex extension of the resistance R, that accurately describe the potential-current behaviour in non-ohmic systems. In complex notation ($i = \sqrt{-1}$), a sinusoidal potential signal of amplitude E_0 and angular frequency ω, is written as,

$$E(\omega) = E_0 e^{(i\omega t)} . \tag{3.2}$$

This has a current response with the amplitude I_0, which can show a phase shift ϕ, and be written as

$$I(\omega) = I_0 e^{(i\omega t - i\phi)} . \tag{3.3}$$

The impedance with magnitude Z_0 is then the quantity defined as

$$Z(\omega) = \frac{E(\omega)}{I(\omega)} = \frac{E_0 e^{(i\omega t)}}{I_0 e^{(i\omega t - i\phi)}} = Z_0 \left[\cos(\phi) + i \sin(\phi)\right] , \tag{3.4}$$

which can be separated into a real $Z_{re} = Z_0 \cos(\phi)$ and an imaginary $Z_{im} = Z_0 \sin(\phi)$ part. The impedance contribution from different electrical components can be derived, for e.g. a resistor R, a capacitor C, or an inductor L.

$$Z_R(\omega) = R \tag{3.5}$$

$$Z_C(\omega) = \frac{1}{i\omega C} \tag{3.6}$$

$$Z_L(\omega) = i\omega L \tag{3.7}$$

On this basis, the total response of more complex systems can be calculated.

This can be applied in electrochemistry as electrochemical impedance spectroscopy (EIS) by measuring the impedance response in a wide range of frequencies. The frequency range frequently cover 6 orders of magnitude e.g. from 10^5 Hz to 10^{-1} Hz, with points being logarithmically spaced. This generate a spectrum of Z_{re} and Z_{im} data pairs varying in frequency ($\omega = 2\pi f$), which are often plotted with Z_{re} as x-axis and $-Z_{im}$ as the y-axis, in what is called a Nyquist plot. An example of an ideal electrochemical response is shown in Figure 3.6.

Many electrochemical systems can be approximated with equivalent circuit models. The ohmic behaviour of the electrolyte can be approximated with a resistor (R) and electrodes are commonly approximated by a resistor (R) and a capacitor (C) in parallel (RC). The resistor correspond to the charge transfer resistance for a given faradaic reaction, and the capacitor model the electrical double layer. Hence, a full electrochemical cell with two electrodes and an electrolyte can be modelled in series as RC-R-RC. Figure 3.7 illustrate the RC-R-RC equivalent circuit that could be used to model an electrochemical cell with cathode (cat), electrolyte, and anode (an). In practice, the capacitor is often replaced with an effective capacitor, called a constant phase element (Q), due to the non-ideal behaviour of real electrodes, caused by e.g. surface roughness.

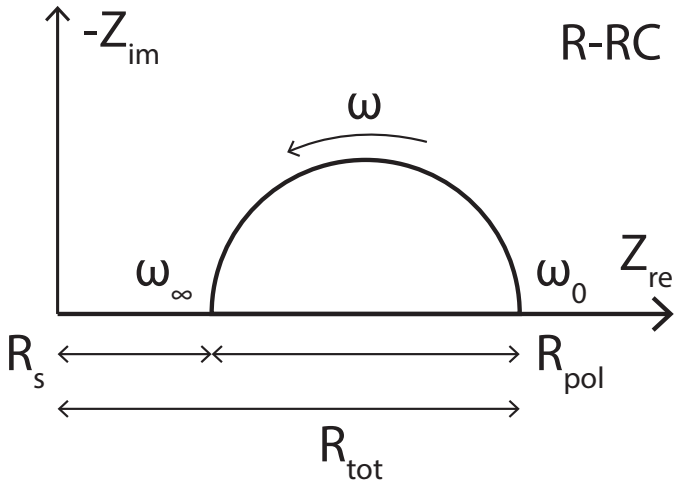

Fig. 3.6: Idealised nyquist plot for a R-RC equivalent circuit. The high frequency x-axis intercept represent the series resistance R_s, and the low frequency intercept represent the total cell resistance at direct current R_{tot}, including polarization processes. The difference represent electrochemical polarization resistances R_{pol}.

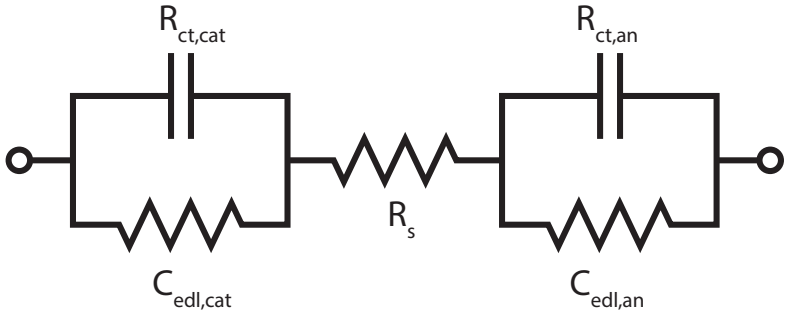

Fig. 3.7: Equivalent circuit model that can be used to model or fit the response obtained from electrochemical impedance spectroscopy.

To extract information from impedance spectra one can fit the data to an equivalent circuit. In this project this is done using the in-house software RavDav. Alternatively, some values can be extracted directly from the Nyquist plot. The idealised data in Figure 3.6 represent a R-RC circuit, and can be used to directly extract the ohmic resistance in the system, often called the series resistance R_s, at the high frequency intercept with the x-axis. For a single electrode, what is marked as R_{pol}, between the high and low frequency intercepts, would correspond to the charge transfer resistance, and the capacitance could be obtained from the summit frequency of the arc through $C = (2\pi Rf)^{-1}$. In this thesis R_s, R_{pol}, and R_{tot} are used as they are labelled in Figure 3.6.

4

Results with PBI membranes

The PhD project have touched many aspects of alkaline water electrolysis. One of them is the use of alkaline membranes based on polybenzimidazole as electrolyte, which is addressed in this chapter.

4.1 *m*-PBI as electrolyte

The concept of applying alkaline membranes in electrolysis have been discussed in literature,[32] and offer the prospect of a greatly reduced inter-electrode distance and subsequent reduction in ohmic resistance. Unlike PEM, the alkaline environment has no need for scarce and expensive noble metal catalysts, hence it constitute a technological pathway to reducing production costs of green hydrogen in the long run. As discussed previously, two primary approaches are pursued in the literature, and in our case we have looked towards ion-solvating membranes based on polybenzimidazole.

Based on previous work[228,229] it was clear that *m*-PBI suffer from some chemical stability problems *ex-situ*, but we wanted to evaluate the *in-situ* performance under different conditions and the consequences for the membrane of being operated under electrolysis conditions. As electrodes nickel foam was used for both cathode and anode in its pristine form. Plain nickel materials serve in

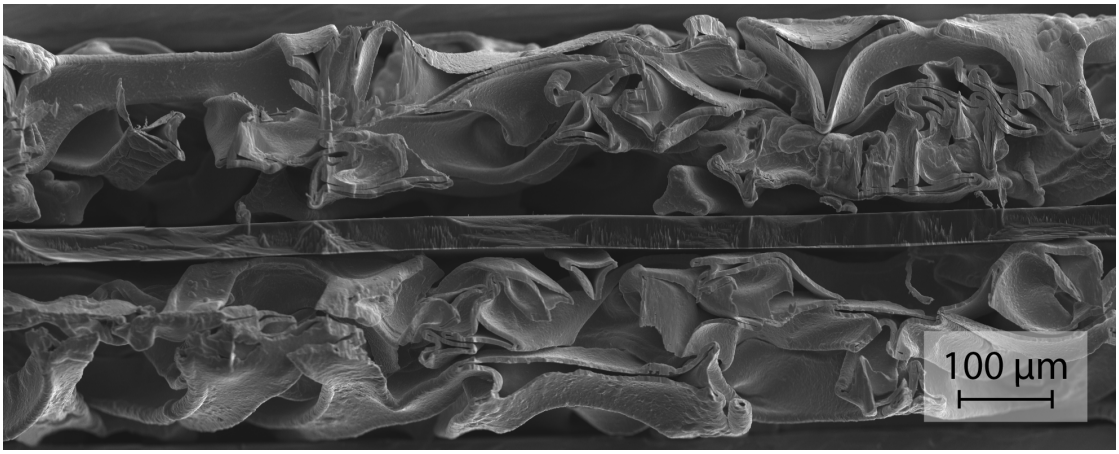

Fig. 4.1: SEM cross-section micrograph of a Ni(f) | *m*-PBI | Ni(f) MEA. The membrane is dry and undoped.

many cases as reference or base-line materials against which to compare more advanced electrodes. This is also the case in our study. An example of a MEA with compressed nickel foam electrodes is shown in Figure 4.1.

4.1.1 Electrolysis performance

One of the primary experimental parameters is the concentrations of the liquid alkaline electrolyte. It is known that the electrolyte uptake, as well as the ionic conductivity depend on bulk solution concentration in which the membrane is equilibrated. The electrolysis behaviour in terms of electrolyte concentration [KOH], is shown in Figure 4.2. As a reference, a commercial porous diaphragm (Zirfon) was tested in 30 wt% KOH as conventionally used, and is shown for comparison.

There are a few things to note: 1) The ohmic behaviour is for all concentrations $\geq$ 15 wt% significantly better that that of Zirfon. This is a result of high conductivity and sufficiently thin membranes. For these cells, membranes were cast based on reported swelling behaviour[229] to have a post-equilibration thickness, d_{wet} of 50-60 µm. Hence, the improvement in ohmic behaviour is partly due to a 10-fold decrease in thickness over Zirfon. A reduction of thickness is, however, one of the points of using membranes in the first place. 2) The behaviour in 20-30 wt% range is not vastly different, but the optimum appear in this case to be closer to 20 wt% rather than 30 wt%, which otherwise show optimal con-

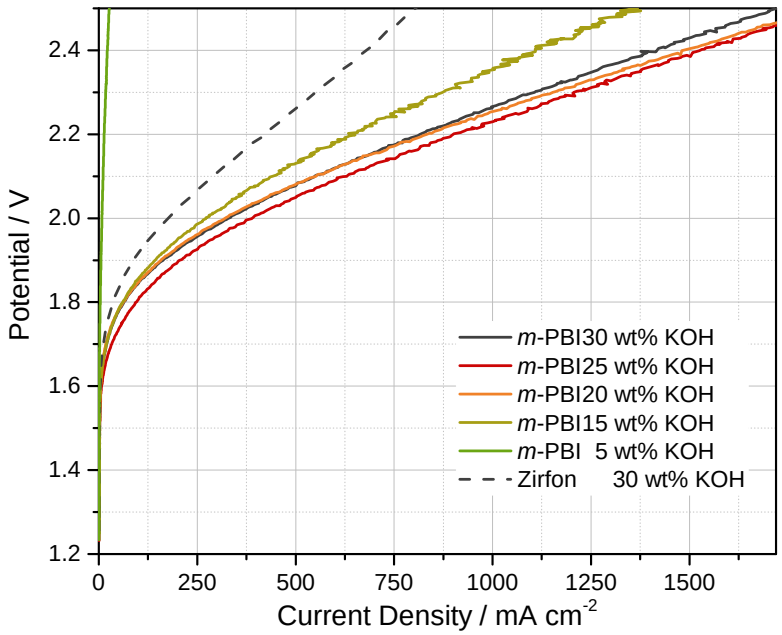

Fig. 4.2: Polarization behaviour of cells with membranes equilibrated at different KOH (aq) concentrations. Electrolyte concentration is identical to equilibration concentration. The cathodes and anodes were pristine nickel foam pressed to 210 µm (1000 µm for 5 wt%). *m*-PBI thickness d_{wet} = 50-60 µm, T = 80°C, flowrate = 120 ml min^{-1}, flowfield = linear.

ductivity for bulk KOH (aq).[204] 3) At low KOH concentrations, e.g. 5 wt% ≈ 1 M, the cell resistance is very high, and only about 20 mA cm^{-2} is achieved at 2.4 V. This is in contrast to around 1500 mA cm^{-2} at 2.4 V for the 20 wt% cell. 1 M KOH is a common concentration choice for AEM-based APEM electrolysis cells, and clearly other AEM-type membranes are vastly more conductive at low concentrations. 4) A small activation difference is noted for the cell at 25 wt%, however this is, at least in principle, unrelated to the membranes, hence it is not considered in the previous discussion.

Tafel fits using eq. (2.22) can be used to estimate the ohmic resistance of the cell but is less reliable than impedance and are for instance unable to catch trends in ohmic resistance as functions of current density. Other effects that appear ohmic will also cause a possible miss-interpretation, hence some caution towards quantitative values extracted must be exerted. Nonetheless, using data for i > 5 mA cm^{-2}, we find values in order from 5 to 30 wt% of 13.1, 0.35, 0.24, 0.26, 0.27 Ω cm^2, corresponding to specific conductivites of 0.4, 15, 26, 22, and 19 mS cm^{-1}, assuming the membrane as the sole contributor.

Conductivity

The ohmic response of an electrolysis cell is closely connected to the specific resistance across the separator, hence the membrane conductivity is of high importance. The specific conductivity of *m*-PBI membranes was measured in this context at different solution concentrations and temperatures, and the data is presented in Figure 4.3. The measured specific conductivity of the bulk electrolyte is plotted for comparison, and fit well with literature data. The specific conductivity of the membranes peak at KOH concentrations around 20-25 wt%. The presented data show the peak at 25 wt%, whereas previous data[228] found peak room temperature conductivity at 20 wt%. Nonetheless, the 20-25 wt% range is lower than the $\sim$ 28-32 wt% where the specific conductivity of bulk KOH (aq) peaks at relevant temperatures according to literature data. In either case, a specific conductivity of 100 mS cm^{-1} is in the practically interesting range, and $\sim$ 250 mS cm^{-1} at 80°C quite respectable. It should be noted that these data are obtained *ex-situ* by an AC-impedance method, hence potassium ions may contribute to larger extent than in the real cell. However, even with a transference number, i.e. the relative contribution of the specific ion, for hydroxide at around $\sim$ 0.7,[41] the OH^- conductivity would still be in the range of 150-200 mS cm^{-1}. Note that while the transference number inside the membrane may be lower, since the potassium polybenzimidazolide form in Figure 2.11 is essentially a cation exchange material, it is still a respectable OH^--conductivity.

Static operation

In connection with these baseline tests it was investigated how different operating conditions affected degradation. Hence, cells were operated at 1.7 or 2.0 V, in KOH concentrations of 5, 15 and 30 wt%. The potentiostatic behaviour of each cell is plotted in Figure 4.4.

Even before performing any post-cell characterization on the membrane we learnt some practical lessons. Initial runs were operated with 1000 µm nickel foam electrodes (1100 µm compressed to 1000 µm). It was later seen to be problematic, as short circuiting frequently occurred in the cell even prior to any current being drawn simply due to physical compression. The higher the KOH concentration, the softer the membranes gets and the issue becomes more severe. It was concluded that the electrodes were too uneven, so pressed electrodes was

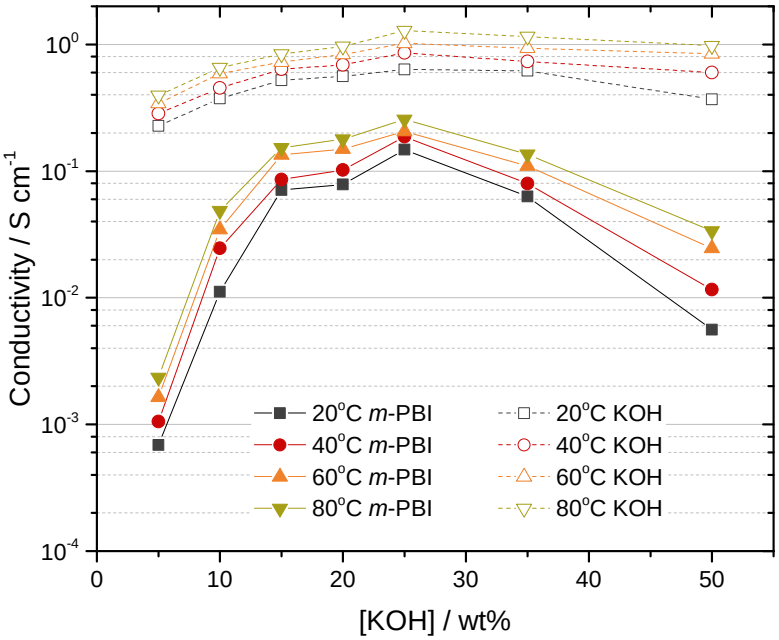

Fig. 4.3: Specific conductivity of *m*-PBI and KOH (aq) as recorded by AC-impedance in a dedicated conductivity cell.

used henceforth. The mechanical properties of the *m*-PBI membranes weaken with increasing doping levels, and at e.g. 25 wt% is the young's modulus an order of magnitude lower compared to undoped PBI, decreasing from 3 GPa to 0.3 GPa.[229] Cell compression is important to ensure good electrical contact between electrodes and flowfields, and to prevent void space between the membrane and electrodes. However, too strong compression may compromise the membrane integrity. Hence, the thickness of the gaskets must chosen based on the electrode and membrane thickness, such that electrode compression is neither too strong nor too weak.

New experiments were conducted with 210 µm electrodes (compressed from 1100 µm), and no short circuiting was experienced during the two-day measurements. Some secondary issues were, however, encountered. Although not quantified, there appeared to be a migration of electrolyte from the anode chamber to the cathode chamber, roughly proportional to the current density or the total charge passed through the membrane. This lead to a dry-out of the anode chamber for the first cell operating with at high current density (~ 350 mA cm^{-1} at 2.0 V in 30 wt% KOH), and probably an increase in mechanical stress on the membrane as well as a significant drop in performance and increase in noise,

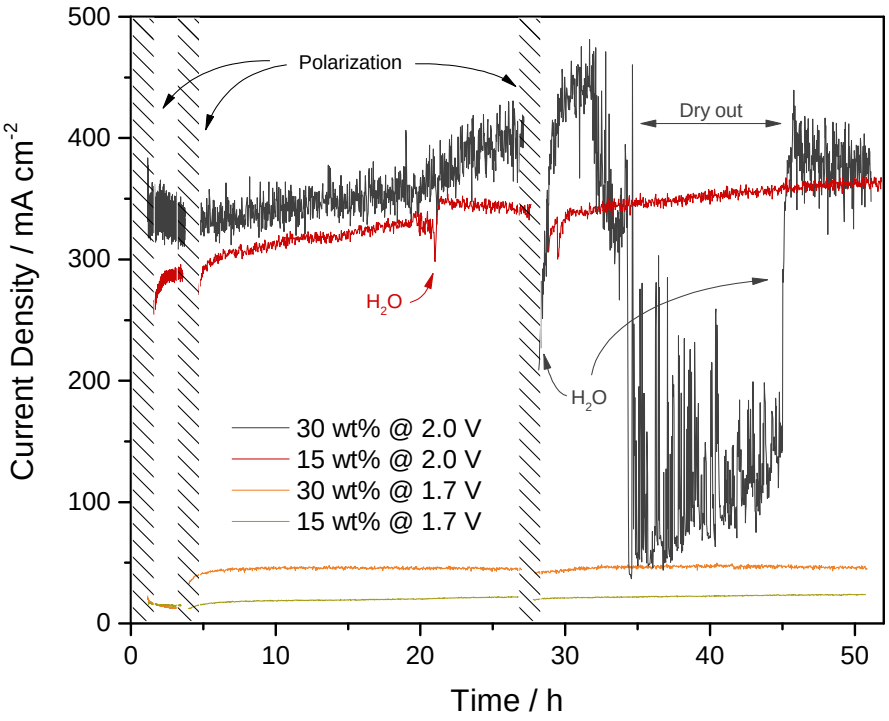

Fig. 4.4: Potentiostatic operation for 2 days with 210 µm nickel foam electrodes. Polarization curves were recorded at three occasions during the test, and water was added as necessary. Both are marked in the figure. *m*-PBI thickness d_{wet} = 50-60 µm, T = 80°C, flowrate = 120 ml min^{-1}, flowfield = linear.

c.f. the dark curve in Figure 4.4. Miscellaneous measurements after the potentiostatic operation, including changes in electrolyte flow rate, lead to a short circuiting, and a large hole was observed in the membrane upon visual inspection after cell disassembly.

Polymer degradation

The membranes were analysed after 48 hours of cell testing. Following a washing step to remove the KOH, FTIR and SEC measurements were performed. Data for cells run at 2.0 V are presented in Figure 4.5. The FTIR data reveal no significant changes for the cell operated in 5 wt% KOH compared to a reference sample, whereas the 15 wt% cell show broadening of the band around 1400 cm^{-1}. The appearance of a distinct peaks at 1380, 1560, and 1690 cm^{-1} is clear for the cell operated at 30 wt%. The band near 1380 cm^{-1} has been been assigned to free amino groups indicating hydrolysis of the backbone structure of the poly-

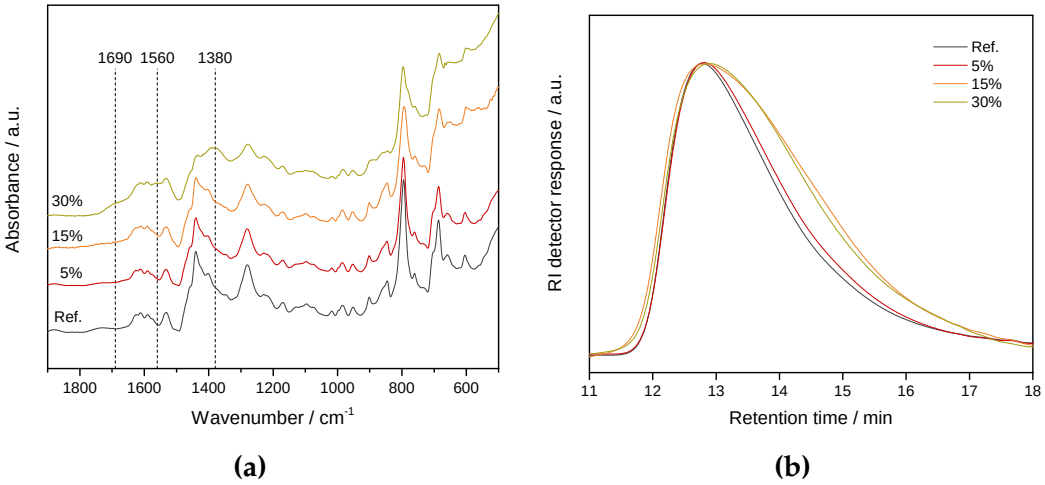

Fig. 4.5: **(a)** FTIR spectra and, **(b)** Size exclusion chromatogram of *m*-PBI membranes after 2 day cell operation at 2.0 V at different KOH (aq) concentrations.

mer,[227] whereas the 1560 cm^{-1} is uncertain and may relate to some oxidation of the polymer. The peak at 1690 cm^{-1} can indicate formation of carbonyl moieties.[252] The SEC data support polymer backbone scissoring as the peak shape change towards higher retention times indicating smaller molecular sizes. In addition, a small change towards lower retention time is also observed, possibly due to agglomeration. Again, the 5 wt% cell does not appear notably different from the reference, whereas the 15 and 30 wt% cells have a clear change.

The attack is previously described to take place at what is known as the C2 position,[227] as illustrated in Figure 4.6. The consequence is a scissoring of the polymer chains, which result in shorter chains, weakening mechanical properties, and ultimately polymer loss from the membranes.

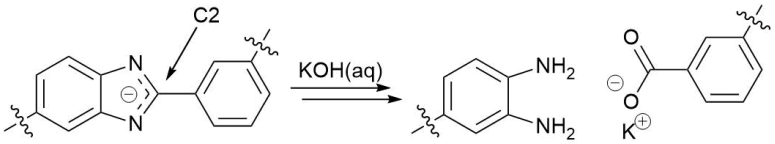

Fig. 4.6: Schematic illustration showing hydrolysis of *m*-PBI.

The initial investigation of *m*-PBI as electrolyte in alkaline electrolysis have demonstrated good ohmic performance, but cells with nickel electrodes did not provide much insight into what performance can be achieved using good electrodes. Furthermore, although increased degradation is observed, questions regarding lifetime remained unanswered.

4.2 *m*-PBI with active electrodes

At Forschungszentrum Jülich (FZJ) in Germany, there are ongoing activities in both PEM and alkaline electrolysis. As a part of the present project, an exchange stay was conducted at FZJ, at which the following results were obtained (Section 4.2).

The Forschungszentrum had been provided with Raney-nickel electrodes prepared by vacuum plasma spraying at the German Aerospace Center in Stuttgart (DLR, Deutsches Zentrum für Luft- und Raumfahrt). The electrodes were available with a molybdenum component (Ni:Al:Mo $\sim$ 52:38:10 wt%) and without (Ni:Al $\sim$ 54:46 wt%). As reviewed, these electrodes have been shown to be both highly active for the HER and durable even at 80°C, 30 wt% KOH (aq) under dynamic operation at 300 mA cm^{-2} for several thousand hours.[253]

At FZJ cells were run with 3 questions in mind:

- What performance can be achieved using active electrodes?
- What is the lifetime of the cell under conventional conditions?
- How are the gas crossover properties of the cells using *m*-PBI membranes?

Lastly, some work was conducted towards preparing electrodes from nickel powder, but this is covered in Section 5.3

4.2.1 Polarization properties

Raney electrodes must be activated prior to cell testing. This means selective leaching of most of the Al (or Zn) present in the alloy structure. The procedure for this activation is not without importance for the performance, but was not investigated. Some literature can be found on the topic.[130,131] In our case, we used 24 wt% KOH (aq) at 80°C for 24 h, with addition of 100 g/L of disodium-tartrate-tetrahydrate. 0.5 L was heated to 80°C, and 2 to 4 electrodes (50-100 cm^2) was submerged simultaneously for 24 h. After a few seconds the electrodes started to release gas bubbles. After 24 h the electrodes were withdrawn and rinsed briefly before being stored in water. Note that the ideal activation likely depend on the preparation procedure and will be different for different preparation methods, and that the activation here followed may not represent the optimal procedure.

The Raney coatings were applied to perforated nickel plates, and therefore cells have been run with plain nickel both in the form of foams (f) and in the form of perforated plates (pp). The labels **(f)** and **(pp)** will be used to clarify the electrode geometry in the following figures. Systematic investigations on polarization behaviour was done to compare the performance of Raney-nickel-molybdenum (R-NiMo(pp)) as a cathode material against a bare nickel foam (Ni(f)), and to compare *m*-PBI with Zirfon. For these investigations, a nickel perforated plate (Ni(pp)) was used as anode. For these cells the anode was fixed to the anode flow-plate by spot-welding. 2-3 sister cells were run with each configuration, and the error bar in the following graphs represent the standard deviation between measured points. An overview over different cell variations is presented in Figure 4.7.

It is evident from Figure 4.7a and 4.7b, that a significant activation improvement is obtained by utilizing high surface area materials. Notably also, when considering nickel as both cathode and anode as a reference material, there are very significant performance gains to achieve by activating the cathode. Similarly, and equally clear from Figure 4.7c and 4.7d, there are vast improvements to gain in the high current density regime when implementing thin membranes over conventional thick porous diaphragms. Interestingly, the ohmic response of the R-NiMo(pp) | Zirfon | Ni(pp) cell (▼) in Figure 4.7a and 4.7d appear different from the Ni(f) | Zirfon | Ni(pp) cell (■). Zirfon has been observed to show varying degree of performance and generally only good data are included. Some filtered data from poor cells with significantly deviating data are in Figure 4.7a shown with open markers. The variations may be caused gas trapping in the porous structure. The porous diaphragm is not suited for zero-gap configuration which is here used for all cells, hence the optimal performance achievable with Zirfon may not be realised in this case with the R-NiMo(pp) cathode. Consequently the difference in Figure 4.7d may appear somewhat exaggerated, but there will in either case be a significant difference.

As shown in Figure 4.7b and 4.7d we achieve extraordinary performance compared to conventional alkaline electrolysis. This is even when using only a unmodified nickel perforated plate as anode. A discussion of likely incidental iron activation is treated later in Section 5.1. It fell natural to also apply the Raney-nickel (R-Ni) as anode material, and the results are shown in Figure 4.8, together with curves illustrating the combined benefit of changing membrane and cathode.

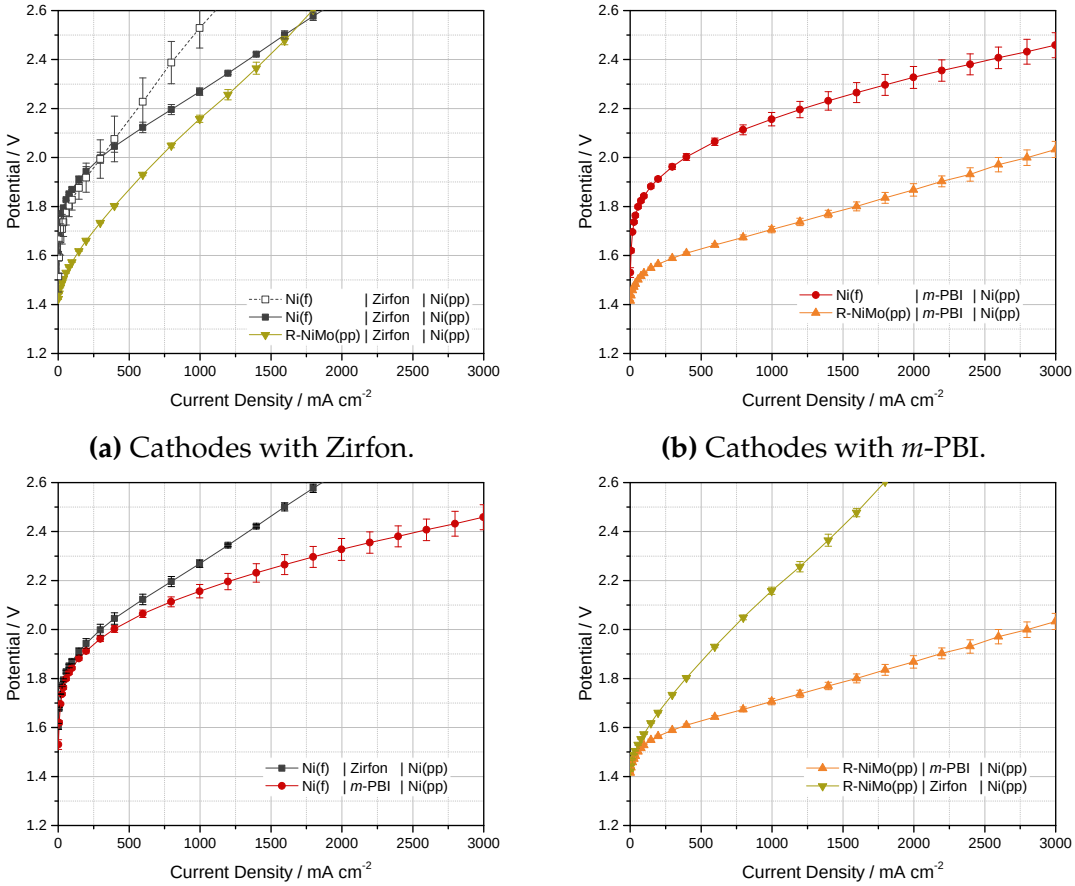

(a) Cathodes with Zirfon.

(b) Cathodes with *m*-PBI.

(c) Separators with Ni(f) cat.

(d) Separators with R-NiMo(pp) cat.

Fig. 4.7: Polarization curves following 12 h break-in. Effects of replacing individual cell parts; **(a)** Ni(f)→R-NiMo(pp) with Zirfon, **(b)** Ni(f)→R-NiMo(pp) with *m*-PBI, **(c)** Zirfon→*m*-PBI with Ni(f), **(d)** Zirfon→*m*-PBI with R-NiMo(pp). *m*-PBI thickness $d_{wet} = 40$ µm, $T = 80°C$, [KOH] = 24 wt%, flowrate = 5 ml min^{-1} for foam (f) and 50 ml min^{-1} for perforated plate (pp), flowfield = pin(FZJ).

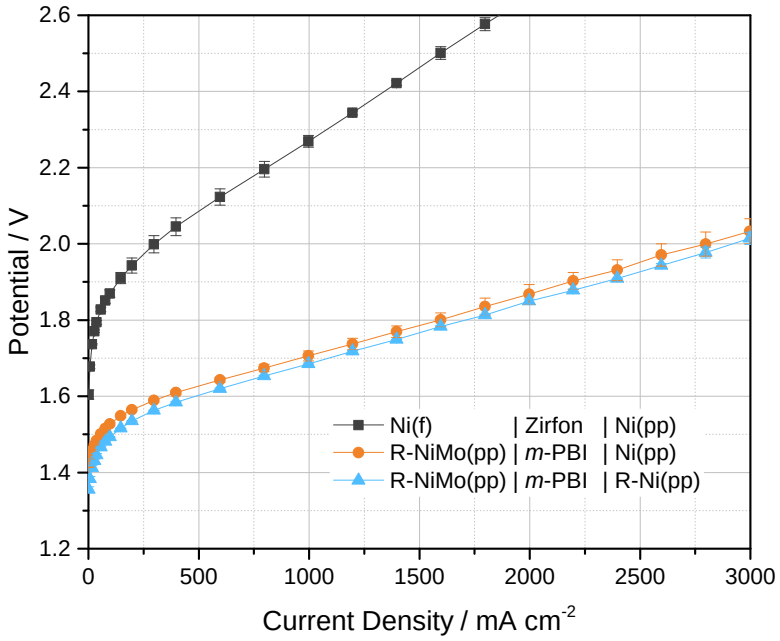

Fig. 4.8: Polarization curves following 12 h break-in. Combined effects of improving cathode and membrane, and the contribution from a Raney-nickel anode. *m*-PBI thickness d_{wet} = 40 µm, T = 80°C, [KOH] = 24 wt%, flowrate = 5 ml min^{-1} for foam (f) and 50 ml min^{-1} for perforated plate (pp), flowfield = pin(FZJ).

It is clear that there is a benefit, but it is rather limited and corresponds to no more than ∼ 20-30 mV at current densities above 200 mA cm^{-2}. Interestingly, it appears to be a larger benefit in the low current density range (< 200 mA cm^{-2}), peaking at 5 mA cm^{-2}, which is the lowest value in the polarization curve. Here the difference is 60 mV. This behaviour could be explained by differences in tafel slope of the freshly activated R-Ni electrodes versus that of Fe-contaminated Ni electrodes, or O_2 gas blocking of a large part of the pore structure at higher current densities, eliminating part of the benefit. The interplay between electrode geometry and bubble properties is difficult to quantify and nano and/or microporosity does not make it easier.

Although not really surprising considering previous experiment of the individual components, we achieve record breaking polarization performance for alkaline electrolysis without using non-noble metal catalysts. At 2.0 V we obtain 2900 mA cm^{-2} with the R-Ni anode, and with plain nickel anode, we reach 2800 mA cm^{-2}. Conversely, we only need 1.7 V to reach 1000 mA cm^{-2} with the Ni(pp) anode and ∼ 1680 mA cm^{-2} with R-Ni(pp).

Impedance investigation

The behaviour of several cells were probed by performing electrochemical impedance spectroscopy (EIS) in galvanostatic mode. In brief, a secondary step-wise polarization curve were recorded after the initial one albeit only up until 2000 mA cm^{-2}. Since this was not meant as a detailed impedance study, no measurements were performed with systematic variations to elucidate the different arcs in the spectrum. Figure 4.9 shows Nyquist plots of the impedance spectra at five different current density setpoints.

A preliminary evaluation reveal that the cell with zirfon (○) shows an expectedly much higher R_s than those with m-PBI (○ + ○). A qualitative difference in the polarization arcs is also evident between the cell with R-NiMo(pp) cathode (○) and those with Ni(f), but this does not upfront reveal any information. Lastly, the combined full polarization resistance decrease as current density, hence overpotential, increases. The low frequency impedance correspond to the tangential resistance, i.e. the slope of the polarization curve at any given setpoint. Since tafel kinetics predict a logarithmic dependence of overpotential on current density, the polarization contribution is expected to decrease roughly proportional to $1/i$. However, due to additional effects a simple $1/i$ fit is not very good.

To obtain more detailed information generic L-R-RQ-RQ or R-RQ-RQ equivalent circuit models were fitted to the data. The scope was primarily to investigate the series resistance R_s (high frequency resistance). The R-RQ-RQ fit gave good mathematical fits, but are not necessarily physically meaningful in relation to transport phenomena, charge transfer resistances, and differentiation between the different electrode contributions. This is, however, not an issue when we are primarily interested in the series resistance R_s and the total polarization resistance R_{pol}, and their behaviour as a function of current density. Figure 4.10 shows the data as open markers, with equivalent circuit fits as solid lines. Figure 4.10d and 4.10c are enlargements of the high frequency intercept region. As can be seen from the figures the overall fits are mathematically good approximations.

It should be noted that some high frequency data have been filtered due to high levels of noise, and not every cell gave good quality EIS data. Noise issues were a common issue for some cells and were to a significant extent caused by pulsing electrolyte pumps, hence dependent on flow rate and the specific test

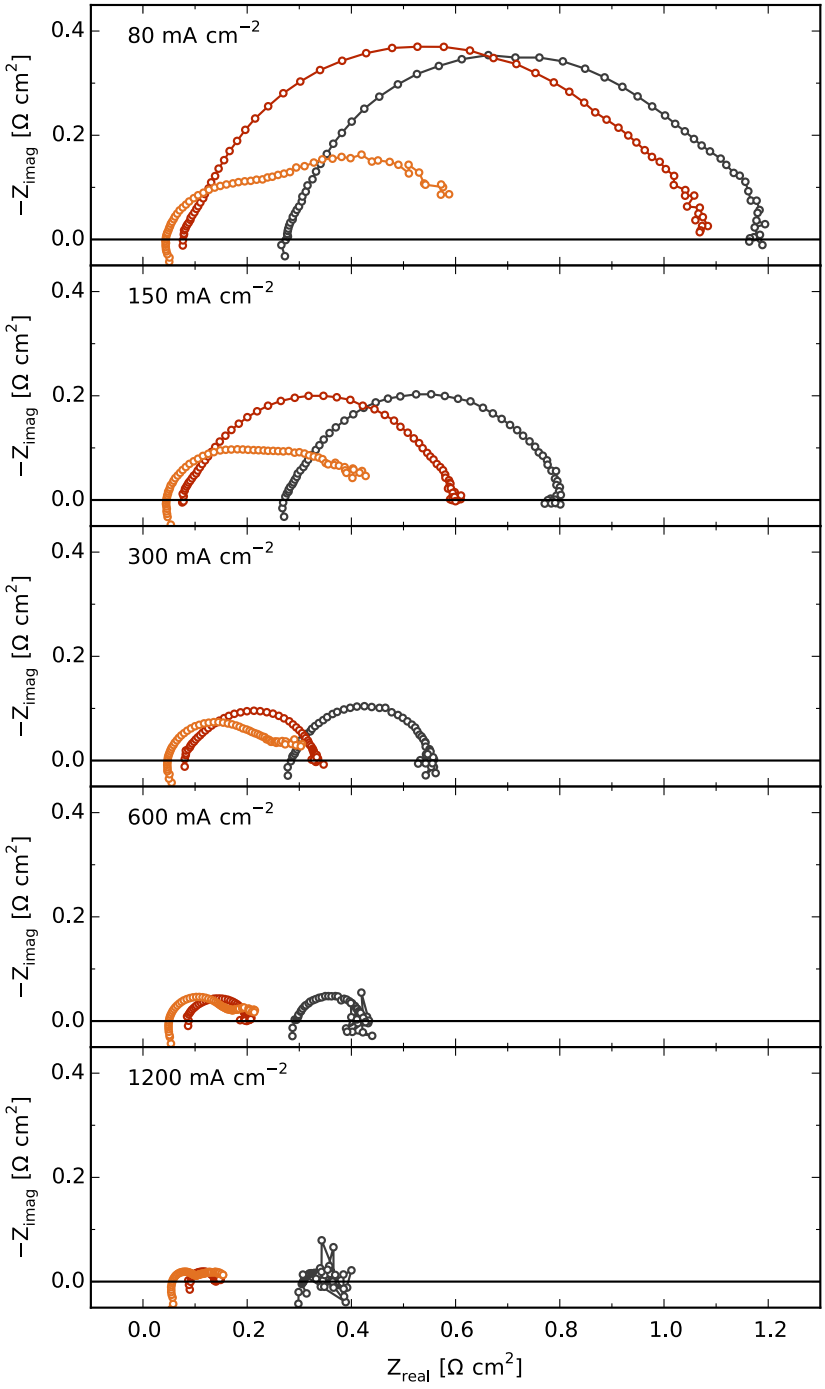

Fig. 4.9: GEIS (25 kHz-1 Hz) for 3 different cells at 5 selected current density setpoints with an amplitude of 10% of the current density setpoint. Grey (○): Ni(f) | Zirfon | Ni(pp), red (○): Ni(f) | *m*-PBI | Ni(pp), and orange (○): R-NiMo(pp) | *m*-PBI | Ni(pp). *m*-PBI thickness, d_{wet} = 40 µm, T = 80°C, [KOH] = 24 wt%, flowrate = 5 ml min^{-1} for foam (f) and 50 ml min^{-1} for perforated plate (pp), flowfield = pin(FZJ).

station.

It can be seen that there is a general trend towards an increase in R_s following increasing current densities, which can be explained by an increased presence of gas bubbles even though the electrodes are in zero-gap. Local surface blocking effectively reduce the access to some active sites, hence leading to active areas experiencing increased current densities and correspondingly resulting in a larger resistance. Similarly, not all parts of the electrode is in direct contact with the membrane, hence electrolyte void formation due to gas bubbles in front of some active sites increases the length of effective ionic pathway. Interestingly, the trend appears to reverse at $\sim$ 1000 mA cm^{-2} for cells with a nickel foam cathode. Looking at different cells (not shown) with Ni(f) cathodes it appears to be an actual effect, but the data is not clear since most other cells using Ni(f) cathodes display large levels of noise. In the case that the reverse trend is an actual effect it could be linked with changes in local flow regime, but any deeper analysis on grounds of available data is mostly guesswork.

Fitted values of R_s can neatly be summarized as shown in Figure 4.11a for different cells. Ni(f) cathode values (■,●) represent single cell data sets, whereas the R-NiMo(pp) cathode data (▼) is averaged from two cells with practically identical data. The outlying values at 100 mA cm^{-2} appeared in a number of data sets, and could be due to internal switching in the potentiostat at the current-range limit between booster mode and without. There is a very significant difference in R_s between the Zirfon and the *m*-PBI cells as would be expected. Furthermore, even the two cells with identical membranes but different cathodes, show quite a large discrepancy in R_s values. Hence, either the membrane is severely deformed by the electrodes, or the ionic resistance in the liquid electrolyte and electrode resistances contribute substantially.

Membrane resistance

By looking at sister cells with different membrane thickness we can approximate the membrane contribution to the R_s on basis of a set of assumptions. 1) Compression of the membrane from electrodes due to cell fixture is uniform, and for sake of approximation negligible. 2) No significant thinning is caused by the operation of these cells prior to GEIS measurements, hence the nominal membrane thickness is valid. As will be discussed later, this may not be the case, and we note that the time of the GEIS measuremenets are not identical across

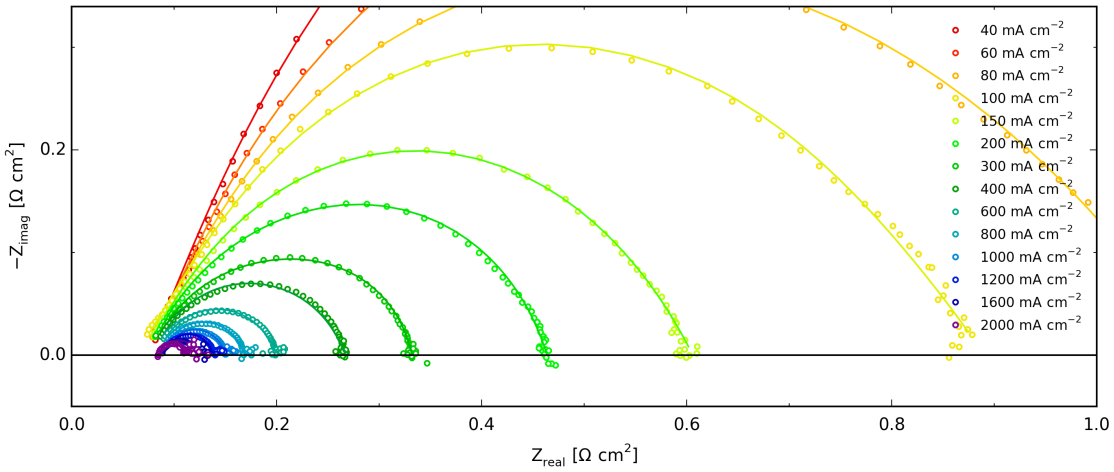

(a) Ni(f) | *m*-PBI | Ni(pp), 12 kHz-1 kHz.

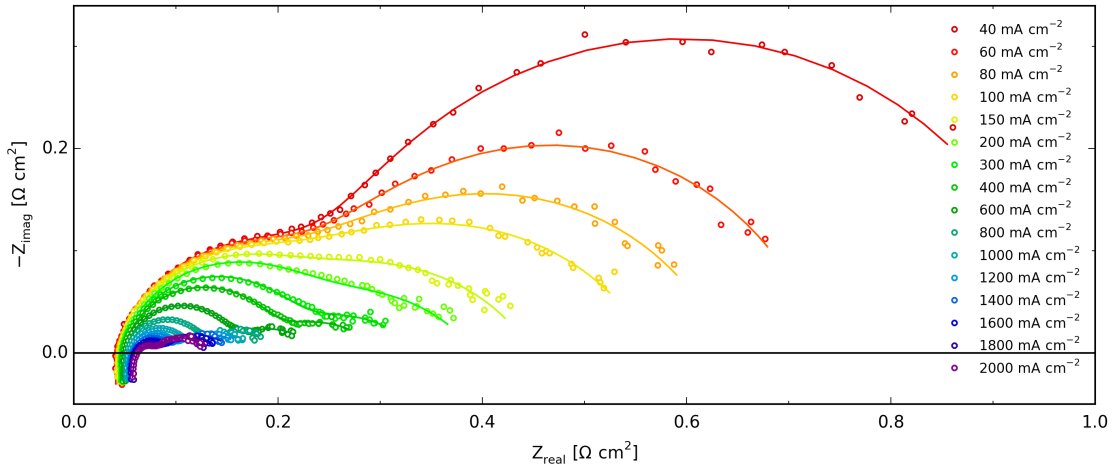

(b) R-NiMo(pp) | *m*-PBI | Ni(pp), 15 kHz-1 kHz.

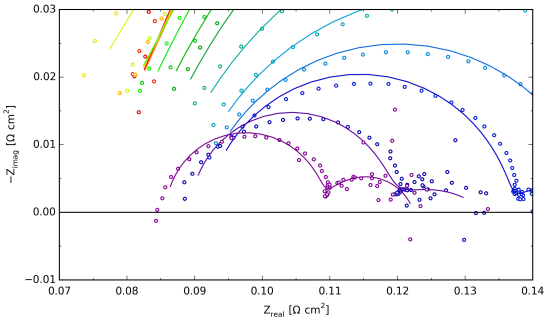

(c) Enlargement of **(a)**

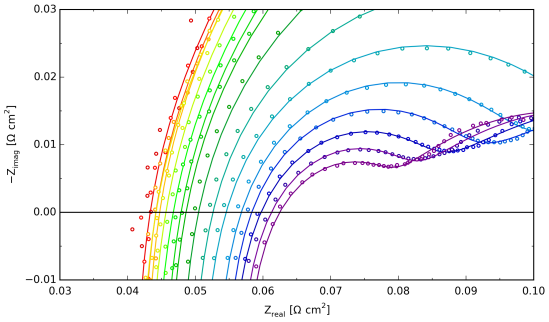

(d) Enlargment of **(b)**

Fig. 4.10: GEIS for 2 different cells at the full recorded current density range with an amplitude of 10% of the current density setpoint. For both cells the membrane is *m*-PBI, and the anode Ni(pp). Cathodes are **(a)** Nickel foam, and **(b)** Raney-nickel-molybdenum. **(c)** High frequency (HF) intercept region of (a), and **(d)** HF intercept region of (b). *m*-PBI thickness, d_{wet} = 40 µm, T = 80°C, [KOH] = 24 wt%, flowrate = 5 ml min^{-1} for foam (f) and 50 ml min^{-1} for perforated plate (pp), flowfield = pin(FZJ).

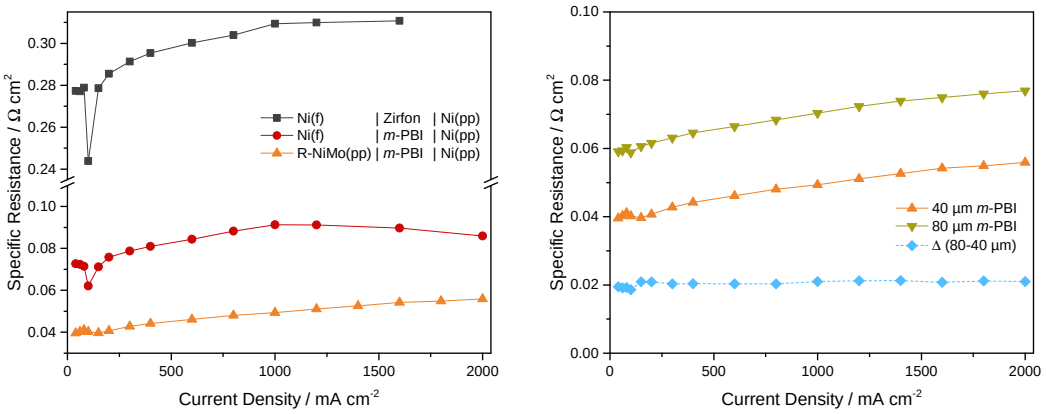

Fig. 4.11: R_s values obtained from equivalent circuit fitting. **(a)** Obtained values from different types of cells. **(b)** Identical cells with two different membrane thickness's.

the data presented here. Nonetheless, if we take the assumptions to be valid, we can evaluate the R_s increase associated by doubling the membrane thickness (40→80 µm) and estimate the membrane contribution as well as estimate the *in-situ* specific conductivity of the membrane. Figure 4.11b show data R_s for two cells with different membrane thickness, as well as the difference between the two. The difference caused by 40 µm membrane increase (♦) is about 20 mΩ cm^2, only half of that of the cell with a 40 µm membrane, and about $\sim 2/7$ of the cell where the cathode is Ni(f) instead of R-NiMo(pp). The corresponding specific conductivity of the membrane can on this basis be calculated to about 205 mS cm^{-1}, which fit quite well with measured values recorded *ex-situ*, see Figure 4.3. To put the magnitude of the R_s in perspective, a PEM cell with Nafion 115 can have R_s values in the range 100-125 mΩ cm^2.[254] Naturally, the membranes applied here are thinner than the PEM reference (Nafion 115 $\sim$ 150 µm), but ultimately the practically applicable thickness will be determined by other properties like durability, gas crossover-resistance, and practical robustness in terms of fabrication and assembly.

It is interesting to compare the values obtained by impedance to those that can be extracted from tafel fits using eq. (2.22). The area specific resistances for the Ni(f) | Zirfon | Ni(pp) cell can be fitted to 0.32 Ω cm^2, compared with 0.28 Ω cm^2 estimated by impedance. Similarly, for 40 µm *m*-PBI cells, we find 0.11 and 0.15 Ω cm^2 with Ni(f) and R-NiMo(pp) cathodes, compared with 0.07 and 0.04

with impedance. The agreement, or lack thereof, between the methods differ quite significantly, hence caution is necessary when using tafel fits to estimate R_s. Effects due to bubbles can appear ohmic (linear) even if they are not exclusively so. Likewise, is a distinguishing between ohmic resistance from the membrane and from the rest of the cell also important to have in mind, although that can be difficult to properly determine experimentally.

In a slight extension to the analysis we can approximate membrane and non-membrane ohmic contributions and compare them against the total polarization resistance recorded by impedance spectroscopy. Figure 4.12 displays the series resistance, polarization resistance, and total resistance measured by GEIS for two cells (4.12a and 4.12b), as well as the corresponding polarization data and the relative ohmic contributions from membrane/diaphragm and liquid electrolyte/electrode contributions (4.12c and 4.12d). The two cells are respectively a Ni(f) | Zirfon | Ni(pp) cell and a R-NiMo(pp) | *m*-PBI | Ni(pp) cell. The *m*-PBI membrane resistance was determined based on previous assumptions, and it is subtracted from the Ni(f)-cathode cell values to determine the electrode/electrolyte ohmic contribution in cells with Ni(f) cathodes. This is then used to estimate the part of the ohmic resistance which is caused by Zirfon. Some uncertainty must be expected this way. It is unfortunately not possible to separate the polarization part into cathode and anode based on the present data.

The two presented cells in Figure 4.12 vary on two parameters: The cathode, a Ni(f) versus a R-NiMo(pp); and separator, a thin *m*-PBI membrane versus a Zirfon diaphragm. Here two primary observations are made. In the classic-type cell with plain electrodes and a diaphragm, the ohmic contribution dominates from 300 mA cm^{-2}, whereas the ohmic contribution in the *m*-PBI based cell never exceed the polarization resistance in presented current density range. Furthermore, the ohmic part from the membrane is so low, that some performance could easily be compromised for better physical properties or improved durability. Secondly, the plain Ni(f) electrode shows lower polarization resistance at high current densities than the Raney-activated perforated plate.

This is peculiar, but is likely an effect of electrode geometry and gas blanketing. Figure 4.13 conceptually outlines how the electrodes are pressed against the membrane/diaphragm. The foam electrodes are more open, hence most of the active surfaces can readily get rid of produced gas. On the other hand, the perforated plates have larger flat surfaces towards the membrane, and hence the

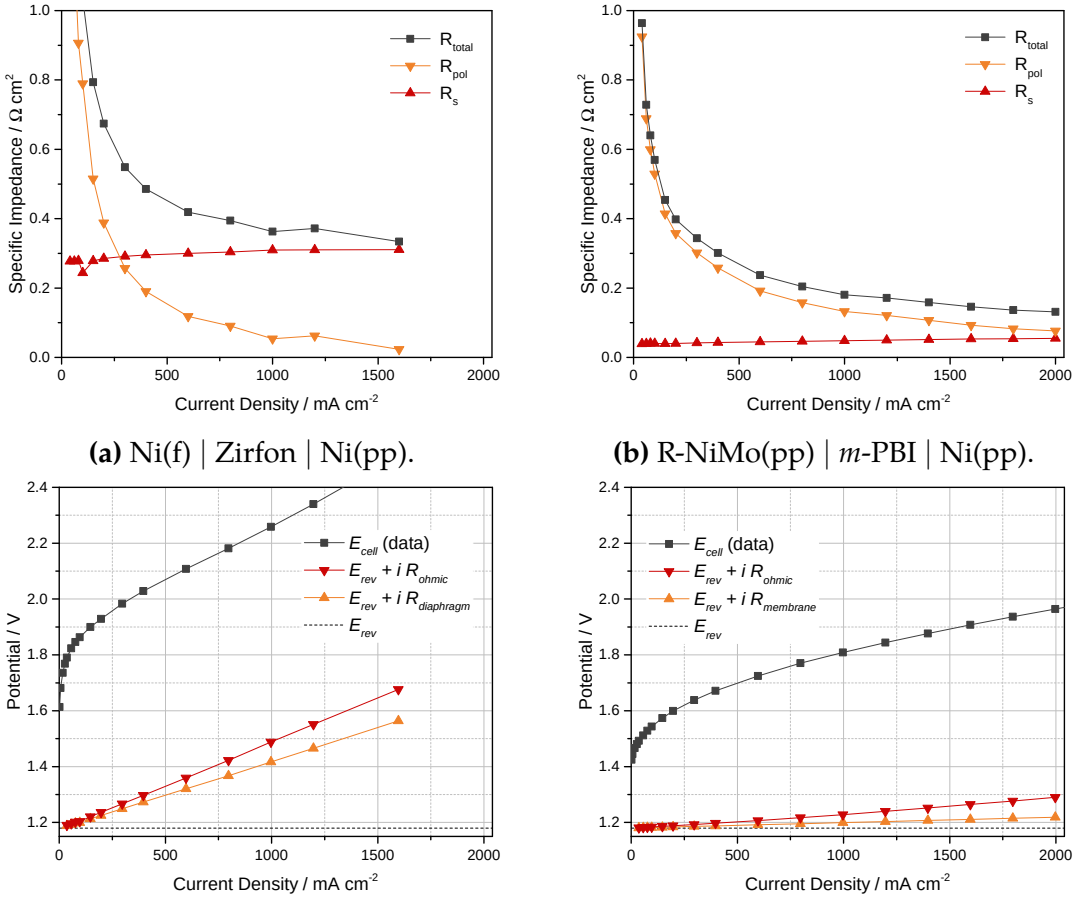

(a) Ni(f) | Zirfon | Ni(pp).

(b) R-NiMo(pp) | *m*-PBI | Ni(pp).

(c) Ni(f) | Zirfon | Ni(pp).

(d) R-NiMo(pp) | *m*-PBI | Ni(pp).

Fig. 4.12: Ohmic and polarization resistance contributions as function of current density for, **(a)** classic type cell with a Zirfon diaphragm and nickel cathode and, **(b)** a APEM type cell with 40 µm *m*-PBI membrane, and R-NiMo(pp) cathode. Corresponding polarization curves, with the respective total ohmic contributions and the part originating from the separator, plotted for **(c)** the classic type cell and, **(d)** the APEM cell. *m*-PBI thickness, d_{wet} = 40 µm, T = 80°C, [KOH] = 24 wt%, flowrate = 5 ml min^{-1} for foam (f) and 50 ml min^{-1} for perforated plate (pp), flowfield = pin(FZJ).

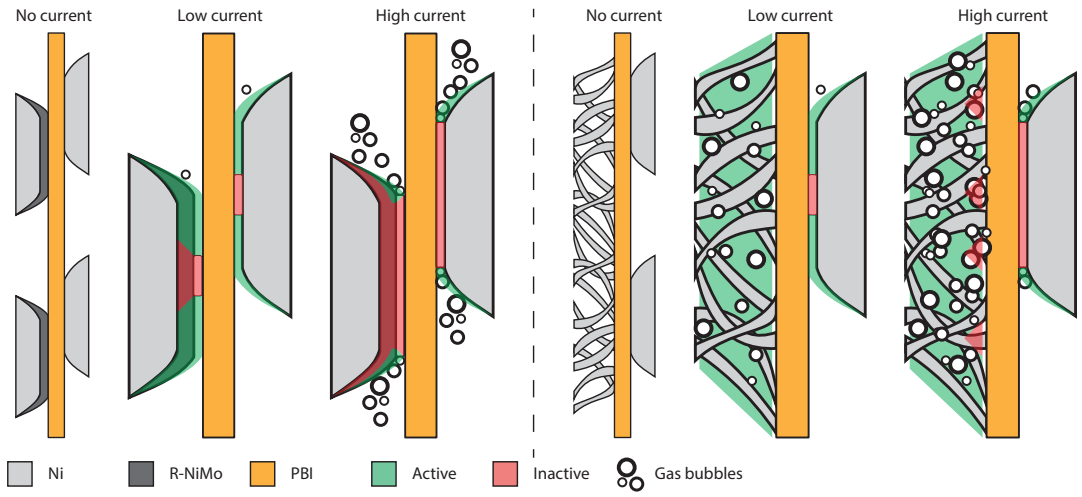

Fig. 4.13: Schematic illustration of the effects of increasing current density and increasing gas evolution. **(left)** A cell with a R-NiMo(pp) cathode. **(right)** A cell with a Ni(f) cathode. The foam geometry more easily discharge evolved gas, and a smaller fraction of the electrode deactivate.

Raney-coatings will more easily experience significant deactivation due to excessive gas bubble blocking. Whether the surface is blocked or if the pore structure is filled is not possible to determine based on the available data, but it seems reasonable to expect a decrease in effective surface area which is more severe for the perforated plate and Raney nickel type electrodes. Ultimately, this points towards the need for optimized electrode geometries. The Raney electrodes in question present a large nano and micro-porous structure with relatively small exhaust areas, i.e. the area facing away from the membrane along the circumference of the perforations in the plate. Ideally, the area and the dense volume of solid nickel parts on the back of the Raney electrodes should be minimized, so the evolved gas could more readily escape from the back side. A design like what is used in PEM EC and fuel cells with porous catalyst layer are likely significantly better when sufficiently optimized.

4.2.2 Durability and gas crossover

Characterization in terms of performance is the first parameter to evaluate when developing or applying new materials. Secondly, but no less important, is the robustness and durability of the system and materials. Here the crucial issue is the durability of the membrane and electrodes, and robustness in terms of mechani-

cal strength and capability to separate generated gasses. As was already shown, a certain degradation is expected from the membranes under classical conditions at 80°C and > 20 wt% KOH (aq), which will ultimately lead to mechanical weakening and membrane failure. However, the timeframe for cell failure was not closely investigated.

During the visit to FZJ a number of cells were run to assess durability and lifetime. The cells were operated dynamically by switching between 100 and 1000 mA cm^{-2} in day-night cycles, after an initial break-in period at 100 mA cm^{-2}, which commonly occurred over the weekend. Cells were of the type R-NiMo(pp) | *m*-PBI | Ni(pp). We expected stability issues from Raney-nickel anodes and since they were shown only to provide a marginal improvement, they were not applied. The H_2 in O_2 level was monitored after the anodic gas was dried by silica gel and molecular sieves. A total of four cells were run this way and the evolution in cell potential and the H_2 in O_2 values are plotted in Figure 4.14[I]. Cells **(a)** and **(b)** operate with 40 μm membranes, whereas **(c)** and **(d)** use thicker 80 μm membranes. For clarity, periods where polarization and impedance data where recorded are omitted.

The durability of electrolysis cells concern two aspects: Loss of performance and cell failure. Lifetime would be determined by a cut-off potential or by cell failure. The loss of performance is generally understood in electrochemical terms, which in electrolysis is an increase in cell potential at constant current. It could however, also be in terms of gradually increasing crossover values. Failure will occur when either a cut-off potential is reached, an electrode short circuit is experienced, or when gas-crossover values increase beyond a certain limit. In some types of electrolysis the cell potential may increase due to a loss of conductivity of the membrane, but we do not expect this to happen due to the presence of liquid electrolyte. Consequently, we do not expect increased cell potentials due to membrane degradation, but rather that the membrane after sufficient weakening will become incapable of separating electrodes and gasses. Hence, we ascribe the continuous potential degradation to be an electrode effect, but relate the cell failures with membrane degradation.

In Figure 4.14 cells **(a)** and **(b)** have thinnest membranes (40 μm *m*-PBI) and show the lowest lifetimes, and conversely **(c)** and **(d)** with double the membrane thickness show on average double the life time. Failure by short circuiting ex-

[I]More detailed H_2 in O_2 data exist for **(d)**, but is currently unavailable.

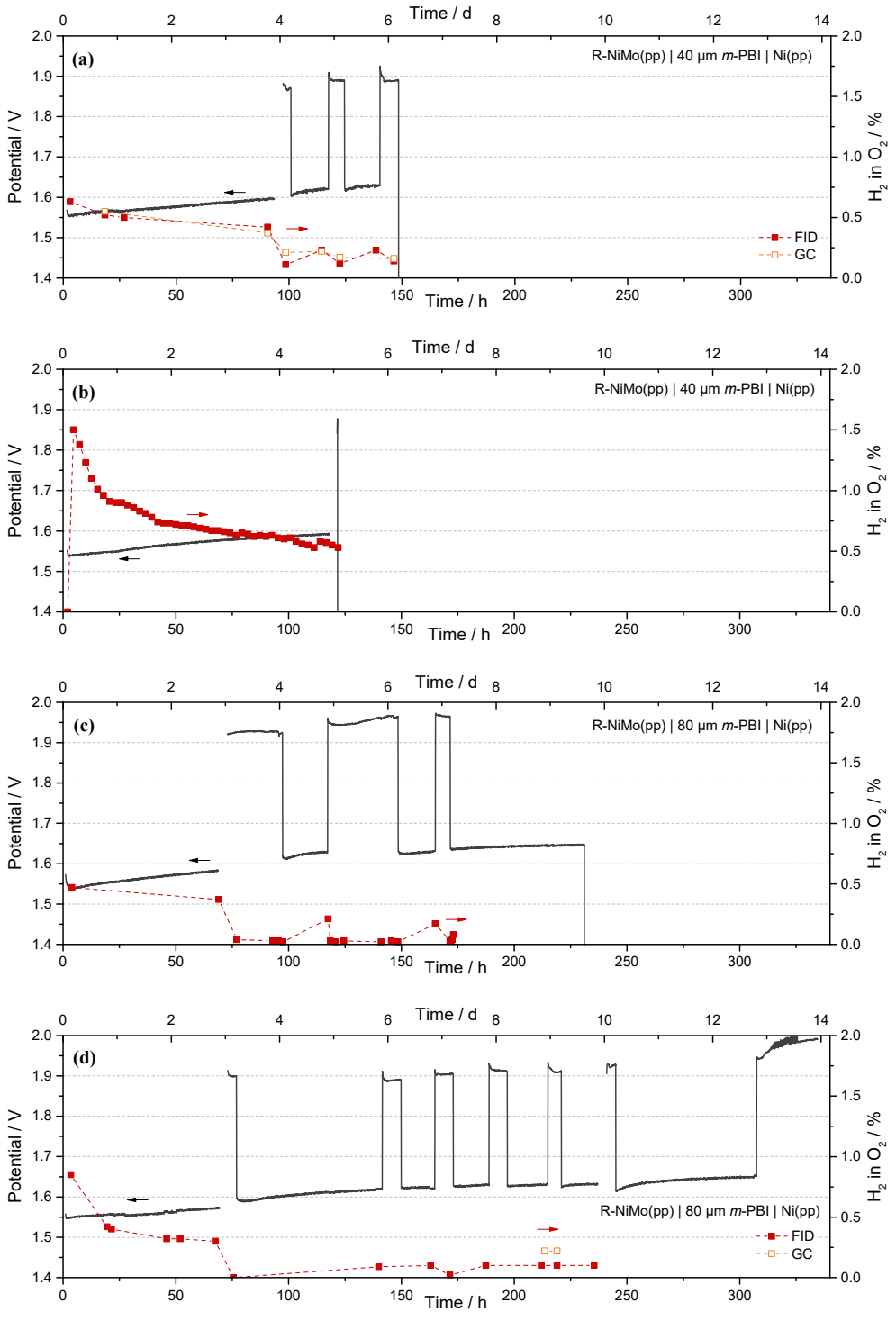

Fig. 4.14: Durability data for cells with alternating current density setpoints between 100 and 1000 mA cm^{-2}. The cell potential and H_2 in O_2 values were monitored. **(a)** and **(b)** cells with 40 µm membranes, **(c)** and **(d)** cells with 80 µm membranes. T = 80°C, [KOH] = 24 wt%, flowrate = 50 ml min^{-1}, flowfield = pin(FZJ).

perienced for the first two tested cells **(a)** and **(c)**, lead us to apply a sub-gasket around the membrane to prevent excessive mechanical compression. This may partially be the reason why cells **(b)** and **(d)** failed due to increased H_2 in O_2 levels rather than a short circuiting.

We very clearly learn that the membranes based on *m*-PBI are indeed are not stable under conditions similar to classical alkaline electrolysis at 80°C and 24 wt% KOH (aq). Figure 4.15 show the four membranes after cell disassembly and after submersion in water. The damage was visually less severe prior to contact with water.

One cell ran long enough enabling two polarization curves to be recorded with a week in-between. The curve and R_s values determined by GEIS are plotted in Figure 4.16. The difference in polarization characteristics are from the activation region, and the overall ohmic resistance of the cell is even observed to decrease. Most likely, the deactivation of electrodes is caused by a loss of material or surface area on the cathode, whereas the decrease in R_s is an effect of membrane thinning. Membrane degradation in the form of backbone scissoring leads to a loss of material, and consequently the membrane experience thinning due to the compression from the electrodes. Ultimately when enough polymer is lost from the membrane, holes form resulting in short circuiting or sudden rise in crossover.

Since the *m*-PBI membranes degrade it is not feasible to apply them under industrial electrolysis conditions. Hence, to improve cell life and stability different approaches can be followed including reduction of temperature or KOH concentration, increasing membrane thickness, or ideally the development of a more stable but equally conductive membrane.

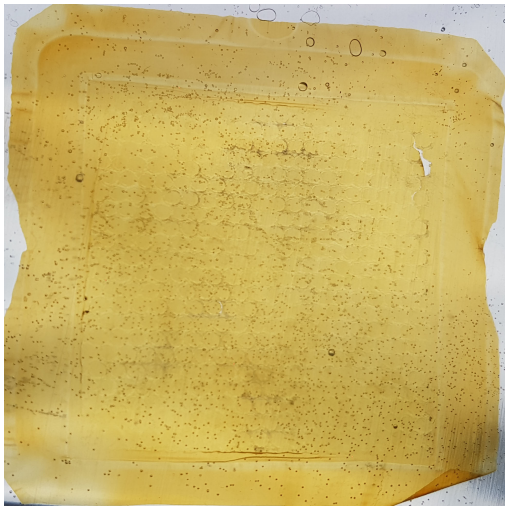

(a) 40 µm #1

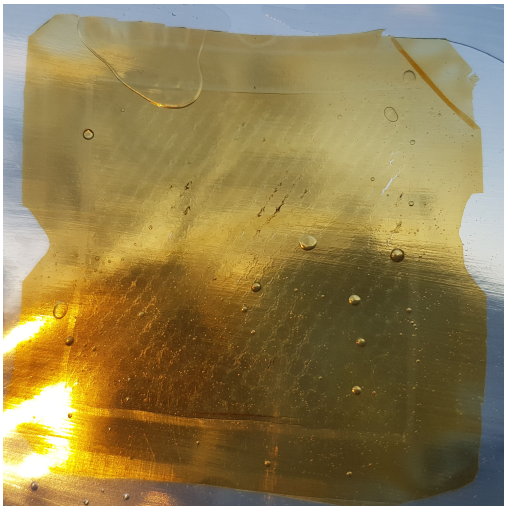

(b) 40 µm #2

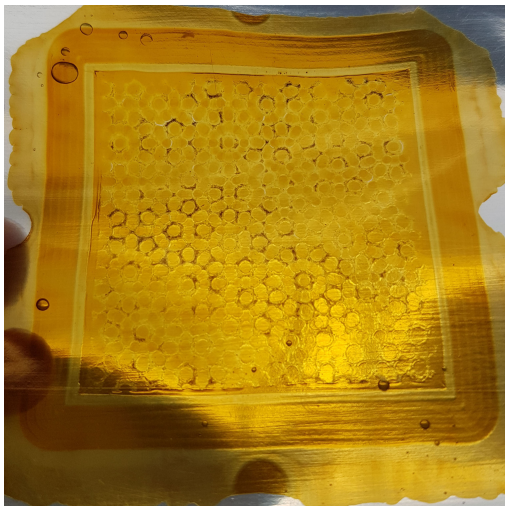

(c) 80 µm #1

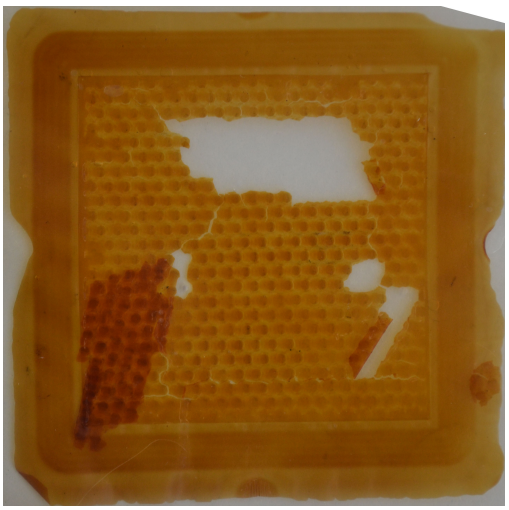

(d) 80 µm #2

Fig. 4.15: Post-morten images of the membranes after durability tests. Lifetimes were approximately: **(a)** 147 h, **(b)** 120 h, **(c)** 230 h, **(d)** 309 h.

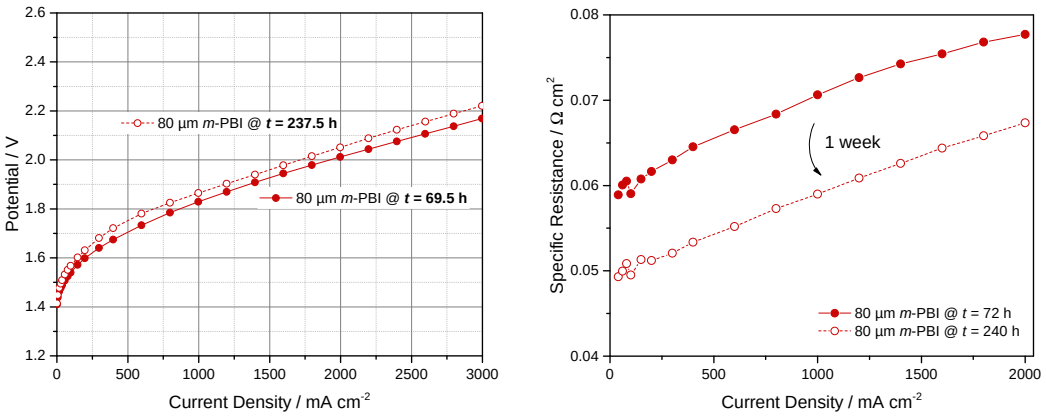

Fig. 4.16: Changes caused by 1 week of durability test for, **(a)** polarization behaviour and, **(b)** R_s values. 80 µm *m*-PBI membrane. T = 80°C, [KOH] = 24 wt%, flowrate = 50 ml min^{-1}, flowfield = pin(FZJ).

4.3 mes-PBI as stable electrolyte

At Simon Fraser University in Vancouver, Canada, the group of Steven Holdcroft are doing research on developing polybenzimidazole derived polymers with better alkaline stability. One such promising polymer is the poly(2,2′-(*m*-mesistylene)-5,5′-bibenzimidazole) (mes-PBI), which we have investigated as electrolyte for alkaline electrolysis. The polymer behave similarly to *m*-PBI and undergo deprotonization in alkaline solution, as shown in Figure 4.17

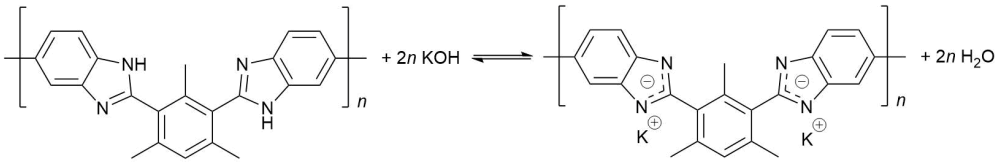

Fig. 4.17: Equilibrium scheme between the neutral pristine mes-PBI polymer and the potassium polybenzimidazolide.

The idea was to use steric hindrance to protect the weak C2 position, but strategies for improving polymer stability is beyond the scope of the current project. Rather, we received samples to characterize and evaluate for alkaline electrolysis.

The membranes swell upon equilibration, although less so than *m*-PBI. Membrane thickness was about 60-65 μm after equilibration in KOH (aq), and cells with 210 μm nickel foam electrodes were run at 5, 15 and 25 wt% KOH (aq). The polarization performance was compared with *m*-PBI and Zirfon and is presented in Figure 4.18. We observe a slightly lower performance than that of *m*-PBI, but also note that the membranes are about 50% thicker. Although the Zirfon cell operate at lower potentials at intermediate current density ($\sim$ 100-500 mA cm^{-2}) we find a lower slope of the cell with mes-PBI in 25 wt% indicating superior ohmic properties. If the curves in Figure 4.18 are compared against previously presented data in Figure 4.2, there are some discrepancy, which is likely caused by changes in flow field, the elimination of a major Fe-source in the system, as well as changes in testing protocol.

To probe the ohmic part in more detail, without having EIS data on our hands, we can fit the data to the tafel equation (2.22). Data points at $i < 5$ mA cm^{-2} were filtered. Previously, a large difference in R_s determined by impedance and by tafel fits was observed, but with this in mind, one can still compare across fitted

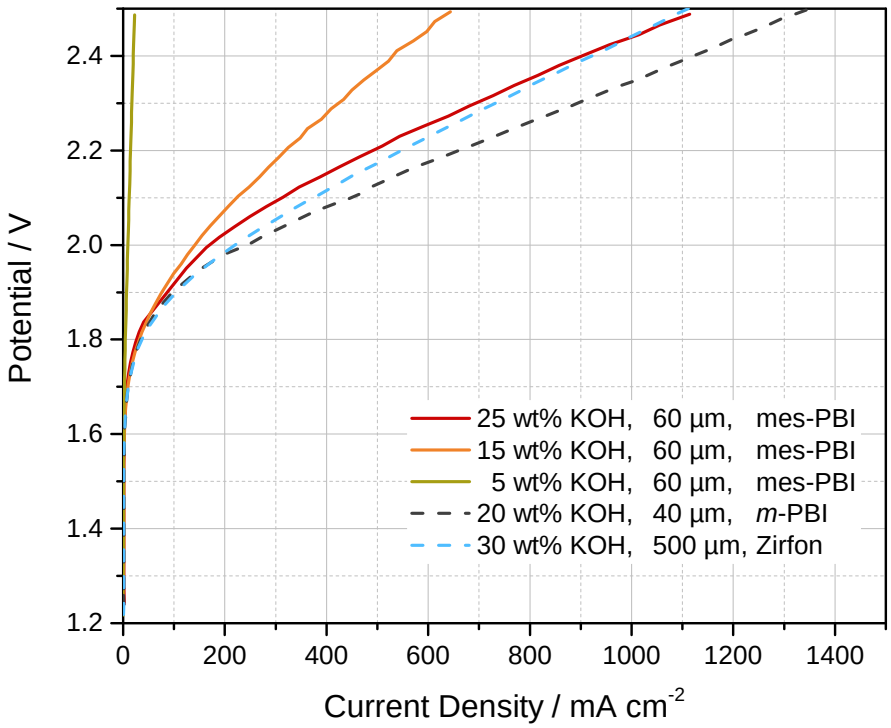

Fig. 4.18: Polarization behaviour of cells with mes-PBI membranes equilibrated at different KOH (aq) concentrations, and corresponding electrolyte. Similar data for cells *m*-PBI and Zirfon is shown for reference. Electrodes were 210 µm nickel foam. mes-PBI thickness, d_{wet} = 60-65 µm, T = 80°C, flowrate = 120 ml min^{-1}, flowfield = pin.

values. Looking at the curves of primary interest, i.e. mes-PBI in 25 wt% in comparison to the reference curves, we find values of 0.366 Ω cm^2 for mes-PBI, 0.335 Ω cm^2 for *m*-PBI, and 0.435 Ω cm^2 for Zirfon. Notably, both PBI membranes have lower resistance than the diaphragm. The fitted resistance values correspond to equivalent specific conductivities of 16 mS cm^{-1} for mes-PBI, 12 mS cm^{-1} for *m*-PBI and 115 mS cm^{-1} for Zirfon using estimated membrane/diaphragm thicknesses of 60, 40 and 500 µm for mes-PBI, *m*-PBI, and Zirfon respectively. It must be stated that there is quite a significant uncertainty, and the all values are vastly underestimated by this method. What is interesting is mostly that mes-PBI and *m*-PBI appear similar, and show better ohmic performance than Zirfon.

The mes-PBI membrane conductivity was also investigated in the *ex-situ* conductivity cell and the data are presented in Figure 4.19. Values for *m*-PBI are plotted for comparison. We note that the directly measured through-plane conductivity of *m*-PBI is almost an order of magnitude higher, 87 mS cm^{-1} versus

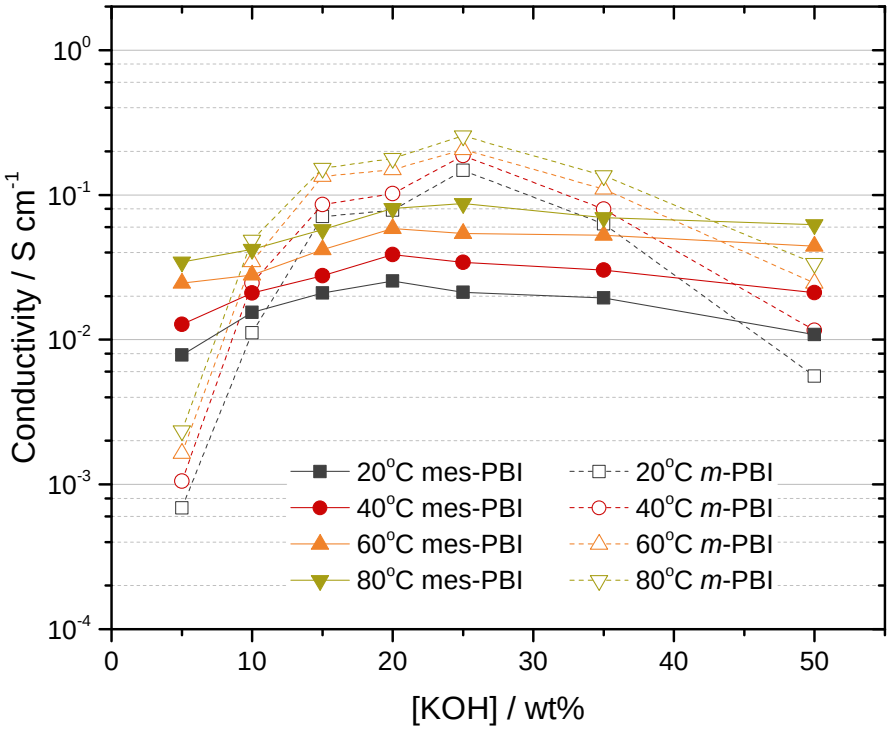

Fig. 4.19: Specific conductivity of mes-PBI with *m*-PBI as reference data. Recorded by AC-impedance in a dedicated conductivity cell.

16 mS cm^{-1} for mes-PBI at T = 80°C. Interestingly, we observe lower peak conductivity, perhaps caused by a different swelling behaviour,[250] but higher conductivity at low concentrations. This, however, does not present itself in any significantly improved cell performance in 5 wt% KOH, as compared with *m*-PBI.

The next question that pose itself is whether the mes-PBI actually is more stable than *m*-PBI. The detailed chemical analysis is published elsewhere.[250] In short it appears that mes-PBI is more chemically stable in the low KOH concentration range up to 10 wt%, but suffer from similar degradation issues as *m*-PBI when the concentration is higher. This is likely because the potassium polybenzimidazolide form of the polymer slightly alter the orientation of the protecting methyl groups, hence the steric protection is lost. A more elaborate study on the electrochemical and electrolysis operation effects on mes-PBI membrane stability is yet to be undertaken.

5

Results on active electrodes

Besides the work carried out evaluating PBI membranes as electrolyte, some work were also dedicated to developing and preparing efficient electrodes for both the cathodic hydrogen evolution and the anodic oxygen evolution. This chapter cover in varying detail the work carried out during the project in this regard.

5.1 Nickel-Iron anodes

There has been a shift in focus in recent literature from metal oxides towards (oxy)hydroxides, phosphides, sulfides and selenides. The (oxy)hydroxides have for a few years now recieved significant attention, to a large degree because of the high activity of nickel-iron (oxy)hydroxides. Some general trends, and selected performances were presented in the literature review in Section 2.3.2. Here some aspects will be discussed in more detail, and the work that has concerned these materials is presented.

5.1.1 Preparation

The nickel-iron (oxy)hydroxides, generically refered to as NiFe-hydroxides, as well as other metal-hydroxides, are primarily prepared in either of two ways:

By an electrodeposition process[162,167,195] or through a homogeneous hydrothermal chemical precipitation route.[77,82,159,163,198] In practice the methods are different, but conceptually very similar processes take place. A third and conceptually identical route, is chemical precipitation by mixing alkaline solution and a metal-ion containing solution. That approachs appear to be less widely applied, likely because it form larger and less well defined precipitates, and it does not apply the material directly on an electrode. The review by Dionigi[140] also address synthesis routes.

Electrodeposition

Although the electrodeposition of metal hydroxide and (oxy)hydroxide proceed through electrochemical reactions on an electrode surface, it is not the conventional electroreduction of metallic ions to their solid form that takes place. Rather, an induced chemical precipitation takes place. Mostly this is done cathodically by reducing nitrate anions, although anodic deposition has also been reported.[196] Metal-hydroxides generally form in solutions with metal ions when pH is increased and display very low solubility in water. Hence, increasing pH is used to precipitate metal-(oxy)hydroxides. In the case of electrodeposited metal-hydroxides, metal-nitrate salts are used and the pH is increased locally at the electrode surface by the reduction of nitrate:[167,196]

$$NO_3{}^- + H_2O + 2\,e^- \longrightarrow NO_2{}^- + 2\,OH^- \tag{5.1}$$

$$M^{2+} + 2\,OH^- \longrightarrow M(OH)_2\,(s) \tag{5.2}$$

The process leads to a plate-like morphology, as the layered (oxy)hydroxides grow anisotropically.

Hydro-thermal precipitation

The hydrothermal synthesis, or homogeneous precipitation synthesis, utilizes the same concept of increasing pH and inducing chemical precipitation. The pH increase is achieved by decomposing suitable organic compounds, most commonly urea. At temperatures above 60°C urea start to hydrolyse,[184] and a num-

ber of proceeding reactions may follow,[197,255]

$$CO(NH_2)_2 + H_2O \longrightarrow 2\,NH_3 + CO_2\uparrow \tag{5.3}$$

$$NH_3 + H_2O \longrightarrow NH_4{}^+ + OH^- \tag{5.4}$$

$$Ni^{2+} + 2\,OH^- \longrightarrow Ni(OH)_2\downarrow \tag{5.5}$$

The metal-hydroxides then preferentially precipitate on a support, but can nucleate to form particulate material as well. In some publications additives beyond urea and metal-salts are used, e.g. NH_4F which has been shown to improve adhesion on glassy substrates and is proposed to help directional growth.[256]

Post treatment

In addition to preparing (oxy)hydroxides as electrode material, the anisotropic growth of the hydroxides have also been used as a template to form other derived materials. Several phosphides, sulfides, and selenides can be prepared while maintaining the morphology of the parent material, although these approaches have not been investigated in this project.

This work

A number of electrodes were prepared using the hydrothermal method following a procedure inspired by Lu *et al*.[163] Briefly, $Ni(NO_3)_2 \cdot 6\,H_2O$, $Fe(NO_3)_3 \cdot 9\,H_2O$, and $CO(NH_2)_2$ were dissolved in water. The solution and a piece of nickel foam were then placed in PTFE lined autoclave and heated to 120°C for 12 h. Electrodes were prepared from solutions with varying Ni:Fe ratios, while maintaining a constant total metal-ion concentration. The Ni:Fe solution molar-ratios investigated were; pure Ni (denoted 10:0), 9:1, 8:2, 7:3, 6:4, and 5:5, and electrodes samples are in the following text and figures denoted as such.

5.1.2 Physical characterization

No rigorous characterization was undertaken, but the prepared electrodes were examined with SEM and EDX. Representative micrographs are presented in Figure 5.1, for the 10:0-sample 5.1a, 5.1c, and 5.1e, and for the 5:5-sample 5.1b, 5.1d, and 5.1f. In both cases the morphology is plate-like due to the anisotropic

growth of the formed hydroxides. The plate-like morphology with a predominantly vertical orientation is achieved since vertically-oriented plates grow faster outward than horizontally oriented. As the horizontally grown plates connect with the vertically oriented they stop growing as they are effectively blocked. Hence, this type morphology with a preferential orientation is achieved. This provides quite a significant enhancement of the effective surface area, which is why it is used in some publications as a templating tool for other materials.[77,153,166,203] Furthermore, it appears that the sample without iron gave larger plate-sizes, but it is unclear why. Lastly, bundles of what appear as agglomerated, and perhaps weakly connected material is observed in either samples. The hydroxides generally display relatively low electronic conductivity and some show semiconductor behaviour,[193,194] hence material far from the underlying nickel support may show some degree of charging and appear brighter in the micrographs.

EDX was performed on regions with excessive material present to avoid or limit the response from the underlying nickel support. Nonetheless, there is a degree of uncertainty associated with the nickel-iron ratios presented in Table 5.1. To the extent that the values can be trusted qualitatively, there appears to be a preferential deposition of nickel over iron. This match with EDX performed on residual material floating on the surface after a 5:5 synthesis, which revealed a Ni:Fe molar ratio of 36:64. It can be speculated that insoluble Fe-oxides are formed as well, and some publications use various chelating agents to prevent this. However, the residual material was not investigated any further.

Table 5.1: EDX results for the prepared electrodes. Only the relative Ni and Fe fractions are considered.

Solution	Ni:Fe [mol%]	50:50	60:40	70:30	80:20	90:10	100:0
EDX est.	Ni:Fe [mol%]	66:34	74:26	76:24	86:14	89:11	-

The combined picture from SEM and EDX seems to indicate that the deposition produces coatings with varying degree of uniformity. Nonetheless, we do observe the expected plate-like growth with Ni and Fe from which enlarged surface area and increased catalytic activity towards the OER can be expected.

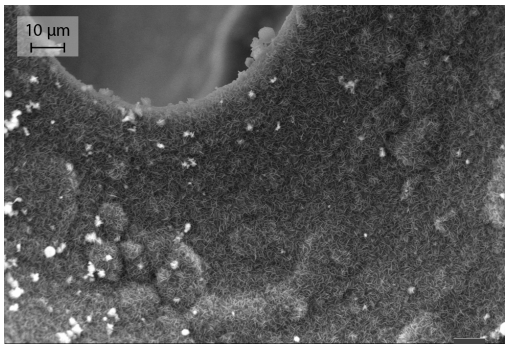

(a) 10:0 at ×2000 mag.

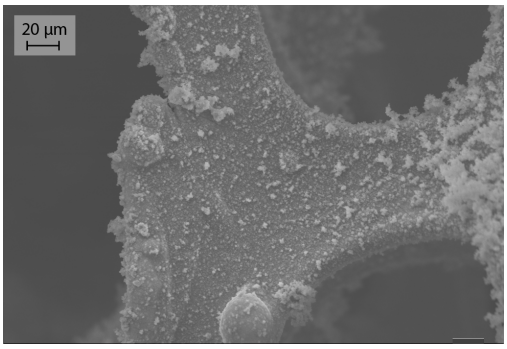

(b) 5:5 at ×1000 mag.

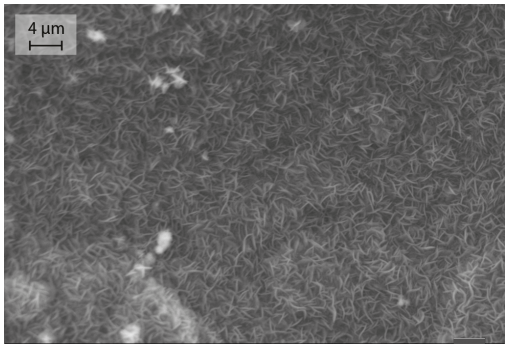

(c) 10:0 at ×5000 mag.

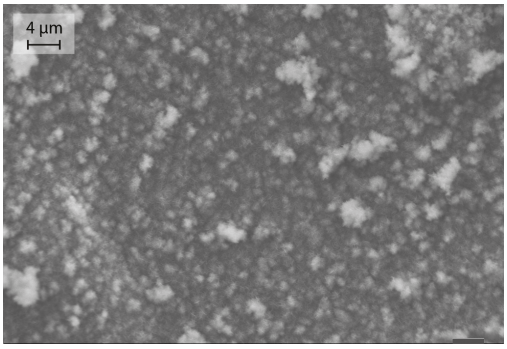

(d) 5:5 at ×5000 mag.

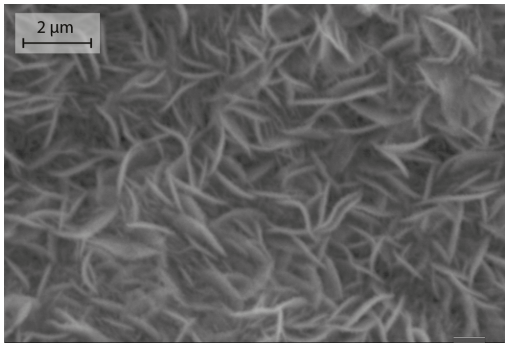

(e) 10:0 at ×20000 mag.

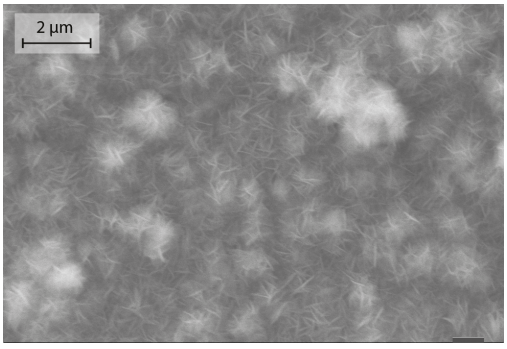

(f) 5:5 at ×20000 mag.

Fig. 5.1: Secondary electron SEM micrographs of prepared electrodes at different magnification. **(a)**, **(c)** and **(e)** without Fe (10:0), and **(b)**, **(d)** and **(f)** with Fe (5:5).

XRD

A single 5:5 electrode was examined with XRD. The diffractogram is presented in Figure 5.2 with relevant phase-indicators shown. A large background signal from pure nickel is present due to the nickel foam substrate. The remaining peaks match with the hydrotalcite structre. α-$Ni(OH)_2$ and Ni-Fe LDH materials are isostructural with hydrotalcite, whereas β-$Ni(OH)_2$ (theophrastite) is isostructural with brucite, which does not seem to be present. Hence, it seems that the deposited material is of the Ni-Fe-LDH type. No other phases appear to be present in any detectable amount. The interlayer peaks of the hydrotalcite structre at $2\theta = 12^\circ$ (003), and 23° (006) are strongly dependent on the intercalated anion. Here, the peak spacing matches with CO_3^{2-}-anions.[198] Nickel-hydrotalcite sturctures are known to have the highest anion affinity towards CO_3^{2-},[182] and we expect CO_3^{2-} to be present from the synthesis due to the hydrolysis of urea to CO_2. We note that on basis of the available data, or lack thereof, it cannot be determined if the 10:0-sample has formed the α or β phase of $Ni(OH)_2$. Other samples, prepared by chemical precipitation did however show a β-$Ni(OH)_2$ phase for the Fe-free batch, whereas the Fe-containing sample had a very clear hydrotalcite structure.

In the literature it has been discussed if α-$Ni(OH)_2$ or β-$Ni(OH)_2$ is the most active towards OER, and it has been suggested that an improved activity achieved by aging was due to the conversion from α to β-phase.[57] Recently it has been suggested that the observed effects were caused by iron inclusion, as well as either phases being in a higher oxidation state during actual oxygen evolution, i.e. γ-NiOOH and β-NiOOH. There is no consensus in the matter regarding the activity of the α versus the β-phase, but it is interesting to note that Fe^{3+} doping is incompatible with the β-$Ni(OH)_2$ structure. α-$Ni(OH)_2$ is known to age and transform into β-$Ni(OH)_2$, but with iron the α-$Ni(OH)_2$ structure is stabilized. Likewise, the active sites in mixed Ni-Fe-LDH catalysts are debated, but literature seems to lean towards Fe being the active site. There are even indications that Fe-hydroxides could be active, if not for lack of stability and poor electronic conductivity. In this view, the Ni-hydroxide structure helps stabilize the active Fe-sites, rather than the Fe atoms modifying the local environment around Ni atoms. On this basis, it should be optimal to include as much Fe as possible without inducing phase-separation. Depending on preparation technique this is likely in the region 25-33 mol%.[140,148]

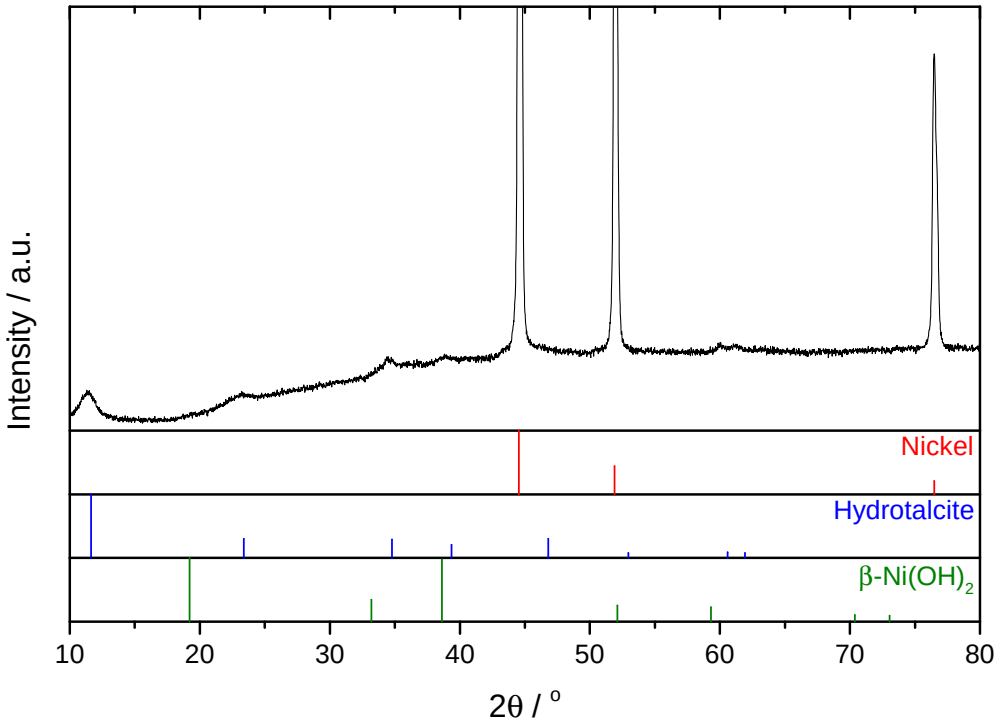

Fig. 5.2: XRD diffractogram of the as-prepared 5:5 electrode. Only the LDH structure (hydrotalcite) appear to be present, besides the background nickel signal from the nickel foam support.

5.1.3 Electrochemical performance

From the prepared $39 \times 80\,\mathrm{mm}^2$ sheets, electrodes were cut for half cell tests, and for full single cell tests. Half cells were evaluated at room temperature, whereas single cell tests were under conventional conditions at 80°C.

Half cells

Investigating the OER can be challenging, since some materials - in particular NiO_xH_y-materials - exhibit changes in phase and redox state at OER-relevant potentials, and display potential-dependent electronic properties.[257] Doped Ni-hydroxides such as the herein investigated Ni-Fe-hydroxides suffer from the same challenges, which are further complicated by the presence of iron, which cause a shift in the Ni^{2+}/Ni^{3+} redox potential. Figure 5.3 shows the electrode polarization of the *iR*-corrected data and the corresponding tafel plot. Although data were recorded up to 2000 mA cm^{-2}, noise caused by bubbles severely dis-

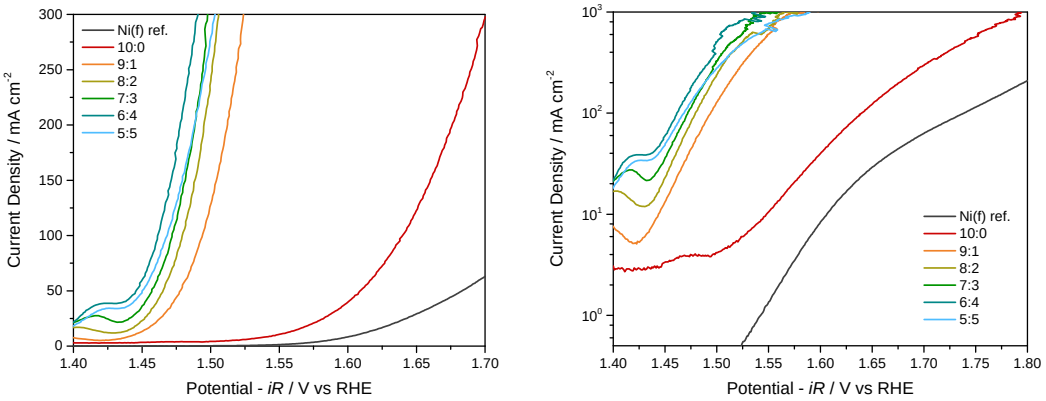

Fig. 5.3: Electrode polarization of NiFe-(oxy)hydroxide electrodes presented as, **(a)** normal iV-plot and, **(b)** tafel plot. T = RT, [KOH] = 20 wt%.

tort the polarization characteristics above anywhere between 300-1000 mA cm^{-2} depending on measurement, hence iR-corrected data are shown only up to 300 mA cm^{-2}. The data for the prepared electrodes are recorded by a forward scan (1.2 V to 2.5 V at 2 mV/s before iR-correction), whereas the nickel foam reference Ni(f) showed a large hysteresis, hence those values are the average of a forward and backward scan. iR-correction was done by estimating R_s at 1.23 V with potentiostatic impedance spectroscopy just prior to recording the polarization curve.

It is clear that at room temperature the presence of iron results in a significant enhancement relative to plain nickel materials. The apparent behaviour indicate an increased performance up to 40 wt% iron in precursor solution, which by EDX were determined to be roughly 25 mol% Fe in the electrode. The electrode with the highest Fe content show a similar high activity, but appears to have a slightly lower tafel slope, although the reason for this is unclear and may be an effect of the experimental details, rather than a conceptual difference. When the Fe content exceeds the solid solubility limit of the nickel-host structure it can be expected to locally form separated FeO_xH_y phases, which are less active than the mixed Ni-Fe phase. As such, over-doping the material result in regions of surface area which are less active, and the overall activity will thus decrease due to smaller effective surface area of the active part of the catalyst. In that sense, the measured performance match quite well with what can be expected. It should be noted that pristine nickel foam tend to activate upon potential cycling, and it

can probably be expected to reach activity similar to the 10:0-sample with sufficient cycling. Additionally, the R_s was seen to depend on the potential at which the impedance was recorded, and R_s was observed to decrease with increasing potentials (0.85 V over 1.23 V to 1.53 V).

For all electrodes, a visual colour transition from grey (Ni) or redish-yellow (with Fe) to black was observed, just prior to the gas evolution onset. This change in color is associated with the Ni^{2+}/Ni^{3+} redox shift and the corresponding structural changes. As nickel increases oxidation state, the material changes to maintain charge balance. This is in part achieved by intercalating anions or producing hydrogen defects. A neat feature of nickel materials, is that the $Ni^{2+/3+}$ peak can be used as a first order approximation of the electrochemically active surface area. Note that this does not necessarily relate directly to the active oxygen evolution surface area if Fe-sites are the active sites, and that nickel show a certain bulk activity in terms of the specific redox shift, but it can be used as an approximation. Cyclic voltametry scans in the region of the Ni^{2+}/Ni^{3+} peak for the different electrodes are shown in Figure 5.4a and the peak-shift variations due to scan rate are shown in Figure 5.4b for the 7:3-sample. The variance across electrodes in terms of peak position and shape strongly indicate poor uniformity of the coating compositions. The observed shift in the $Ni^{2+/3+}$-peak towards higher potentials with increasing Fe content is well known, but the bimodal nature of most peaks indicate regions with low Fe-content as well as high Fe-contents.

Table 5.2 shows the values of the integrated redox peaks of the samples. The cathodic peak is used since the anodic peak is partially obscured by the onset of OER. It would be too much of a stretch to attempt to calculate an absolute surface area on basis of this relatively crude dataset, but a comparison against a pristine nickel electrode and between the different samples is in place. Firstly, we observe an $\sim$20-40-fold increase in redox active nickel compared to a pristine nickel foam sample, showcasing the surface-area benefit by applying this type of coating. Note that the redox peak of pristine nickel will grow on cycling, and the presented value is from an early cycle. Secondly there seem to be a correlation between the electrode activity and amount of redox active nickel. Both the activity and the redox-peak area increase with increasing Fe-contents until the 6:4 sample.

Interestingly, commercial *Inconel 625* and *NiFeCrAl* foams (Alantum) showed

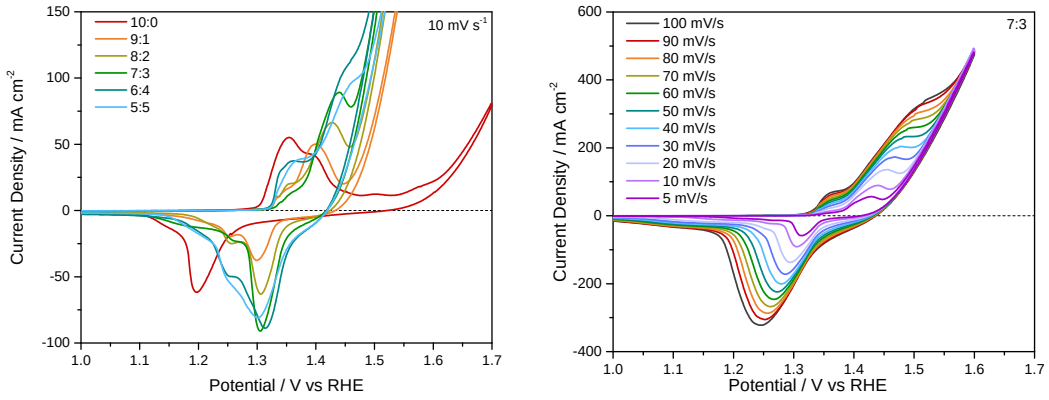

(a) **(b)**

Fig. 5.4: Cyclic voltammetry of the prepared electrodes. **(a)** Fixed scanrate of 10 mV s^{-1} for different electrodes and, **(b)** Varying scanrate for the 7:3-sample. Scans from 0.5 to 1.6 V vs RHE (1.7 V for the 10:0 sample). T = RT, [KOH] = 20 wt%.

Table 5.2: Integrated values of the $Ni^{2+/3+}$ cathodic redox peak area for the different electrodes.

Sample		5:5	6:4	7:3	8:2	9:1	10:0	Ni(f) ref.
Cathodic peak	[mC]	945	968	705	486	351	585	21

almost equal OER activity, albeit with significant initial corrosion. This was not investigated further but a distinct color change of the electrolyte was noticed. Likely, some elements selectively dissolve, and the remaining Ni and Fe form (oxy)hydroxide upon OER polarization.

Single cell electrolysis

The electrodes prepared were also applied in single cell electrolysis as anodes with a *m*-PBI membrane (35-40 µm) and a nickel foam cathode. Figure 5.5 show the cell performance at room temperature and at 80°C. The 6:4-cell is omitted since the cell suffered from massive noise and a variety of issues for unknown reasons.

An interesting thing to observe is that the significant differences between anodes with varying degree of Fe-content is to some extent washed out at elevated temperatures. Particular in the light, that most electrode publications in recent literature only concern themselves with 1 M KOH (aq) at room temperature,

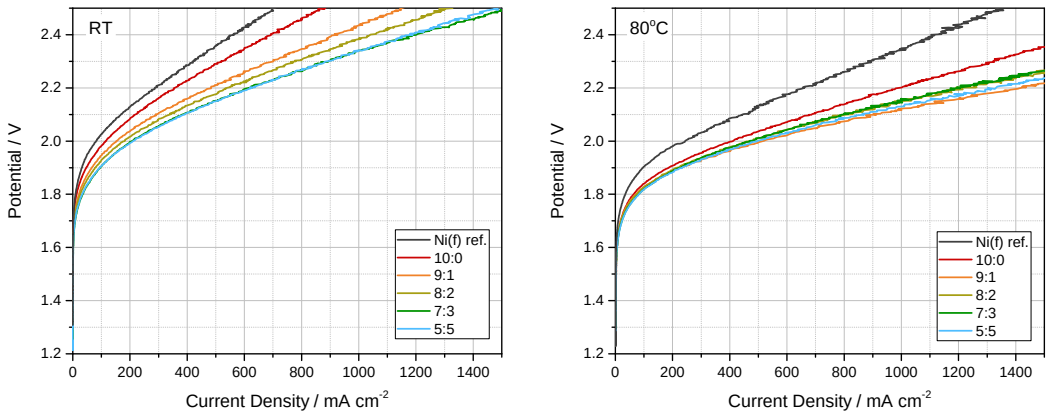

(a) **(b)**

Fig. 5.5: Single cell polarization curves using the prepared NiFe electrodes as anode, with a *m*-PBI membrane, and nickel foam cathode. Both cathode and anodes were pressed to 210 µm. **(a)** at room temperature, **(b)** at 80°C. *m*-PBI thickness, d_{wet} = 35-40 µm, [KOH] = 20 wt%, flowrate = 120 ml min^{-1}, flowfield = pin.

whereas the test in the present work were carried out under 20 wt% KOH (aq) and up to 80°C. Furthermore, there seem to be no significant activation benefit between the Fe-containing electrodes and the one without (10:0) whereas the slopes are different.

The anodes were not investigated in terms of stability.

5.1.4 Incidental iron

As already mentioned, iron present in the electrolyte has the capacity to improve the activity of nickel electrodes. This is a problem in terms of confidently evaluating electrodes, although it provide conveniently active and simple electrodes. In the aspect of this study, iron has been present from two sources. As an impurity in the KOH pellets used to prepare the liquid electrolyte ($\leq$ 5 mg/kg) and from steel components in contact with the hot liquid electrolyte. At early stages two small pieces of steel tube were part of the tubing, which were later removed. Similarly, a set of ball-valves were conventional steel-type, and the pumps used in most of the projects also had steel exposed to the electrolyte. Examples of this significant activation is shown in Figure 5.6 in a case with both *m*-PBI and mes-PBI membranes.

The iron activation is not an immediate effect and the activation is to some

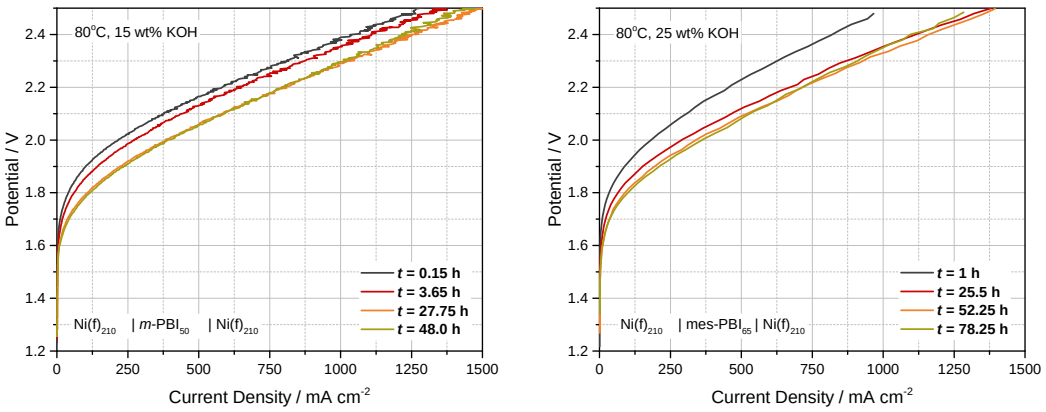

Fig. 5.6: Development in polarization curves over time with steel components exposed to the electrolyte, cell examples used for studies with **(a)** *m*-PBI at 15 wt% KOH (aq) and, **(b)** mes-PBI at 25 wt% KOH (aq). Electrode and membrane thickness are labelled as indices. $T = 80°C$, flowrate = 120 ml min^{-1}, flowfield (a) = linear, (b) = pin.

extent combined with the phase changes of nickel at high potentials. The impurities solely from the electrolyte may only activate the anode partially and not provide the same degree of activation as larger amounts of Fe-ions will. However, when a iron source is available, the anodes will readily activate over the course of 1-2 days. Examples of cells measured after eliminating Fe-sources are shown in Figure 5.7, albeit these cells were only run for a single day. It appears at the very least, that *in-situ* activation is eliminated, although a thorough systematic investigation has not been performed.

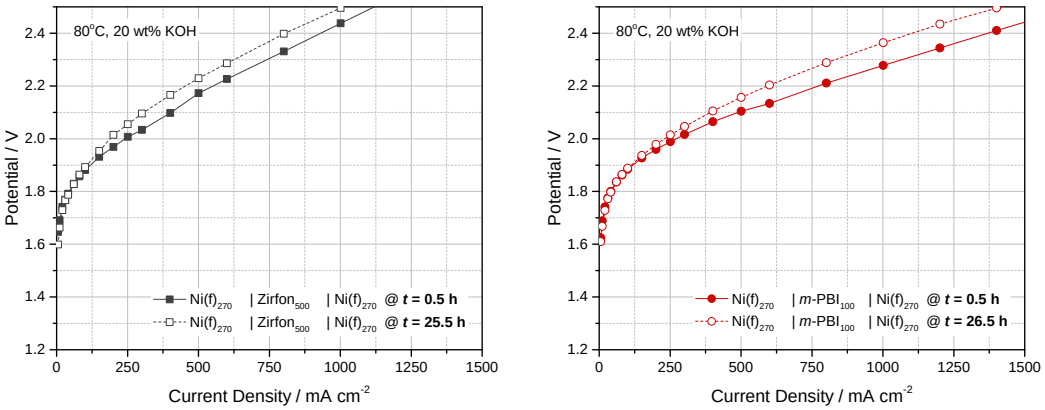

(a) **(b)**

Fig. 5.7: Development in polarization curves over time without steel components exposed to the electrolyte. Cells presented with **(a)** Zirfon and, **(b)** *m*-PBI. Electrode and membrane thickness are labelled as indices. $T = 80°C$, [KOH] = 20 wt%, flowrate = 60 ml min^{-1}, flowfield = pin.

5.2 Nickel based cathodes

Platinum catalyse the hydrogen evolution very efficiently in both acidic and alkaline environment. In the acidic environment research still struggle to find competitive materials. However, under alkaline conditions, a number of catalysts based on non-noble metals have been published with activities seemingly on par with platinum.[66,72–74,79,109] This project have preliminarily investigated some of these materials. Raney-nickel based electrodes were investigated in single cell tests in Section 4.2, and measurements on electrodes prepared with NiMo, NiSn, and NiCoS coatings are presented in this section.

NiMo and NiSn electrodes were prepared in-house, whereas NiCoS-electrodes were supplied by partners based on work described in [118, 119] and will only be used for comparison.

5.2.1 NiSn cathodes

The work carried out on nickel-tin based electrodes were a collaboration with bachelor student Anders Richter Kjeldsen during work on his bachelor project ultimo 2015. Anders carried out the majority of the experimental work. The project was excecuted in two segments, an initial batch of electrodes inspired by a paper from Zhu,[88] followed by a parametric study with slightly different preparation conditions. The idea was to apply nickel-tin coatings to nickel foam by electrodeposition and to evaluate the resulting electrodes and the preparation procedure.

Initially electrodes were prepared potentiostatically, without any pre-treatment of the substrate. Representative half-cell polarization curves in 30 wt% KOH are presented in Figure 5.8. The electrodes display very good performance and behave similarly to the literature starting point as would be expected, although galvanostatic operation at 300 mA cm^{-2} for 10 h following the polarization measurements revealed a loss of performance with a constant decrease in potential.

The electrodes were investigated with top-down and ion-milled cross-section SEM. Representative micrographs are presented in Figure 5.9 obtained with a backscatter detector. The SEM showed a cauliflower morphology of the deposited coating, but more critically revealed some serious problems with ad-

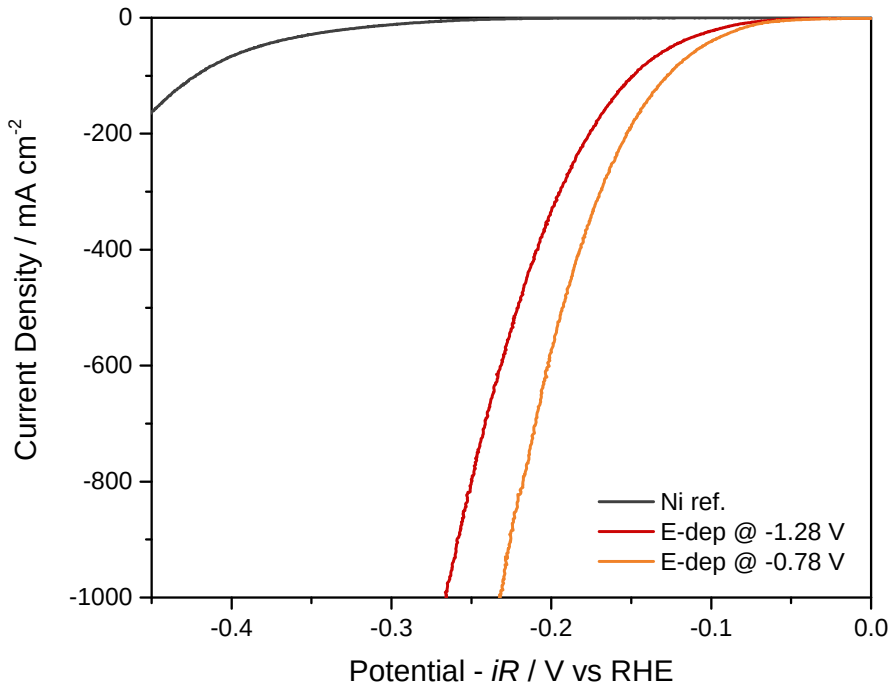

Fig. 5.8: Electrode polarization of NiSn coated nickel foam prepared by potentiostatic electrodeposition. Deposition potentials refer to RHE. T = RT, [KOH] = 30 wt%.

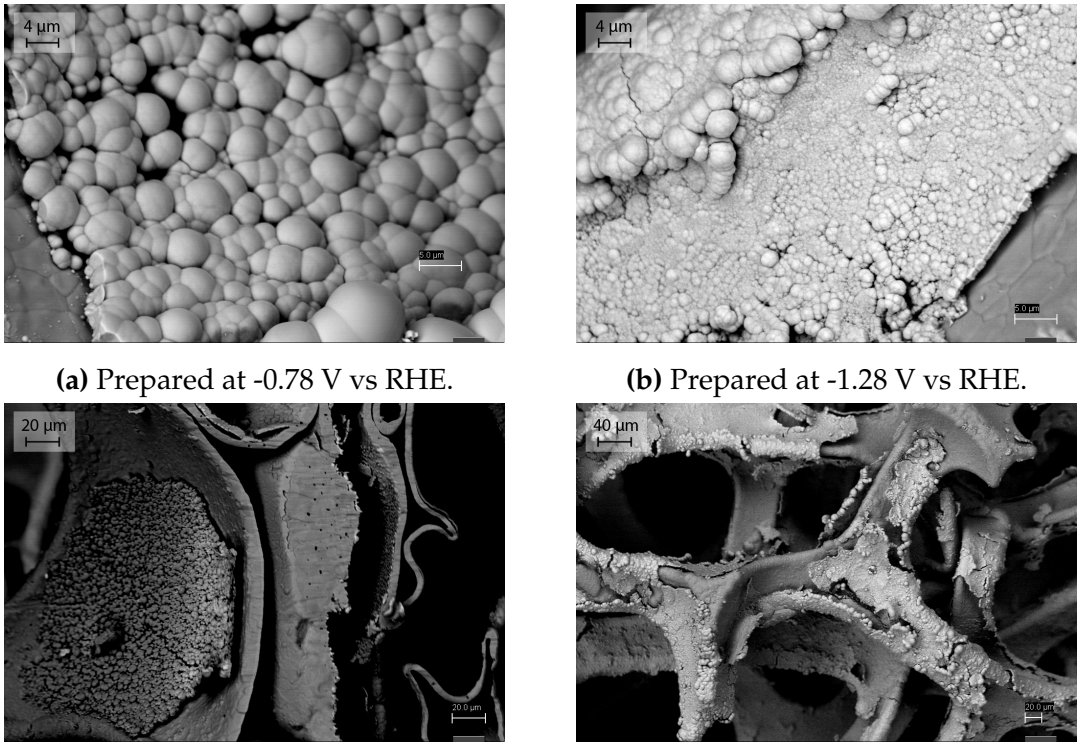

(a) Prepared at -0.78 V vs RHE.

(b) Prepared at -1.28 V vs RHE.

(c) Prepared at -0.78 V vs RHE.

(d) Prepared at -1.28 V vs RHE.

Fig. 5.9: Backscatter detector SEM micrographs of NiSn-electrodes prepared potentiostatically. Electrodes were deposited at **(a)** and **(c)** -0.78 V vs RHE and, **(b)** and **(d)** -1.28 V vs RHE, until 50 C cm^{-2} has passed through.

hesion of the deposited material. EDX performed on the coating indicated an approximately 62:38 Ni:Sn molar stoichiometry.

In the proceeding experiments a pre-treatment process consisting of a degreasing and an etching step were introduced. Electrodes were prepared galvnostatically rather than potentiostatically, and preparation parameters such as the deposition current density, the total charge, the metal precursor stoichiometry, and the temperature were varied systematically. Unfortunately very inconsistent data results were obtained within the frame of the project but a few observations were made regarding the preparation procedure. Generally speaking, electrocoating at constant current lead to worse performance than what was demonstrated with constant potential. It further more lead to stoichiometry changes throughout the coatings which resulted in mechanical tension and consequently poor mechanical adhesion and the coating peeling off. This is illustrated in Figure 5.10a-5.10c. The signal intensity of the backscatter detector

change from dark (Ni) at the support through bright (Ni:Sn $\sim$ 6:4 mol ratio) at the inner layer to a grey shade in between (Ni:Sn $\sim$ 9:1). Furthermore a clear delamination between the support and the coating is seen. It can be speculated, that if the deposition procedure were stopped prior to the apparent tin-depletion, there would be less mechanical stress, but most electrodes had deposition carry on beyond that point. Figure 5.10d illsutrate severe flaking observed on several electrodes, and Figure 5.10e to 5.10g show how increasing loading change the morphology from uniform to a cracked and bulged structure. Among these, the uniform coating showed very poor activity, likely as a result of too high tin content, whereas increasing loading lead to increasing activity.

Unfortunately only provisional conclusions can be drawn from this work. On the positive side very active electrodes can be prepared using a potentiostatic electrodeposition approach, but the mechanical stability specifically in terms of adhesion must be improved. This can possibly be solved by simply pre-treating the substrate with degreasing and etching steps. Secondly, it was observed that galvanostatic deposition lead to variations in stoichiometry in the coated layers in the investigated parameter range. This lead to mechanical stress and displayed overall lower activity. However, several publications use galvanostatic deposition,[113,114] so it is likely feasible at lower current densities, with better agitation, or perhaps at other solution compositions.

5.2.2 NiMo and *a*-NiCoS cathodes

Nickel-molybdenum and nickel-cobalt-sulfide electrodes have not been the subject of detailed investigation but both have been tested on a preliminary level. Nickel-molybdenum because literature repeatedly show this material to have high activity, and amorphous NiCoS since it is used commercially and can be used as a reference. Data for two different prepared NiMo(f) electrodes are presented together with the commercial NiCoS(pp) reference, and NiSn data from previous section in Figure 5.11. Note that data were collected with different protocols and that the electrolyte concentration was different across measurements. This has a significant effect on the results and direct comparison must be done with caution. We further note that the NiCoS electrodes are known to activate over several hours and may prove more active upon prolonged electrolysis than here presented.

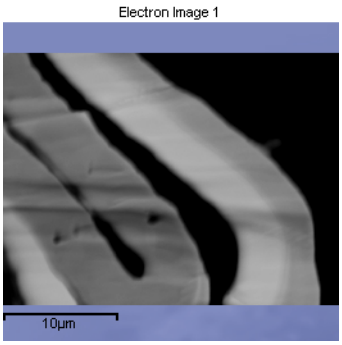

(a) BSD SEM.

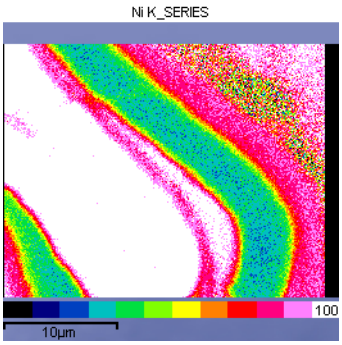

(b) Ni content [wt%].

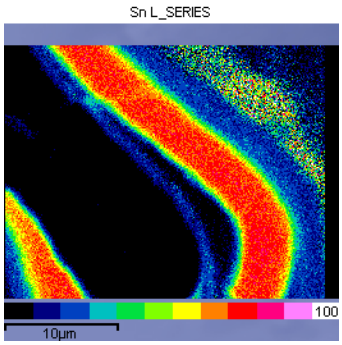

(c) Sn content [wt%].

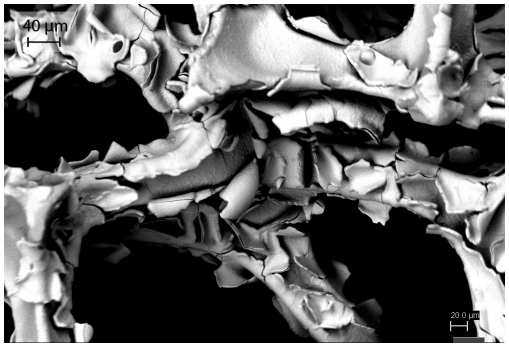

(d) 50 C cm^{-2} @ -183 mA cm^{-2}.

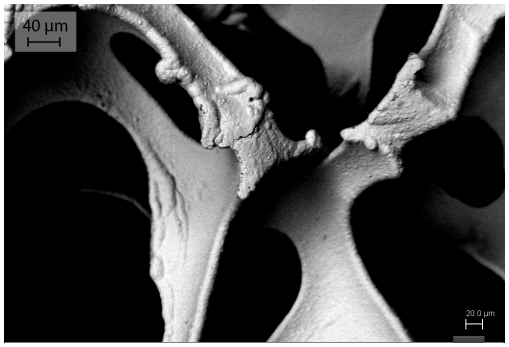

(e) 10 C cm^{-2} @ -100 mA cm^{-2}.

(f) 100 C cm^{-2} @ -100 mA cm^{-2}.

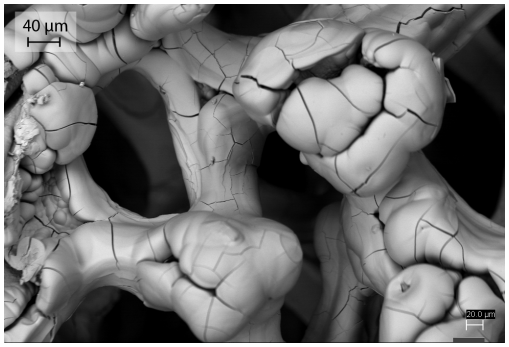

(g) 500 C cm^{-2} @ -100 mA cm^{-2}.

Fig. 5.10: NiSn-electrodes prepared galvanostatically. **(a-c)** EDX elemental mapping with weight% scale and, **(d-g)** Backscatter detector SEM micrographs of selected electrodes at $\times 500$ magnification.

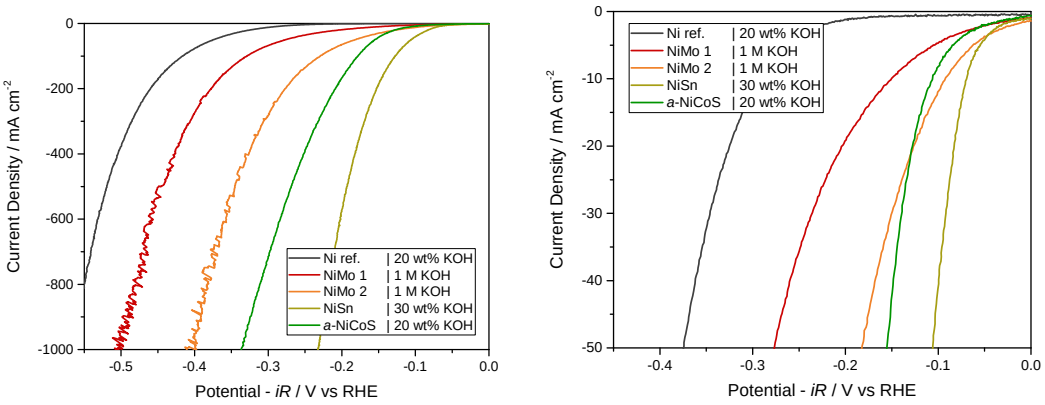

Fig. 5.11: Electrode polarization of selected nickel based cathodes at current density scales down to, **(a)** -1000 mA cm^{-2} and, **(b)** -50 mA cm^{-2}. NiMo 1 and 2 represent different NiMo electrodes prepared with different deposition parameters. T = RT and [KOH] is labelled on the figure.

It is evident that all the presented materials show promise over pristine nickel, even if improved surface area may play a dominant role in the demonstrated increase in activity. Although this work has not investigated either material sufficiently to establish a more active reference electrode to replace the pristine nickel reference, the preliminary investigation show that it might be worthwhile spending more time on.

5.3 Powder based electrodes

When developing electrodes for alkaline polymer membrane electrolysis there are two primary approaches. The first is to apply coatings on support materials such as nickel meshes or foams. This approach was followed with the nickel-iron type anodes from Section 5.1 and the mixed nickel based cathodes in Section 5.2, and is very common in literature for alkaline OER and HER. This concept require liquid electrolyte and is to a large degree incompatible with AEM systems, unless an ionomer is infiltrated onto the electrode. It is however, compatible with classic alkaline and APEM electrolysis. The second approach is to apply a catalyst powder at the membrane-electrode interface, e.g. with the assistance of an ionomer or binder. This approach is identical to what is used in PEM electrolysis, and in fuel cell technology and have the prospect of eliminating bubble issues and significantly reducing ohmic losses, as bubbles will develop on the backside of the active layer. This approach however, is incompatible with classical porous type diaphragms, but can be used in APEM electrolysis and AEM when an ionomer is included. The following section discuss work on this type of electrodes.

In the context of this work, the second approach may be referred to as *porous electrodes*, whereas the first is sometimes referred to as *3D electrodes* when using foam supports, due to the more extensive thickness dimension. Both types are in principle both three dimensional and porous.

The porous type electrodes can generally be prepared in two ways. As a catalyst coated membrane (CCM) or a catalyst coated substrate (CCS). A CCM electrode will generally have a transport layer of some kind which can correspond to the substrate layer in a CCS approach. It is not easily possible to determine which is the most favourable approach, as it will depend on essentially all the involved parameters. Consider e.g. membrane swelling behaviour, ink behaviour, geometry of support, and much more.

5.3.1 Dip-coated

The initial approach was to imitate electrodes prepared for nickel batteries or alkaline fuel cell electrodes. The common preparation method is to blend nickel and/or raney-nickel with a PTFE suspension and an organic solvent. The or-

ganic solvent is only used in small amounts, i order to form a paste rather than an ink. The paste is then rolled or kneaded into a substrate (mesh/foam), after which the entire thing is cured to improve PTFE dispersion in the electrode. Although a number of uniformly-looking electrodes were prepared, this approach was abandoned since PTFE is highly hydrophobic and a highly hydrophilic electrode is desired. In fuel cells the hydrophobicity is necessary to achieve a triple phase boundary, whereas in electrolysis the gas should be disposed of as quickly as possible to ensure complete wetting. Results by Marini *et al.* presented in a series of papers on PTFE bonded gas evolution electrodes also show poor high current density behaviour relative to otherwise good activation behaviour exactly as would be expected.[126,258]

As a variation we turned to *m*-PBI as a binder, as it demonstrate very good hydrophilic behaviour. However, PBI forms a solution with a suitable solvent, unlike PTFE which come as a dispersion of particles. Hence, the kneading and rolling procedure which deform PTFE particles to increase binding properties does not work with a dissolved polymer. Consequently, a different preparation approach was necessary.

m-PBI can be dissolved in alkaline ethanol[259] which was attempted, rather than more conventional solvents such as dimethylacetamide (DMAc) or formic acid. At 2-5 wt% KOH in EtOH, up to 5 wt% *m*-PBI can readily be dissolved even at room temperature. Electrode ink was prepared with nickel powder (< 10 µm) and the PBI solution. Due to the large particle size of the metallic powder, ink formation was nigh impossible but a slurry like mixture could be obtained, from which small electrodes could be prepared. Either by dip-coating (*dip*) or by casting (*cast*) the slurry onto pieces of electrode substrate (nickel foam). The electrodes were then left to dry. The prepared electrodes were not completely uniform and significant differences between sister electrodes was observed. While the specific preparation method with the used catalyst particle size is unfit for additional work, the electrodes prepared can still be used as an initial assessment for the feasibility of preparing porous electrodes. Loadings of the prepared electrodes were everywhere in the range of 10-300 mg/cm^2. This is high values, but note that very large metallic particles were used, and that nickel foam supports with a 1000 µm thickness can contain a lot of material. Exemplary optical microscopy images partially show the lack of uniformity, and are presented in Figure 5.12.

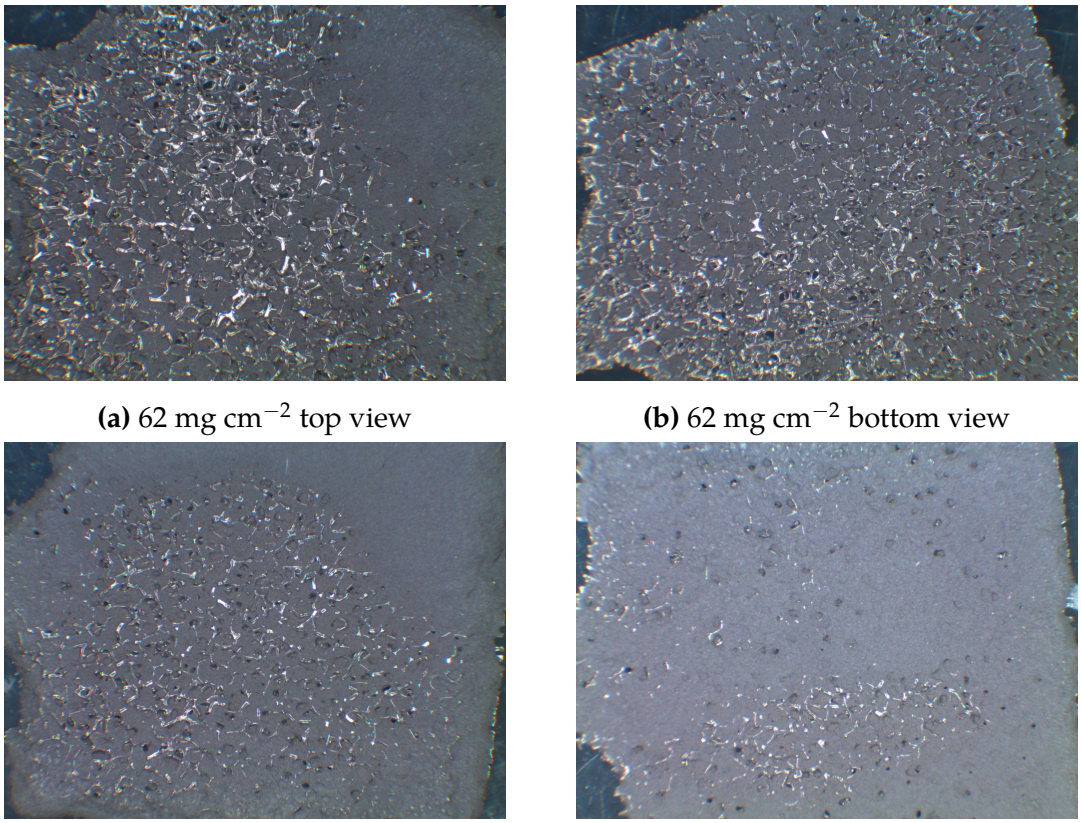

(a) 62 mg cm^{-2} top view

(b) 62 mg cm^{-2} bottom view

(c) 121 mg cm^{-2} top view

(d) 121 mg cm^{-2} bottom view

Fig. 5.12: Microscopy images of two porous electrodes with *m*-PBI binder and with different nickel loadings, **(a)** and **(b)** 62 mg cm^{-2} and 2% *m*-PBI and, **(c)** and **(d)** 121 mg cm^{-2} and 2% *m*-PBI. The images represent roughly the full 1×1 cm^2 area of the electrode.

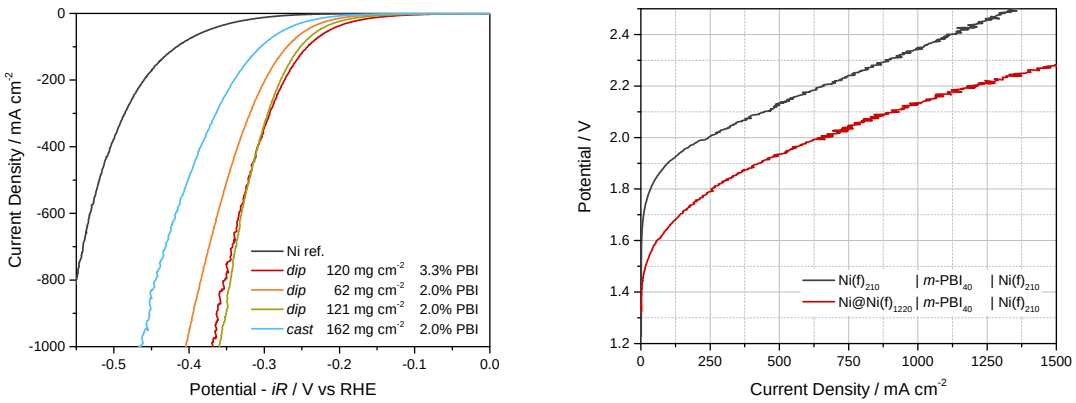

(a) **(b)**

Fig. 5.13: Evaluation of porous electrodes prepared with nickel powder and *m*-PBI binder as cathodes, **(a)** half cell tests at T = RT and [KOH] = 20 wt%. **(b)** Single cell test with a porous cathode, loading 161 mg cm^{-2} nickel (Ni@Ni(f)) and 2% *m*-PBI as binder, *m*-PBI membrane, and nickel foam anode. Indices denote thickness. T = 80°C, [KOH] = 20 wt%, flowrate = 120 ml min^{-1}, flowfield = pin.

Electrodes were evaluated for the HER since the OER is more difficult due to phase transformations of nickel and problems in ensuring good electrode conductivity. Electrodes selected on basis of uniformity and performance are presented in Figure 5.13a. A single electrode was evaluated as cathode in a full single cell and is presented in Figure 5.13b

It is difficult to draw to definite conclusions but some trends could be observed on basis on the recorded data. Figure 5.13a only shows a fraction of the evaluated half-cell electrodes. Firstly, the increased amount of nickel surface improved the activity. Secondly, the electrodes prepared big dip-coating type method appear more active than those prepared by casting the slurry onto the substrate. Possibly, the ability to drain off excessive solvent help prevent excessive polymer-film formation locally in the electrode, and in effect result in a better binder-catalyst structure. In terms of loading, will an increased loading positively influence the activity as long as other parameters are comparable. The binder (*m*-PBI) content were not seen directly trend one way or the other. We note that varying a single parameter while maintaining the others was difficult due to changing rheological properties. The solvent:binder:catalyst ratio heavily influence the apparent viscosity in particular when working with slurries rather than various degrees of low viscosity inks. One can imagine, that by reducing particle size by 2 orders of magnitude an equivalent loading reduction can be

achieved without performance costs.

The single cell test also reveal significantly improved activation performance, but the polarization behaviour towards the high current density range (> 200 mA cm^2) reveal a slightly different qualitative behaviour that appear less ohmic. No diagnostic measurements have been attempted, but likely a more complex gas-discharge behaviour is involved in the porous electrode than the pristine nickel foam which show a more open structure.

5.3.2 Tape casting

At Forschungszentrum Jülich some effort was also put into preparing porous electrodes in addition to cell measurements with Raney-nickel electrodes. A tape-casting approach was used in which a catalytic ink was spread on a polymeric support (primarily PTFE) with a doctor blade. An adhesive film was die cut to form an electrode mask and placed on the support. The doctor blade then moved across the film to distribute the ink evenly over the electrode mask, after which the solvent evaporated. As an extension of the work described in previous section, *m*-PBI was used as binder from a KOH/EtOH solution, but the catalyst was a nano-powder (5-20 nm) of nickel-nickel oxide core-shell catalysts. Conveniently, this enable stable inks to be prepared, which give a wider range of options for electrode preparation, and loadings were consequently lower, namely in the range 2-10 mg cm^{-2}.

First electrode batches attempted at preparing free standing catalyst layers, but this did not prove successful for a number of reasons. The biggest obstacle was an issue with film tension causing the film to crumble in on it self near the end of the solvent evaporation process. Attempts at hotpress-transferring the catalyst films from PTFE sheets to *m*-PBI membranes did not succeed, since the glass-transition temperature for PBI is too high. Electrodes cast on kapton stuck too well to the support, so while they did not crumble due to mechanical tension in the layer they could not be transferred to a all.

Later batches attempted to coat the catalyst directly onto nickel foam supports or *m*-PBI membranes. This turned out to be a better approach, but issues related to tension in the catalyst layer persisted. Likely, the evaporation of solvent increase concentration of KOH and *m*-PBI in the solvent until eventually both KOH and *m*-PBI precipitates. Probably a sort of tension gradient is formed due to in-

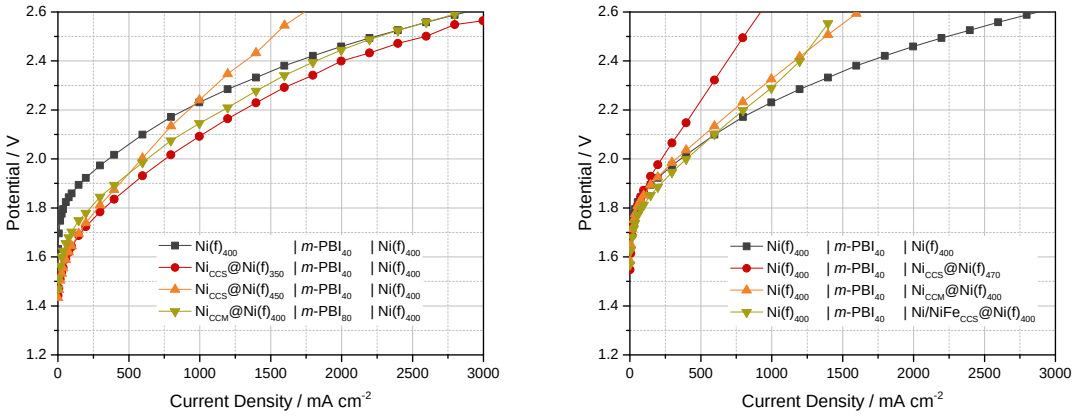

(a) **(b)**

Fig. 5.14: Cell polarization with porous electrodes prepared using nickel nanopowder, when applied as **(a)** cathode, and **(b)** anode. Loadings are in the range 4-10 mg cm^{-2} and the *m*-PBI fraction about 5%. Indices denote thickness. T = 80°C, [KOH] = 24 wt%, flowrate = 5 ml min^{-1}, flowfield = pin(FZJ).

creasing KOH concentration at later drying stages, but whether it is due to KOH salt precipitation, or the polymer changing properties were difficult to determine. Coating directly onto a membrane with a doctor blade is easier with very uniform and even membranes, which the in-house prepared membranes proved not to be. Furthermore, there may be complications related to the swelling of *m*-PBI upon equilibration with KOH (aq). Ultimately, a few electrodes prepared as CCM and CCS were realised with sufficient quality for a cell test. The results for cathodes and anodes are presented in Figure 5.14a and 5.14b. Note that no fixed method for preparation were developed and that all electrodes are different.

Most notable is the improvements in activation when the nickel catalyst is applied to the cathode compared with the anode. It is also clear that the effect appear to be lost at high current densities probably due to transport or bubble phenomena.

Recorded GEIS spectra were generally very noisy, but visual estimation of R_s reveal higher values than previously presented cells, and a larger increase in R_s as function of current density. The reference cell with pristine nickel foam on either side show approximately 0.11 Ω cm^2 which shift approximately by 0.01 Ω cm^2 to 0.12 Ω cm^2 going from 40 to 2000 mA cm^{-2}. This behaviour is somewhat similar to the behaviour presented previously in Figure 4.11. On the other hand, the cell with the best performing coated cathode (●) shift from 0.11

to 0.13 Ω cm^2, the second best (▼) from 0.12 to 0.16 Ω cm^2, and the worst (▲) shift from 0.15 to 0.21 Ω cm^2. Clearly, the direct or indirect ohmic contribution from the electrodes are very significant, and poor gas-discharge properties in the electrode cause increased ohmic and polarization resistances at higher current densities. Although GEIS does not easily identify bubble effects in this type of system, it is clear that some transport or bubble issues are present. This could be a result of the electrode binder forming a dense polymer film and partially encapsulating the catalysts in the electrode, rather than forming a uniform and porous dispersion throughout the catalysts coatings. No microscopy or other characterization were done to investigate this further. The behaviour is much worse when similar electrodes are applied at the anode. At the activation region (< 100 mA cm^{-2}) all electrodes display slightly improved performance over the uncoated reference, but this is lost as current density increase. R_s values estimated by GEIS increase from 0.17 to 0.32 Ω cm^2 (●), from 0.19 to 0.21 Ω cm^2 (▼), and from 0.17 to 0.44 Ω cm^2 (▲). Not only is the low range current density R_s larger than the reference cell most likely due to poor conductivity within the coating, but the shift in R_s with current density indicate significant problems caused by gas bubbles.

The stability were not systematically studied, but most cells were run for at least a few hours. Most cells show a notable potential degradation, and interestingly the cell with a CCM cathode displayed the best stability and barely had any degradation over 20 hours at 100 mA cm^{-2}.

Although no distinct conclusions can be drawn on specific preparation procedures relative to performance and stability, the feasibility of using nickel nanopowder or other nano catalysts has been demonstrated. Using *m*-PBI from a KOH (EtOH) solution appears to be problematic for tape-casting, but other solvents, preparation methods, or binders could enable the realization of efficient and stable CCS and CCM electrodes.

6

Conclusion and outlook

6.1 Conclusions

Alkaline water electrolysis was investigated as a technological pathway towards cost-efficient sustainable hydrogen production. This was done on the basis of cheap materials available to the alkaline system, with focus on improving efficiency to match the similar, but more efficient and more expensive PEM electrolyzers.

One step towards this goal was to use thin (40 µm) alkaline compatible membranes with high ionic conductivity based on *m*-PBI. The thin membranes decreased the inter-electrode spacing in the electrolysis cells compared to conventional porous separators. This resulted in a reduction of the ohmic losses in the cell and opened the window to operating at current densities > 1000 mA cm^{-2}. In parallel, efficient cathodes based on Raney-nickel-molybdenum and anodes based on Raney-nickel with high surface areas were applied making the electrolyzer completely free from noble metal catalysts. By combining *m*-PBI membranes and Raney-nickel electrodes, alkaline electrolysis performance on par with state-of-the-art PEM electrolysis have been demonstrated. In the presence of 24 wt% aqueous KOH at 80°C we achieve 1000 mA cm^{-2} at 1.7 V, and 2900 mA cm^{-2} at 2.0 V, above the target of 2000 mA cm^{-2} at 2.0 V.

Analysis and cell failure reveal problems with regards to membrane stability and cells display limited lifetimes of up to 13 days using 80 µm *m*-PBI membranes. This is, however, longer than most results published in literature on membranes for alkaline electrolysis. Furthermore, the contribution to the overpotential from the membranes were estimated to be minor, suggesting that parameters effecting membrane stability such as temperature, KOH (aq) concentration, as well as membrane thickness, could be varied to improve stability in exchange for slightly reduced polarization performance. EIS for instance, revealed a 6-fold reduction in ohmic cell resistance for the best cells, compared to cells based on conventional materials.

Membranes based on mes-PBI were investigated as a more stable membrane material than *m*-PBI, and tests showed similar polarization performance at 25 wt% KOH but a lower peak conductivity. An improved stability was observed only at concentrations < 10 wt% KOH, where cell polarization is worse than traditional porous separators due to too low conductivity.

Electrodes were prepared following two conceptual approaches: One concept was to coat nickel foams with active catalysts by hydrothermal or electrodeposition methods. In this way Ni-Fe-(oxy)hydroxide anodes, and Ni-Mo and Ni-Sn cathodes were prepared, which each showed improved performance over plain nickel used reference material. The reduction in onset overpotential from Ni-Fe anodes compared to pure nickel were seen to diminish at temperatures relevant for single cell tests (80°C), although partly due to suspected Fe-contamination of the uncoated electrodes originating from system components. Nonetheless, an improved ohmic behaviour was observed and further improvement of preparation procedure is expected to yield even better performance. The development of Ni-Sn and Ni-Mo cathodes did not reach a level during the project at which single cell tests were warranted, but half cell tests at room temperature showed up to 300 mV reduction in overpotential compared to nickel foam.

The second approach used nickel powder as a basis for electrodes. Rather than modifying the surface of nickel foam, it was simply used as a support. Although no reliable and reproducible preparation route was achieved, good cathode performance was achieved. Using preliminary electrodes with ~ 5 µm nickel particles and *m*-PBI as binder, a 200 mV improvement over plain nickel foam was seen in single cell tests. When used as anodes, too large ohmic or mass transport losses were observed for the tested electrodes.

6.2 Outlook

Looking ahead some key challenges remain and a number of opportunities lie ahead. No matter the approach used for electrode preparation, the membrane remain essential to achieving high performance in alkaline electrolysis. In light of the good performance achieved in this project, and compared against the poor performance of AEM electrolysis demonstrated in literature so far, proceeding in the direction of ion-solvating membranes in the presence of aqueous KOH appears to be the most attractive approach. However, the currently investigated materials are not sufficiently stable for practical applications, leaving us with a challenge that must be overcome. This can be achieved either through different PBI derivatives with improved steric protection at high KOH concentrations, or by using other stable and hydrophilic polymers that can readily form electrolyte systems with water and KOH.

A key step towards improving electrode performance is to utilize the full electrode area. The applied Raney-nickel-coated perforated plates, which show high activity, are restricted by large perforations without active material and large solid phase without gas discharge capability. More active electrodes can likely be realized in two key conceptual ways which both circumvent this problem:

One approach is to coat active high surface area catalysts on macro-porous supports like nickel foam, similar to what was presented in the thesis. Coatings with optimized preparation conditions and good stability under real conditions can be envisioned to show a higher activity, both with Ni-Mo or Ni-Sn cathodes and with Ni-Fe anodes. In recent literature a few publications using nickel-molybdenum cathodes display negligible onset overpotential for the HER at room temperature and 1 M KOH, and publications based on Ni-Fe/Co sulfide or selenide have shown lower OER overpotentials than what was demonstrated with the preparation procedure followed here. The stability and activity of these will have to be evaluated at higher temperatures (50-80°C) and more concentrated KOH electrolyte (15-25 wt%).

The second approach is to use nano-powders to form thin catalyst layers right at the membrane-electrode interface. With proper optimization this should result in gas discharging from the backside and has the possibility of showing a better ohmic response than coated macro or micro-porous supports. The next step towards this would be to use well proven hydrophilic binders such

as nafion, rather than *m*-PBI, and to use nickel nano-powder rather than micro-powder. Preparing anodes this way has an extra set of challenges due to the low conductivity of many metal oxides. This could be solved by blending active catalysts, e.g. Ni-Fe-(oxy)hydroxide, with phase stable conductive oxides such as $NiCo_2O_4$, or by preparing catalysts layers with two steps using different materials.

In either case, improving electrodes can direct the system towards operation at milder conditions, which will help in regards to membrane and overall stability. Conversely, fully stable membranes might enable operation at higher temperatures improving electrode kinetics.

References

[1] Key World Energy Statistics 2016, tech. rep., International Energy Agency, Paris, France, **2016**.

[2] International Energy Outlook 2016, tech. rep., U.S. Energy Information Administration, **2016**.

[3] BP Statistical Review of World Energy 2016, tech. rep., BP P.L.C., London, United Kingdom, **2016**.

[4] S. Sorrell, R. Miller, R. Bentley, J. Speirs, *Energy Policy* **2010**, *38*, 4990–5003.

[5] Public health, environmental and social determinants of health (PHE), World Health Organization, http://www.who.int/phe/health_topics/outdoorair/databases/en/ (visited on 03/06/2016).

[6] Ambient air pollution: A global assessment of exposure and burden of disease, tech. rep., World Health Organization, **2016**.

[7] IPCC, Climate Change 2014: Synthesis Report. Contribution of Working Group I, II and III to the Fifth Assessment Report of the Intergovernmental Panel on Climate Change, tech. rep., IPCC, Geneva, Switzerland, **2014**.

[8] Trends in Atmospheric Carbon Dioxide, U.S. Department of Commerce, National Oceanic and Atmospheric Administration, Earth Systems Research Laboratory, **2017**, https://www.esrl.noaa.gov/gmd/ccgg/trends/index.html (visited on 03/01/2017).

[9] J. Hansen, M. Sato, R. Ruedy, *Proceedings of the National Academy of Sciences* **2012**, *109*, E2415–E2423.

[10] K. Bleich, R. D. Guimaraes, Renewable Infrastructure Investment Handbook: A Guide for Institutional Investors, tech. rep., World Economic Forum, **2016**.

[11] Energistatistik 2015, tech. rep., Energistyrelsen, Copenhagen, Denmark, **2015**.

[12] Dansk vindstrøm slår igen rekord - 42 procent [Danish windpower make another record - 42 percent], Energinet.dk, **2016**, https://www.energinet.dk/Om-nyheder/Nyheder/2017/04/25/Dansk-vindstrom-slar-igen-rekord-42-procent (visited on 07/31/2017).

[13] Technology Roadmap Energy Storage, tech. rep., International Energy Agency, Paris, France, **2014**.

[14] B. Decourt, B. Lajoie, R. Debarre, O. Soupa, Hydrogen-Based Energy Conversion, More than Storage: System Flexibility, tech. rep., SBC Energy Institute, Paris, France, **2014**.

[15] Technology Roadmap Hydrogen and Fuel Cells, tech. rep., International Energy Agency, Paris, France, **2015**.

[16] M. Götz, J. Lefebvre, F. Mörs, A. McDaniel Koch, F. Graf, S. Bajohr, R. Reimert, T. Kolb, *Renewable Energy* **2016**, *85*, 1371–1390.

[17] SSAB, LKAB and Vattenfall launch initiative for a carbon-dioxide-free steel industry, SSAB, LKAB and Vattenfall, **2016**, https://www.ssab.com/globaldata/news-center/2016/04/04/05/32/ssab-lkab-and-vattenfall-launch-initiative-for-a-carbondioxidefree-steel-industry (visited on 07/31/2017).

[18] P. Zakkour, G. Cook, CCS Roadmap for Industry: High-purity CO_2 sources, tech. rep., Carbon Counts, **2010**.

[19] C. Graves, S. D. Ebbesen, M. Mogensen, K. S. Lackner, *Renewable and Sustainable Energy Reviews* **2011**, *15*, 1–23.

[20] K. Zeng, D. Zhang, *Progress in Energy and Combustion Science* **2010**, *36*, 307–326.

[21] A. Ursua, L. Gandia, P. Sanchis, *Proceedings of the IEEE* **2012**, *100*, 410–426.

[22] B. Simonsen, "Hydrogen reaching fossil parity around the world", Presented at the 1st International Conference on Electrolysis, Copenhagen, 13th of June, **2017**.

[23] V. M. Rosa, M. B. F. Santos, E. P. da Silva, *International Journal of Hydrogen Energy* **1995**, *20*, 697–700.

[24] J. Kerres, G. Eigenberger, S. Reichle, V. Schramm, K. Hetzel, W. Schnurnberger, I. Seybold, *Desalination* **1996**, *104*, 47–57.

[25] J. Divisek, P. Malinowski, J. Mergel, H. Schmitz, *International Journal of Hydrogen Energy* **1988**, *13*, 141–150.

[26] H. Wendt, G. Imarisio, *Journal of Applied Electrochemistry* **1988**, *18*, 1–14.

[27] H. Vandenborre, R. Leysen, L. Baetsle, *International Journal of Hydrogen Energy* **1980**, *5*, 165–171.

[28] H. Vandenborre, R. Leysen, H. Nackaerts, P. Vanasbroeck, *International Journal of Hydrogen Energy* **1984**, *9*, 277–284.

[29] P. Vermeiren, W. Adriansens, J. P. Moreels, R. Leysen, *International Journal of Hydrogen Energy* **1998**, *23*, 321–324.

[30] V. Kienzlen, D. Haaf, W. Schnurnberger, *International Journal of Hydrogen Energy* **1994**, *19*, 729–732.

[31] J. Otero, J. Sese, I. Michaus, M. Santa Maria, E. Guelbenzu, S. Irusta, I. Carrilero, M. Arruebo, *Journal of Power Sources* **2014**, *247*, 967–974.

[32] D. Pletcher, X. Li, *International Journal of Hydrogen Energy* **2011**, *36*, 15089–15104.

[33] F. Allebrod, C. Chatzichristodoulou, P. L. Mollerup, M. B. Mogensen, *International Journal of Hydrogen Energy* **2012**, *37*, 16505–16514.

[34] F. Allebrod, C. Chatzichristodoulou, M. B. Mogensen, *ECS Transactions* **2014**, *64*, 1029–1038.

[35] C. Chatzichristodoulou, F. Allebrod, M. B. Mogensen, *Journal of The Electrochemical Society* **2016**, *163*, F3036–F3040.

[36] F. Allebrod, C. Chatzichristodoulou, M. B. Mogensen, *Journal of Power Sources* **2014**, *255*, 394–403.

[37] G. G. Scherer, T. Momose, K. Tomiie, *Journal of The Electrochemical Society* **1988**, *135*, 3071.

[38] P. Millet, M. Pineri, R. Durand, *Journal of Applied Electrochemistry* **1989**, *19*, 162–166.

[39] U. Babic, M. Suermann, F. N. Büchi, L. Gubler, T. J. Schmidt, *Journal of The Electrochemical Society* **2017**, *164*, F387–F399.

[40] M. Carmo, D. L. Fritz, J. Mergel, D. Stolten, *International Journal of Hydrogen Energy* **2013**, *38*, 4901–4934.

[41] M. Schalenbach, G. Tjarks, M. Carmo, W. Lueke, M. Müller, D. Stolten, *Journal of The Electrochemical Society* **2016**, *163*, F3197–F3208.

[42] P. C. K. Vesborg, T. F. Jaramillo, *RSC Advances* **2012**, *2*, 7933.

[43] L. Bertuccioli, A. Chan, D. Hart, F. Lehner, B. Madden, E. Standen, Study on the development of water electrolysis in the EU, Technical report, For the Fuel Cells and Hydrogen Joint Undertaking under the European Commision, E4tech Sàrl and element energy, **2014**.

[44] F. Allebrod, "PEM Electrolysis Systems and Stacks for Renewable Energy Storage and Sector Coupling", Presented at the 1st International Conference on Electrolysis, Copenhagen, 14th, **2017**.

[45] J. Parrondo, M. George, C. Capuano, K. E. Ayers, V. Ramani, *J. Mater. Chem. A* **2015**, *3*, 10819–10828.

[46] C. De Pauli, S. Trasatti, *Journal of Electroanalytical Chemistry* **2002**, *538-539*, 145–151.

[47] M. Schalenbach, M. Carmo, D. L. Fritz, J. Mergel, D. Stolten, *International Journal of Hydrogen Energy* **2013**, *38*, 14921–14933.

[48] S. D. Ebbesen, S. H. Jensen, A. Hauch, M. B. Mogensen, *Chemical Reviews* **2014**, *114*, 10697–10734.

[49] F. M. Sapountzi, J. M. Gracia, C. (.-J. Weststrate, H. O. Fredriksson, J. (Niemantsverdriet, *Progress in Energy and Combustion Science* **2017**, *58*, 1–35.

[50] C. B. Prag, Ph.D. Thesis, Technical University of Denmark, **2014**.

[51] CRC Handbook of Chemistry and Physics, version 97th Edition, CRC Press, **2016**, http://hbcponline.com/faces/contents/ContentsSearch.xhtml.

[52] NIST, Data overview of water, National Institute of Standards and Technology, **2016**, http://webbook.nist.gov/cgi/inchi?ID=C7732185.

[53] C. Borgnakke, R. E. Sonntag, *Fundamentals of Thermodynamics*, 8th, Wiley, **2013**.

[54] 2016 Mirai Product Information, Toyota Motor Corporation, **2016**.

[55] ElPris.dk, **2017**, www.elpris.dk.

[56] S. Trasatti, *Electrochimica Acta* **1984**, *29*, 1503–1512.

[57] E. Fabbri, A. Habereder, K. Waltar, R. Kotz, T. Schmidt, *Catalysis Science & Technology* **2014**, DOI 10.1039/C4CY00669K.

[58] C. C. L. McCrory, S. Jung, I. M. Ferrer, S. M. Chatman, J. C. Peters, T. F. Jaramillo, *Journal of the American Chemical Society* **2015**, *137*, 4347–4357.

[59] S. Trasatti, *Journal of Electroanalytical Chemistry and Interfacial Electrochemistry* **1972**, *39*, 163–184.

[60] J. K. Nørskov, T. Bligaard, A. Logadottir, J. R. Kitchin, J. G. Chen, S. Pandelov, U. Stimming, *Journal of The Electrochemical Society* **2005**, *152*, J23.

[61] I. C. Man, H.-Y. Su, F. Calle-Vallejo, H. A. Hansen, J. I. Martínez, N. G. Inoglu, J. Kitchin, T. F. Jaramillo, J. K. Nørskov, J. Rossmeisl, *ChemCatChem* **2011**, *3*, 1159–1165.

[62] J. Suntivich, K. J. May, H. A. Gasteiger, J. B. Goodenough, Y. Shao-Horn, *Science* **2011**, *334*, 1383–1385.

[63] Z. W. Seh, J. Kibsgaard, C. F. Dickens, I. Chorkendorff, J. K. Nørskov, T. F. Jaramillo, *Science* **2017**, *355*, eaad4998.

[64] F. Safizadeh, E. Ghali, G. Houlachi, *International Journal of Hydrogen Energy* **2015**, *40*, 256–274.

[65] A. Rami, A. Lasia, *Journal of Applied Electrochemistry* **1992**, *22*, 376–382.

[66] L. Birry, A. Lasia, *Journal of Applied Electrochemistry* **2004**, *34*, 735–749.

[67] M. Bodner, A. Hofer, V. Hacker, *Wiley Interdisciplinary Reviews: Energy and Environment* **2015**, *4*, 365–381.

[68] D. S. P. Cardoso, S. Eugénio, T. M. Silva, D. M. F. Santos, C. a. C. Sequeira, M. F. Montemor, *RSC Advances* **2015**, *5*, 43456–43461.

[69] M. Zeng, Y. Li, *J. Mater. Chem. A* **2015**, *3*, 14942–14962.

[70] D. Pletcher, R. Greff, R. Peat, L. M. Peter, J. Robinson, *Instrumental Methods in Electrochemistry*, Woodhead Publishing Limited, **2001**, Chapter 7.

[71] M. Gong, D.-Y. Wang, C.-C. Chen, B.-J. Hwang, H. Dai, *Nano Research* **2016**, *9*, 28–46.

[72] Y. Wang, G. Zhang, W. Xu, P. Wan, Z. Lu, Y. Li, X. Sun, *ChemElectroChem* **2014**, *1*, 1138–1144.

[73] J. Zhang, T. Wang, P. Liu, Z. Liao, S. Liu, X. Zhuang, M. Chen, E. Zschech, X. Feng, *Nature Communications* **2017**, *8*, 15437.

[74] Y. Jin, X. Yue, C. Shu, S. Huang, P. K. Shen, *J. Mater. Chem. A* **2017**, *5*, 2508–2513.

[75] S. Gupta, N. Patel, R. Fernandes, S. Hanchate, A. Miotello, D. Kothari, *Electrochimica Acta* **2017**, *232*, 64–71.

[76] C. Tang, N. Cheng, Z. Pu, W. Xing, X. Sun, *Angewandte Chemie International Edition* **2015**, *54*, 9351–9355.

[77] N. Yang, C. Tang, K. Wang, G. Du, A. M. Asiri, X. Sun, *Nano Research* **2016**, *9*, 3346–3354.

[78] G.-F. Chen, T. Y. Ma, Z.-Q. Liu, N. Li, Y.-Z. Su, K. Davey, S.-Z. Qiao, *Advanced Functional Materials* **2016**, *26*, 3314–3323.

[79] B. You, Y. Sun, *Advanced Energy Materials* **2016**, *6*, 1502333.

[80] S.-i. Tanaka, N. Hirose, T. Tanaki, Y. H. Ogata, *International Journal of Hydrogen Energy* **2001**, *26*, 47–53.

[81] J. R. McKone, B. F. Sadtler, C. a. Werlang, N. S. Lewis, H. B. Gray, *ACS Catalysis* **2013**, *3*, 166–169.

[82] J. Luo, J.-H. Im, M. T. Mayer, M. Schreier, M. K. Nazeeruddin, N.-G. Park, S. D. Tilley, H. J. Fan, M. Gratzel, *Science* **2014**, *345*, 1593–1596.

[83] W. Zhu, X. Yue, W. Zhang, S. Yu, Y. Zhang, J. Wang, J. Wang, *Chem. Commun.* **2016**, *52*, 1486–1489.

[84] H. Liang, L. Li, F. Meng, L. Dang, J. Zhuo, A. Forticaux, Z. Wang, S. Jin, *Chemistry of Materials* **2015**, *27*, 5702–5711.

[85] H. Vrubel, X. Hu, *Angewandte Chemie International Edition* **2012**, *51*, 12703–12706.

[86] P. Los, A. Rami, A. Lasia, *Journal of Applied Electrochemistry* **1993**, *23*, 135–140.

[87] C. K. Kjartansdóttir, L. P. Nielsen, P. Møller, *International Journal of Hydrogen Energy* **2013**, *38*, 8221–8231.

[88] Y. Zhu, X. Zhang, J. Song, W. Wang, F. Yue, Q. Ma, *Applied Catalysis A: General* **2015**, *500*, 51–57.

[89] Q. Han, K. Liu, J. Chen, X. Wei, *International Journal of Hydrogen Energy* **2003**, *28*, 1345–1352.

[90] I. A. Raj, K. I. Vasu, *Journal of Applied Electrochemistry* **1990**, *20*, 32–38.

[91] I. A. Raj, *Journal of Materials Science* **1993**, *28*, 4375–4382.

[92] Q. Han, K. Liu, J. Chen, X. Wei, *International Journal of Hydrogen Energy* **2003**, *28*, 1207–1212.

[93] E. R. Gonzalez, L. A. Avaca, G. Tremiliosi-Filho, S. A. S. Machado, M. Ferreira, *International Journal of Hydrogen Energy* **1994**, *19*, 17–21.

[94] Y. Choquette, L. Brossard, H. Menard, *International Journal of Hydrogen Energy* **1990**, *15*, 551–555.

[95] D. Miousse, A. Lasia, V. Borck, *Journal of Applied Electrochemistry* **1995**, *25*, 592–602.

[96] G. Schiller, V. Borck, *International Journal of Hydrogen Energy* **1992**, *17*, 261–273.

[97] D. Pletcher, X. Li, S. Wang, *International Journal of Hydrogen Energy* **2012**, *37*, 7429–7435.

[98] D. E. Brown, M. N. Mahmood, A. K. Turner, S. M. Hall, P. O. Fogarty, *International Journal of Hydrogen Energy* **1982**, *7*, 405–410.

[99] D. E. Brown, M. N. Mahmood (T. B. P. C. Limited), US 4,358,475, **1982**.

[100] X. Zhang, J. Hampshire, K. Cooke, X. Li, D. Pletcher, S. Wright, K. Hyde, *International Journal of Hydrogen Energy* **2015**, *40*, 2452–2459.

[101] M. Santos, E. da Silva, R. Andrade, J. Dias, *Electrochimica Acta* **1992**, *37*, 29–32.

[102] D. Chade, L. Berlouis, D. Infield, A. Cruden, P. T. Nielsen, T. Mathiesen, *International Journal of Hydrogen Energy* **2013**, *38*, 14380–14390.

[103] E. Endoh, H. Otouma, T. Morimoto, Y. Oda, *International Journal of Hydrogen Energy* **1987**, *12*, 473–479.

[104] H. Yamashita, T. Yamamura, K. Yoshimoto, *Journal of The Electrochemical Society* **1993**, *140*, 2238.

[105] B. Jović, U. Lačnjevac, N. Krstajić, V. Jović, *International Journal of Hydrogen Energy* **2014**, *39*, 8947–8958.

[106] X. Tang, L. Xiao, C. Yang, J. Lu, L. Zhuang, *International Journal of Hydrogen Energy* **2014**, *39*, 3055–3060.

[107] D. E. Brown, M. N. Mahmood, M. C. M. Man, A. K. Turner, **1984**, *29*, 1551–1556.

[108] J. Divisek, H. Schmitz, J. Balej, *Journal of Applied Electrochemistry* **1989**, *19*, 519–530.

[109] G. Schiller, R. Henne, V. Borck, *Journal of Thermal Spray Technology* **1995**, *4*, 185–194.

[110] C. González-Buch, I. Herraiz-Cardona, E. Ortega, J. García-Antón, V. Pérez-Herranz, *Journal of Applied Electrochemistry* **2016**, *46*, 791–803.

[111] H. Okamoto, *Journal of Phase Equilibria and Diffusion* **2008**, *29*, 297–298.

[112] U. Lačnjevac, B. M. Jović, V. D. Jović, *Journal of The Electrochemical Society* **2012**, *159*, D310.

[113] V. D. Jović, U. Lačnjevac, B. M. Jović, L. Karanović, N. V. Krstajić, *International Journal of Hydrogen Energy* **2012**, *37*, 17882–17891.

[114] B. M. Jović, U. Č. Lačnjevac, N. V. Krstajić, V. D. Jović, *Electrochimica Acta* **2013**, *114*, 813–818.

[115] J. B. Holte, K. A. Andreassen, K. Widding, H. Harang (N. H. A.S), NO 139,355, NO Patent, **1978**.

[116] H. Vandenborre, P. Vermeiren, R. Leysen, *Electrochimica Acta* **1984**, *29*, 297–301.

[117] S. Sunde, B. Johansen, G. Hagen, R. Tunold, K. Andreassen in Hydrogen Energy Progress XI: Proceedings of the 11th World Hydrogen Energy Conference, International Association for Hydrogen Energy, Stuttgart, **1996**, pp. 813–817.

[118] S. Egelund, Ph.D. Thesis, Technical University of Denmark, **2015**.

[119] M. Caspersen, Ph.D. Thesis, Technical University of Denmark, **2015**.

[120] J. Staszak-Jirkovský, C. D. Malliakas, P. P. Lopes, N. Danilovic, S. S. Kota, K.-C. Chang, B. Genorio, D. Strmcnik, V. R. Stamenkovic, M. G. Kanatzidis, N. M. Markovic, *Nature Materials* **2015**, *15*, 197–203.

[121] M. Raney, US 1,628,190, US Patent, **1927**.

[122] C. K. Kjartansdóttir, Ph.D Thesis, Technical University of Denmark, **2014**.

[123] T. Kenjo, *Bulletin of the Chemical Society of Japan* **1981**, *54*, 2553–2556.

[124] W. Jenseit, A. Khalil, H. Wendt, *Journal of Applied Electrochemistry* **1990**, *20*, 893–900.

[125] P. Salvi, P. Nelli, M. Villa, Y. Kiros, G. Zangari, G. Bruni, A. Marini, C. Milanese, *International Journal of Hydrogen Energy* **2011**, *36*, 7816–7821.

[126] S. Marini, P. Salvi, P. Nelli, R. Pesenti, M. Villa, Y. Kiros, *International Journal of Hydrogen Energy* **2013**, *38*, 11484–11495.

[127] J. M. Jiri Divisek (K. J. G. mit Beschrankter Haftung), US 4,300,993, US Patent, **1981**.

[128] J. Balej, J. Divisek, H. Schmitz, J. Mergel, *Journal of Applied Electrochemistry* **1992**, *22*, 705–710.

[129] D. V. Sokol'skii, P. I. Zabotin, S. V. Druz, A. M. Zagor'ev, G. V. Akulova, *Soviet Electrochemistry* **1987**, *23*, 853–857.

[130] M. L. Bakker, D. J. Young, M. S. Wainwright, *Journal of Materials Science* **1988**, *23*, 3921–3926.

[131] J. Balej, J. Divisek, H. Schmitz, J. Mergel, *Journal of Applied Electrochemistry* **1992**, *22*, 711–716.

[132] S. Rausch, H. Wendt, *Journal of The Electrochemical Society* **1996**, *143*, 2852.

[133] K. Lohrberg, P. Kohl, *Electrochimica Acta* **1984**, *29*, 1557–1561.

[134] A. Kayser, V. Borck, M. von Bradke, R. Henne, W. A. Kaysser, G. Schiller, *Zeitschrift für Metallkunde* **1992**, *83*, 565–568.

[135] J. M. F. Chemicals, Heterogeneous Catalysts, **2017**, http://www.jmfinechemicals.com/products/heterogeneous-catalysts/ni/ (visited on 04/19/2017).

[136] J. O. Bockris, T. Otagawa, *The Journal of Physical Chemistry* **1983**, *87*, 2960–2971.

[137] J. O. Bockris, *Journal of The Electrochemical Society* **1984**, *131*, 290.

[138] M. Hamdani, R. N. Singh, P. Chartier, *International Journal of Electrochemical Science* **2010**, *5*, 556–577.

[139] Y. Matsumoto, E. Sato, *Materials Chemistry and Physics* **1986**, *14*, 397–426.

[140] F. Dionigi, P. Strasser, *Advanced Energy Materials* **2016**, DOI 10.1002/aenm.201600621.

[141] J. O. Bockris, *The Journal of Chemical Physics* **1956**, *24*, 817.

[142] A. I. Krasil'shichikov, *Zhurnal Fizicheskoi Khimii (Russian Journal of Physical Chemistry A)* **1963**, *37*, 531–537.

[143] W. E. O'Grady, C. Iwakura, J. Huang, E. Yeager in Proceedings Of The Symposium On Electrocatalysis, (Ed.: M. W. Breiter), The Electrochemical Society Inc., Princeton, **1974**, p. 286.

[144] H.-C. Chien, W.-Y. Cheng, Y.-H. Wang, T.-Y. Wei, S.-Y. Lu, *Journal of Materials Chemistry* **2011**, *21*, 18180.

[145] C. C. L. McCrory, S. Jung, J. C. Peters, T. F. Jaramillo, *Journal of the American Chemical Society* **2013**, *135*, 16977–16987.

[146] S. Jung, C. C. L. McCrory, I. M. Ferrer, J. C. Peters, T. F. Jaramillo, *J. Mater. Chem. A* **2016**, *4*, 3068–3076.

[147] O. Diaz-Morales, I. Ledezma-Yanez, M. T. M. Koper, F. Calle-Vallejo, *ACS Catalysis* **2015**, *5*, 5380–5387.

[148] D. Friebel, M. W. Louie, M. Bajdich, K. E. Sanwald, Y. Cai, A. M. Wise, M.-J. Cheng, D. Sokaras, T.-C. Weng, R. Alonso-Mori, R. C. Davis, J. R. Bargar, J. K. Nørskov, A. Nilsson, A. T. Bell, *Journal of the American Chemical Society* **2015**, *137*, 1305–1313.

[149] J. B. Gerken, S. E. Shaner, R. C. Massé, N. J. Porubsky, S. S. Stahl, *Energy & Environmental Science* **2014**, *7*, 2376.

[150] C. Zhang, R. D. Fagan, R. D. L. Smith, S. A. Moore, C. P. Berlinguette, S. Trudel, *J. Mater. Chem. A* **2015**, *3*, 756–761.

[151] R. Singh, D. Mishra, Anindita, A. Sinha, A. Singh, *Electrochemistry Communications* **2007**, *9*, 1369–1373.

[152] R. N. Singh, J. P. Singh, B. Lal, M. J. K. Thomas, S. Bera, *Electrochimica Acta* **2006**, *51*, 5515–5523.

[153] Y. Xiao, L. Feng, C. Hu, V. Fateev, C. Liu, W. Xing, *RSC Advances* **2015**, *5*, 61900–61905.

[154] Anindita, a. Singh, R. N. Singh, *International Journal of Hydrogen Energy* **2010**, *35*, 3243–3248.

[155] K. Elumeeva, J. Masa, F. Tietz, F. Yang, W. Xia, M. Muhler, W. Schuhmann, *ChemElectroChem* **2016**, *3*, 138–143.

[156] W. Zhou, M. Zhao, F. Liang, S. C. Smith, Z. Zhu, *Mater. Horiz.* **2015**, *2*, 495–501.

[157] B. G. Amin, A. T. Swesi, J. Masud, M. Nath, *Chem. Commun.* **2017**, *4*, 4–6.

[158] X. Wu, D. He, H. Zhang, H. Li, Z. Li, B. Yang, Z. Lin, L. Lei, X. Zhang, *International Journal of Hydrogen Energy* **2016**, *41*, 10688–10694.

[159] C. Tang, A. M. Asiri, X. Sun, *Chem. Commun.* **2016**, *52*, 4529–4532.

[160] J. Jiang, A. Zhang, L. Li, L. Ai, *Journal of Power Sources* **2015**, *278*, 445–451.

[161] M. Gong, Y. Li, H. Wang, Y. Liang, J. Z. Wu, J. Zhou, J. Wang, T. Regier, F. Wei, H. Dai, *Journal of the American Chemical Society* **2013**, *135*, 8452–8455.

[162] X. Lu, C. Zhao, *Nature Communications* **2015**, *6*, 1–7.

[163] Z. Lu, W. Xu, W. Zhu, Q. Yang, X. Lei, J. Liu, Y. Li, X. Sun, X. Duan, *Chemical communications* **2014**, *50*, 6479–82.

[164] B. Zhang, X. Zheng, O. Voznyy, R. Comin, M. Bajdich, M. Garcia-Melchor, L. Han, J. Xu, M. Liu, L. Zheng, F. P. Garcia de Arquer, C. T. Dinh, F. Fan, M. Yuan, E. Yassitepe, N. Chen, T. Regier, P. Liu, Y. Li, P. De Luna, A. Janmohamed, H. L. Xin, H. Yang, A. Vojvodic, E. H. Sargent, *Science* **2016**, *1525*, 1–11.

[165] Z. Lu, L. Qian, Y. Tian, Y. Li, X. Sun, X. Duan, *Chem. Commun.* **2016**, *52*, 908–911.

[166] C. Xiao, Y. Li, X. Lu, C. Zhao, *Advanced Functional Materials* **2016**, *26*, 3515–3523.

[167] Z. Li, M. Shao, H. An, Z. Wang, S. Xu, M. Wei, D. G. Evans, X. Duan, *Chem. Sci.* **2015**, *6*, 6624–6631.

[168] D. A. Corrigan, M. R. Bendert, *Journal of The Electrochemical Society* **1989**, *136*, 723.

[169] E. Guerrini, H. Chen, S. Trasatti, *Journal of Solid State Electrochemistry* **2007**, *11*, 939–945.

[170] Y. Lee, J. Suntivich, K. J. May, E. E. Perry, Y. Shao-Horn, *The Journal of Physical Chemistry Letters* **2012**, *3*, 399–404.

[171] A. Grimaud, K. J. May, C. E. Carlton, Y.-L. Lee, M. Risch, W. T. Hong, J. Zhou, Y. Shao-Horn, *Nature Communications* **2013**, *4*, 2439.

[172] L. Trotochaud, S. W. Boettcher, *Scripta Materialia* **2014**, *74*, 25–32.

[173] H. Wendt, V. Plzak, *Electrochimica Acta* **1983**, *28*, 27–34.

[174] J. Balej, *International Journal of Hydrogen Energy* **1985**, *10*, 89–99.

[175] X. Wu, K. Scott, *Journal of Materials Chemistry* **2011**, *21*, 12344.

[176] B. Chi, J. Li, Y. Han, Y. Chen, *International Journal of Hydrogen Energy* **2004**, *29*, 605–610.

[177] G. Zhang, X. W. D. Lou, *Advanced Materials* **2013**, *25*, 976–979.

[178] D. Chanda, J. Hnát, M. Paidar, K. Bouzek, *International Journal of Hydrogen Energy* **2014**, *39*, 5713–5722.

[179] M. S. Burke, L. J. Enman, A. S. Batchellor, S. Zou, S. W. Boettcher, *Chemistry of Materials* **2015**, *27*, 7549–7558.

[180] M. S. Burke, S. Zou, L. J. Enman, J. E. Kellon, C. a. Gabor, E. Pledger, S. W. Boettcher, *The Journal of Physical Chemistry Letters* **2015**, *6*, 3737–3742.

[181] M. Shao, R. Zhang, Z. Li, M. Wei, D. G. Evans, X. Duan, *Chem. Commun.* **2015**, *51*, 15880–15893.

[182] A. Mendiboure, R. Schöllhorn, *Revue de chimie minérale* **1986**, *23*, 819–827.

[183] D. S. Hall, D. J. Lockwood, C. Bock, B. R. MacDougall, *Proceedings of the Royal Society A: Mathematical Physical and Engineering Sciences* **2014**, *471*, 20140792–20140792.

[184] L. Xu, Y.-S. Ding, C.-H. Chen, L. Zhao, C. Rimkus, R. Joesten, S. L. Suib, *Chemistry of Materials* **2008**, *20*, 308–316.

[185] L. Zeng, T. Zhao, *Nano Energy* **2015**, *11*, 110–118.

[186] P. Sun, R. Ma, X. Bai, K. Wang, H. Zhu, T. Sasaki, *Science Advances* **2017**, *3*, e1602629.

[187] M. Gong, H. Dai, *Nano Research* **2015**, *8*, 23–39.

[188] D. A. Corrigan, *Journal of The Electrochemical Society* **1987**, *134*, 377.

[189] D. A. Corrigan (G. M. Corporation), US 4,882,024, **1989**.

[190] M. D. Merrill, R. C. Dougherty, *The Journal of Physical Chemistry C* **2008**, *112*, 3655–3666.

[191] X. Li, F. C. Walsh, D. Pletcher, *Physical chemistry chemical physics : PCCP* **2011**, *13*, 1162–7.

[192] S. Zou, M. S. Burke, M. G. Kast, J. Fan, N. Danilovic, S. W. Boettcher, *Chemistry of Materials* **2015**, *27*, 8011–8020.

[193] L. Trotochaud, S. L. Young, J. K. Ranney, S. W. Boettcher, *Journal of the American Chemical Society* **2014**, *136*, 6744–53.

[194] M. S. Burke, M. G. Kast, L. Trotochaud, A. M. Smith, S. W. Boettcher, *Journal of the American Chemical Society* **2015**, *137*, 3638–3648.

[195] A. S. Batchellor, S. W. Boettcher, *ACS Catalysis* **2015**, *5*, 6680–6689.

[196] C. G. Morales-Guio, L. Liardet, X. Hu, *Journal of the American Chemical Society* **2016**, *138*, 8946–8957.

[197] L.-P. Zhu, G.-H. Liao, Y. Yang, H.-M. Xiao, J.-F. Wang, S.-Y. Fu, *Nanoscale Research Letters* **2009**, *4*, 550–557.

[198] F. Song, X. Hu, *Nature Communications* **2014**, *5*, 1–9.

[199] S. Klaus, Y. Cai, M. W. Louie, L. Trotochaud, A. T. Bell, *The Journal of Physical Chemistry C* **2015**, 7243–7254.

[200] L. J. Enman, M. S. Burke, A. S. Batchellor, S. W. Boettcher, *ACS Catalysis* **2016**, *6*, 2416–2423.

[201] K. Fan, H. Chen, Y. Ji, H. Huang, P. M. Claesson, Q. Daniel, B. Philippe, H. Rensmo, F. Li, Y. Luo, L. Sun, *Nature Communications* **2016**, *7*, 11981.

[202] L.-A. Stern, L. Feng, F. Song, X. Hu, *Energy Environmental Science* **2015**, *8*, 2347–2351.

[203] X. Xu, F. Song, X. Hu, *Nature Communications* **2016**, *7*, 12324.

[204] R. J. Gilliam, J. W. Graydon, D. W. Kirk, S. J. Thorpe, *International Journal of Hydrogen Energy* **2007**, *32*, 359–364.

[205] Foxboro, Conductivity ordering guide, **1999**, http://myweb.wit.edu/sandinic/Research/conductivity%20v%20concentration.pdf (visited on 07/25/2017).

[206] R. J. Guanti, P. J. Moran, *Journal of Applied Electrochemistry* **1986**, *16*, 678–682.

[207] D. M. See, R. E. White, *Journal of Chemical & Engineering Data* **1997**, *42*, 1266–1268.

[208] M. E. Tuckerman, K. Laasonen, M. Sprik, M. Parrinello, *The Journal of Physical Chemistry* **1995**, *99*, 5749–5752.

[209] M. E. Tuckerman, D. Marx, M. Parrinello, *Nature* **2002**, *417*, 925–929.

[210] F. Allebrod, Ph.D. Thesis, Technical University of Denmark, **2013**.

[211] M. B. Knaster, L. A. Apelbaum, *Zhurnal Fizicheskoi Khimii* **1964**, *38*, 223–225.

[212] D. Tromans, *Hydrometallurgy* **1998**, *50*, 279–296.

[213] M. Schalenbach, T. Hoefner, P. Paciok, M. Carmo, W. Lueke, D. Stolten, *The Journal of Physical Chemistry C* **2015**, acs.jpcc.5b04155.

[214] V. Schröder, B. Emonts, H. Janßen, H. P. Schulze, *Chemical Engineering and Technology* **2004**, *27*, 847–851.

[215] G. Merle, M. Wessling, K. Nijmeijer, *Journal of Membrane Science* **2011**, *377*, 1–35.

[216] J. O. Jensen, D. Aili, M. K. Hansen, Q. Li, N. J. Bjerrum, E. Christensen, *ECS Transactions* **2014**, *64*, 1175–1184.

[217] J. R. Varcoe, P. Atanassov, D. R. Dekel, A. M. Herring, M. A. Hickner, P. a. Kohl, A. R. Kucernak, W. E. Mustain, K. Nijmeijer, K. Scott, T. Xu, L. Zhuang, *Energy Environ. Sci.* **2014**, *7*, 3135–3191.

[218] J. Pan, Y. Li, L. Zhuang, J. Lu, *Chemical Communications* **2010**, *46*, 8597.

[219] Y.-C. Cao, X. Wu, K. Scott, *International Journal of Hydrogen Energy* **2012**, *37*, 9524–9528.

[220] M. Faraj, M. Boccia, H. Miller, F. Martini, S. Borsacchi, M. Geppi, A. Pucci, *International Journal of Hydrogen Energy* **2012**, *37*, 14992–15002.

[221] M. G. Marino, K. D. Kreuer, *ChemSusChem* **2015**, *8*, 513–523.

[222] M. G. Marino, J. P. Melchior, A. Wohlfarth, K. D. Kreuer, *Journal of Membrane Science* **2014**, *464*, 61–71.

[223] A. G. Wright, J. Fan, B. Britton, T. Weissbach, H.-F. Lee, E. A. Kitching, T. J. Peckham, S. Holdcroft, *Energy Environ. Sci.* **2016**, *9*, 2130–2142.

[224] B. Xing, O. Savadogo, *Electrochemistry Communications* **2000**, *2*, 697–702.

[225] Q. Li, J. O. Jensen, R. F. Savinell, N. J. Bjerrum, *Progress in Polymer Science* **2009**, *34*, 449–477.

[226] M. K. Hansen, Ph.D. Thesis, Technical University of Denmark, **2012**.

[227] D. Aili, M. K. Hansen, R. F. Renzaho, Q. Li, E. Christensen, J. O. Jensen, N. J. Bjerrum, *Journal of Membrane Science* **2013**, *447*, 424–432.

[228] D. Aili, K. Jankova, Q. Li, N. J. Bjerrum, J. O. Jensen, *Journal of Membrane Science* **2015**, *492*, 422–429.

[229] D. Aili, K. Jankova, J. Han, N. J. Bjerrum, J. O. Jensen, Q. Li, *Polymer* **2016**, *84*, 304–310.

[230] L. Xiao, S. Zhang, J. Pan, C. Yang, M. He, L. Zhuang, J. Lu, *Energy & Environmental Science* **2012**, *5*, 7869.

[231] X. Wu, K. Scott, *Journal of Power Sources* **2012**, *214*, 124–129.

[232] X. Wu, K. Scott, *Journal of Power Sources* **2012**, *206*, 14–19.

[233] C. C. Pavel, F. Cecconi, C. Emiliani, S. Santiccioli, A. Scaffidi, S. Catanorchi, M. Comotti, *Angewandte Chemie International Edition* **2014**, *53*, 1378–1381.

[234] J. Parrondo, C. G. Arges, M. Niedzwiecki, E. B. Anderson, K. E. Ayers, V. Ramani, *RSC Advances* **2014**, *4*, 9875.

[235] Y. Leng, G. Chen, A. J. Mendoza, T. B. Tighe, M. A. Hickner, C.-Y. Wang, *Journal of the American Chemical Society* **2012**, *134*, 9054–9057.

[236] J. Schauer, J. Žitka, Z. Pientka, J. Křivčík, J. Hnát, K. Bouzek, *Journal of Applied Polymer Science* **2015**, *132*, n/a–n/a.

[237] L. A. Diaz, J. Hnát, N. Heredia, M. M. Bruno, F. A. Viva, M. Paidar, H. R. Corti, K. Bouzek, G. C. Abuin, *Journal of Power Sources* **2016**, *312*, 128–136.

[238] Z. Liu, S. D. Sajjad, Y. Gao, J. Kaczur, R. Masel, *ECS Transactions* **2017**, *77*, 71–73.

[239] L. A. Diaz, R. E. Coppola, G. C. Abuin, R. Escudero-Cid, D. Herranz, P. Ocón, *Journal of Membrane Science* **2017**, *535*, 45–55.

[240] P. Haug, M. Koj, T. Turek, *International Journal of Hydrogen Energy* **2017**, *42*, 9406–9418.

[241] A. Garat, J. Gras, *International Journal of Hydrogen Energy* **1983**, *8*, 681–688.

[242] J. Gras, P. Spiteri, *International Journal of Hydrogen Energy* **1993**, *18*, 561–566.

[243] Corrosion Resistance of Nickel and Nickel-Containing Alloys in Caustic Soda and Other Alkalies, tech. rep., Publication No 281 (CEB-2), Nickel Development Institute, Inco Limited,

[244] Technical information-Chemical compatability, tech. rep., Habonim, **2017**.

[245] Application Guide, Corrosion Guide, tech. rep., Watlow,

[246] Guide to the Selection of Corrosion Resisting Non-Metallics, tech. rep., Flowserve Corporation, **2000**.

[247] EPDM & FKM Chemical Resistance Guide, tech. rep., IPEX, **2009**.

[248] Chemical Compatibility Database, Cole-Parmer, https://www.coleparmer.com/Chemical-Resistance (visited on 05/22/2017).

[249] Chemical Resistance Chart, tech. rep., Siemens, **2008**.

[250] D. Aili, A. G. Wright, M. R. Kraglund, K. Jankova, S. Holdcroft, J. O. Jensen, *J. Mater. Chem. A* **2017**, *5*, 5055–5066.

[251] G. Tsotridis, "EU Harmonised Test Protocols for Electrolysis Applications", Presented at the 1st International Conference on Electrolysis, Copenhagen, 13th of June, **2017**.

[252] D. Aili, L. N. Cleemann, Q. Li, J. O. Jensen, E. Christensen, N. J. Bjerrum, *Journal of Materials Chemistry* **2012**, *22*, 5444.

[253] G. Schiller, R. Henne, P. Mohr, V. Peinecke, *International Journal of Hydrogen Energy* **1998**, *23*, 761–765.

[254] H. Ito, T. Maeda, A. Nakano, A. Kato, T. Yoshida, *Electrochimica Acta* **2013**, *100*, 242–248.

[255] M. Dixit, G. N. Subbanna, P. V. Kamath, *J. Mater. Chem.* **1996**, *6*, 1429–1432.

[256] J. Jiang, J. P. Liu, X. T. Huang, Y. Y. Li, R. M. Ding, X. X. Ji, Y. Y. Hu, Q. B. Chi, Z. H. Zhu, *Crystal Growth & Design* **2010**, *10*, 70–75.

[257] M. B. Stevens, L. J. Enman, A. S. Batchellor, M. R. Cosby, A. E. Vise, C. D. M. Trang, S. W. Boettcher, *Chemistry of Materials* **2017**, *29*, 120–140.

[258] S. Marini, P. Salvi, P. Nelli, R. Pesenti, M. Villa, M. Berrettoni, G. Zangari, Y. Kiros, *Electrochimica Acta* **2012**, *82*, 384–391.

[259] M. Litt, R. Ameri, Y. Wang, R. Savinell, J. Wainwright, *MRS Proceedings* **1998**, *548*, 313.

List of publications

Journal publications

Paper I

Zero-Gap Alkaline Water Electrolysis Using Ion-Solvating Polymer Electrolyte Membranes at Reduced KOH Concentrations
Mikkel Rykær Kraglund, David Aili, Katja Jankova, Erik Christensen, Qingfeng Li, and Jens Oluf Jensen
Journal of the Electrochemical Society, 2016, **163** (11) F3125-F3131

Paper II

Towards a stable ion-solvating polymer electrolyte for advanced alkaline water electrolysis
David Aili, Andrew G. Wright, Mikkel Rykær Kraglund, Katja Jankova, Steven Holdcroft, and Jens Oluf Jensen
Journal of Materials Chemistry A, 2017, **5**, 5055-5066

Paper III

Advanced alkaline polymer electrolyte membrane electrolysis using ion-solvating membranes
Mikkel Rykær Kraglund, Marcelo Carmo, Günther Schiller, David Aili, Erik Chris-

tensen, and Jens Oluf Jensen
To be submitted

Conference contributions

Contribution I

Polybenzimidazole membranes in alkaline water electrolysis: Chemical and electrochemical stability
Mikkel Rykær Kraglund, David Aili, Aleksey Nikiforov, Erik Christensen, and Jens Oluf Jensen
Poster presented at the 3rd International Workshop on Degradation Issues of Fuel Cells and Electrolysers, September 29th to October 1st, 2015, Thira, Santorini, Greece

Contribution II

Polybenzimidazole membranes for zero gap alkaline electrolysis cells
Mikkel Rykær Kraglund, David Aili, Erik Christensen, and Jens Oluf Jensen
Poster presented at the 21st World Hydrogen Energy Conference, June 13th to June 16th, 2016, Zaragoza, Spain

Contribution III

Alkaline membrane electrolysis with PEM-level electrochemical performance
Mikkel Rykær Kraglund, Marcelo Carmo, David Aili, Günther Schiller, Erik Christensen, Andreas Friedrich, Detlef Stolten, and Jens Oluf Jensen
Oral presentation at the 1st International Conference on Electrolysis, June 12th, 2017, Copenhagen, Denmark.

A

Preparation methods

This section serve to briefly outline what is meant by the experimental techniques mentioned in Section 2.3. It is not meant to discuss details, benefits or disadvantages. The techniques may be different in other contexts than the herein presented.

Thermal decomposition (TD) is in essence oxidation of metal precursor salts, commonly applied by coating an electrode with a solution of metal salts followed by heat treatment in air (300-1000°C). This form metal oxides directly onto a support, but can also be used to prepared powders.

Electrodeposition (ED) is commonly performed by electrochemically reducing metal cations from an electrolyte to their solid phase directly onto a support. Variations exist where electrochemical reduction or oxidation is used to induce chemical precipitation near the electrode as is done when electrodepositing (oxy)hydroxides.

Electrodeposited composite coating (EDCC) is electrodeposition performed while having fine powder dispersed in the electrolyte. The suspended particles can be co-deposited and immobilized by the growth of a dense electrocoating and will increase surface roughness and may help to reduce mechanical stresses in the coating.

Hydrothermal (HT) precipitation also works by thermally (60-180°C) hydrolysing organic precursors to generate reaction products to modify the pH of a solution containing metal precursors, inducing a homogeneous chemical precipitation.

Magnetron sputtering (MS) is a type of vapour deposition where a target is plasma sputtered and dislodged atoms condense on a substrate of choice.

Sintered powder (SP) is an annealing process often performed under inert atmosphere where a metal or metal-oxide powder is heated sufficiently for the particles to grow together through thermally induced restructuring, without melting the material and collapsing the pore structure of the powder.

Pressed powder(PP) is achieved by applying a high compression pressure onto a powder in an electrode shaped mould. Ductile materials such as metals can deform and produce mechanically stable shapes. This can be followed by sintering to improve mechanical strength.

Vacuum plasma spraying (VPS) accelerates a plasma towards a target and inject precursor powder into the plasma stream near the nozzle. The metal powders melt in the plasma and condense onto the electrode and form a coating. VPS is done under vacuum to prevent oxidation.

Atmospheric plasma spraying (APS) is like VPS, but done at atmospheric conditions. This is a of economic interest, but suffer from oxidation.

Low pressure plasma spraying (LPPS) is a compromise between VPS and APS in an attempt to balance cons and pros of the two techniques.

Physical vapour deposition (PVD) is deposition of atoms from a metallic vapour or plasma e.g. induced by sputtering.

Sulforization (DS/S) is thermal treatment (300-600°C) in an mixed sulfur-inert gas atmosphere. This is realised by placing a sulfur deposit or sulfur compound upstream in e.g a tube furnace with an inert gas stream, and placing a sample to be sulfurized downstream.

Phosphorization (P) is equivalent to sulfurization, except the sulfur deposit or compound is replaced by phosphor or phosphor compound.

Supercritical drying (SD) is the removal of a solvent at supercritical conditions to avoid phase boundary between liquid and gas during drying. This can prevent delicate structures from collapsing and can be used to prepare aerogels. CO_2 is often used for this.

Sol-gel (SG) uses a solution to achieve a uniform mixing on an atomic level of different precursors, and then gradual polymerization of precursors during solvent evaporation, effectively freezing the uniform mixing in place prior to precipitation.

Citrate complexing technique (CCT) is a type of sol-gel technique where citric acid is added prior to drying.

Solid state reaction (SSR) is the reaction between mixed solid powders at high temperatures (1000-1500°C). Mechanical mixing is often done by ball milling.

Chemical precipitation (CP) is in this case done by mixing a solution with metal precursors with a alkaline solution. This increase pH, and form metal hydroxides which precipitate due to their poor solubility.

Ink (drop casting) techniques involve the stable dispersion of a fine powder in typically a volatile solvent often mixed with polymeric binders and e.g. surfactant or dispersion agents. For e.g. RDE electrodes particles are often deposited by drop-casting the ink.

Ink (spraying) deposition by means of spraying likewise require a stable ink, but by spraying it can be uniformly applied to large electrode areas. By spraying the solvent is evaporated gradually, which may be beneficial.

Ink (tape casting) can also be applied as a casting technique for larger areas. Tape casting disperse stable inks uniformly over large areas by distributing the ink using a doctor blade. Either by moving the ink container across a template shape, or by moving a coating support beneath a fixed aperture.

Brush painting is used to disperse slurrys or thick inks on electrode substrates, prior to evaporating the solvent. Brush painting does not form uniform coatings.

Paste rolling is used in e.g. alkaline fuel cells and nickel batteries. An ink or slurry with dispersed PTFE as binder is prepared so thick that it is a paste

rather than ink. The paste is then sheared and kneaded e.g. while rolling the paste into a electrode substrate, which cause the dispersed PTFE particles to shear resulting in a mechanical cross linking.

B

Technical drawings

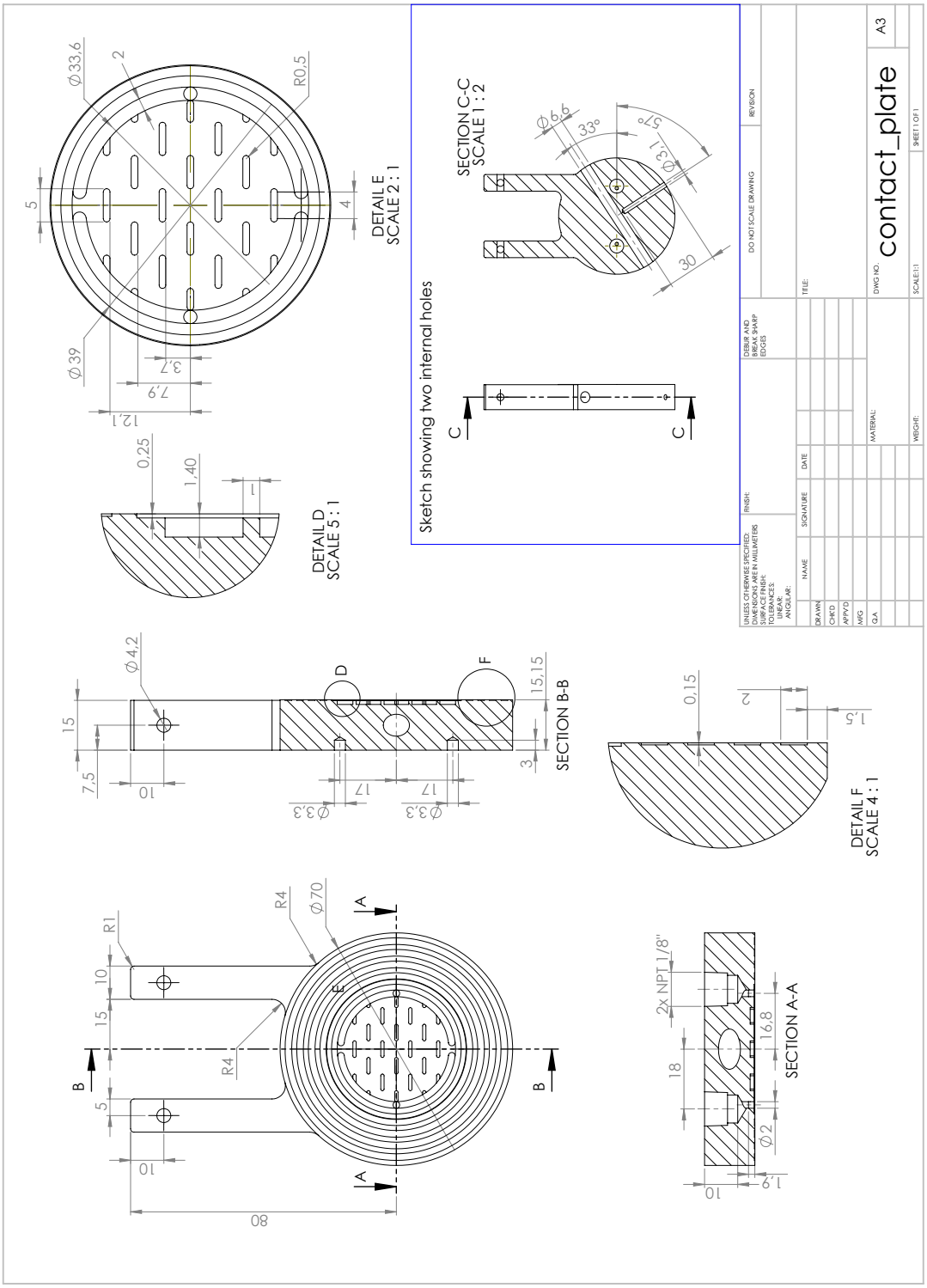

Fig. B.1: Technical drawing of the DTU-cell cell-house and flow field.

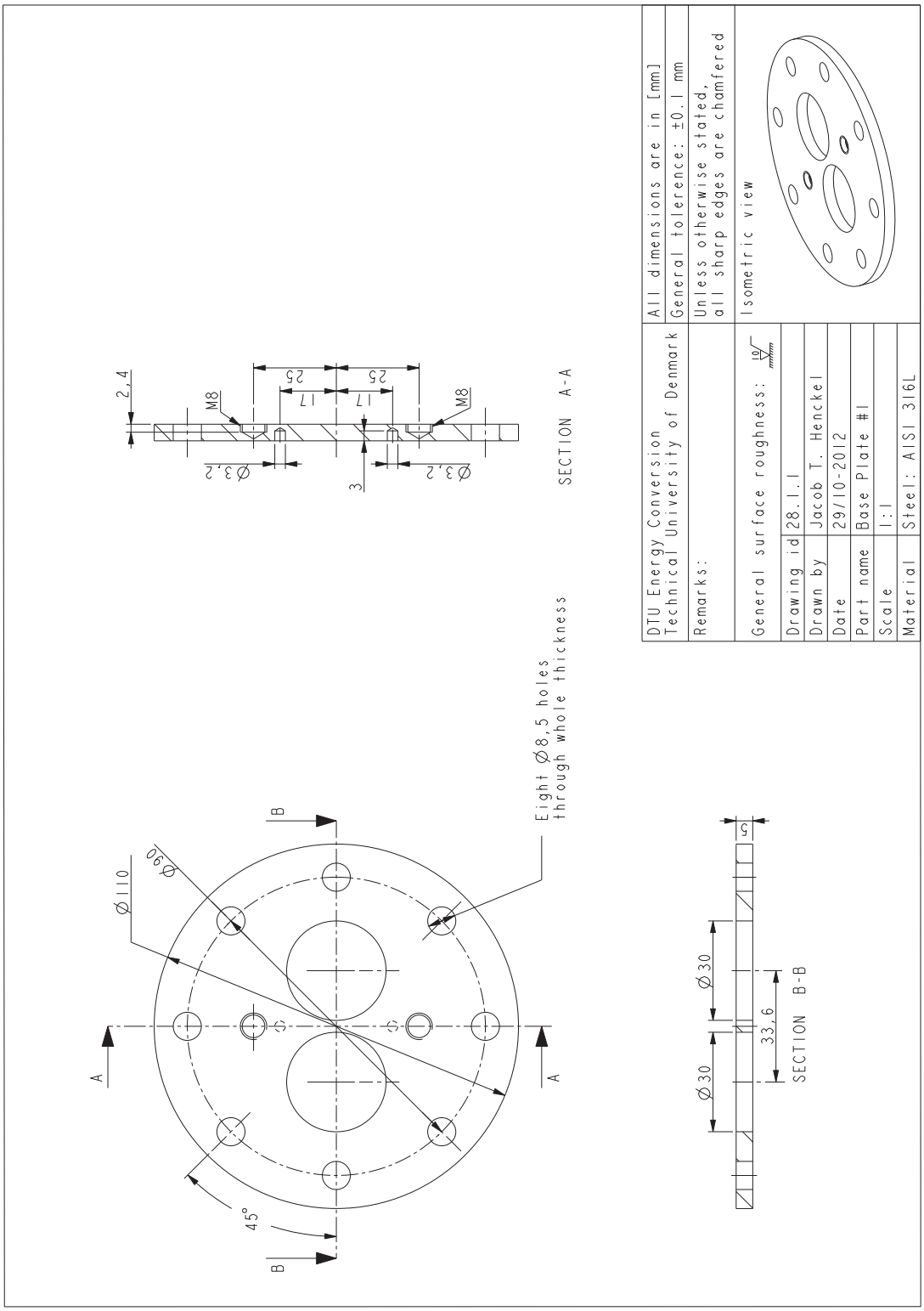

Fig. B.2: Technical drawing of the DTU-cell endplate.